Title

MafB is a conserved transcriptional regulator of macrophage development and functional identity across tissues and species

Authors

Domien Vanneste[1,2,*], Wen Peng[1,2], Zhuangzhuang Liu[3,4], Malik Hamaïdia[5], Raphaël La Rocca[1,2], Joan Abinet[1,2], Alexis Balthazar[2,6], Fabienne Perin[7], Alexandre Hego[8], Didier Cataldo[7], Fabrice Bureau[2,9], Philippe Compère[10,11], Bénédicte Machiels[2,6], Charlotte L. Scott[3,4], Coraline Radermecker[1,2] & Thomas Marichal[1,2,12,13,*]

Affiliations

[1]Laboratory of Immunophysiology, GIGA Institute, University of Liège, Liège, Belgium

[2]Faculty of Veterinary Medicine, University of Liège, Liège, Belgium

[3]Laboratory of Myeloid Cell Biology in Tissue Damage and Inflammation, VIB-UGent Center for Inflammation Research, Ghent, Belgium

[4]Department of Biomedical Molecular Biology, Faculty of Science, Ghent University, Ghent, Belgium

[5]Laboratory of Cellular and Molecular Epigenetics, GIGA Institute, University of Liège, Liège, Belgium

[6]Laboratory of Immunology-Vaccinology, FARAH Institute, University of Liège, Liège, Belgium

[7]Laboratory of Tumour and Development Biology, GIGA Institute, University of Liège, Liège, Belgium

[8]In Vitro Imaging Platform, GIGA Institute, University of Liège, Liège, Belgium

[9]Laboratory of Cellular and Molecular Immunology, GIGA Institute, University of Liège, Liège, Belgium

[10]Laboratory of Functional and Evolutionary Morphology, FOCUS Research Unit, Department of Biology, Ecology and Evolution, University of Liège, Liège, Belgium

[11]Center for Applied Research and Education in Microscopy (CAREM) and Biomaterials Interfaculty Center (CEIB), University of Liège, Liège, Belgium

[12]Walloon Excellence in Life Sciences and Biotechnology (WELBIO) Department, WEL Research Institute, Wavre, Belgium.

[13]Lead contact

*Correspondence: t.marichal@uliege.be (T.M.) and domien.vanneste@uliege.be (D.V.)

SUMMARY

Homeostatic resident tissue macrophages (RTMs) exhibit diversity across tissues but also share common features that are driven by conserved transcriptional programs. While the transcription factor MafB is highly expressed in macrophages, its role in establishing RTM identity and functions remains unclear. Here we show that MafB was required for the development of bone-marrow-derived macrophages (BMDMs) and most RTMs *in vivo*. MafB deficiency retained RTM in a CD52^{high} immature stage and disrupted global and tissue-specific identities and functions, impairing phagocytosis, splenic iron recycling, and lung, kidney and gut physiology. Epigenetic profiling revealed that MafB directly regulated key RTM genes in mouse and humans, including *Csf1r, Mertk, Fcgr1, Cd163* and *Zeb2*. *In silico* analyses further demonstrated strong evolutionary conservation of MafB binding sites across vertebrates. Together, these findings establish MafB as a crucial regulator of RTM development and functional identity, linking MafB-dependent transcriptional programs with defining features of RTMs and tissue homeostasis.

INTRODUCTION

Macrophages (Macs) are integral parts of most mammalian tissues and exhibit an extensive functional diversity.[1–4] Homeostatic tissue macrophage populations present at steady-state, called resident tissue macrophages (RTMs) hereafter, act as professional phagocytes and are gatekeepers of homeostasis by deploying important functions, including clearance of cells and foreign bodies and defense against pathogens, as well as context-specific duties inherent of their tissue of residence.[5–7] While most RTM populations seed tissues before the establishment of definitive hematopoiesis and are long-lived[8–11], bone marrow(BM)-derived monocytes can also contribute to RTM maintenance throughout adult life.[1,12–14]

RTM developmental and functional heterogeneity has been a subject of intense investigations, which has led to the discovery of tissue-specific niche-instructive signals and transcriptional programs dictating such diversity[1,2,13,15–18]. However, macs represent above all, a distinct cell lineage that is defined by common characteristics, including expression of receptors, such as the Csf1 receptor (Csf1r)[19,20] and the high affinity receptor for the immunoglobulin gamma Fc region 1 (Fcgr1)[21,22], and mac-defining transcription factors (TF), such as the Ets family TF PU.1[23,24] and Zinc finger E box binding homeobox 2 (Zeb2).[25] Additional conserved factors arguably contribute to RTM identity and regulate shared and tissue-specific transcriptional programs across RTM populations.

First discovered in 1994[26], Maf basic leucine zipper transcription factor B (MafB) has been found to be highly expressed in myelomonocytic cells, including macs, and contributes to monocytic differentiation.[27–30] Of note, MafB overexpression can induce mac differentiation from chick myeloblasts[28], suggesting a link between MafB and mac development. Subsequent genome-wide and lineage-tracing studies support elevated MafB expression in RTMs, distinguishing them from dendritic cells (DCs) and monocytes.[3,22,31]

Initial studies investigating MafB contributions to mac development *in vivo* have used *Mafb*$^{-/-}$ mice[30] or mice reconstituted with MafB-deficient hematopoietic cells[32,33] and have found no marked defects in mac numbers.[30,32,33] *In vitro*, MafB-deficient macs retain phagocytic and nitric oxide–producing capacities, but display enhanced actin remodeling and membrane protrusions upon macrophage Csf1 stimulation.[32] When both MafB and c-Maf are deleted, differentiated macs remain phenotypically and functionally intact yet acquire an unusual capacity for self-renewal, driven by Klf4- and c-Myc–dependent pathways.[33] Additional analyses of MafB-deficient mice reveal context-specific roles of MafB in the regulation of F4/80[30] and complement components C1q[34], the suppression of antiviral responses in microglia (MG)[35], the regulation of brown adipose tissue thermogenesis[36] or the restriction of lung monocyte proliferation prior to interstitial mac (IM) differentiation[37]. Nevertheless, the potentially conserved role of MafB in governing RTM development and identities across tissues and species remains elusive.

Here, we addressed this question using *in vivo* conditional *Mafb* targeting[37], *ex vivo* mac cultures and *in silico* analyses combined with flow cytometry, microscopy, RNA-sequencing (RNA-seq), functional assays as well as epigenetic profiling of MafB binding sites. We found that MafB was highly expressed and active in all tested RTM populations, at the exception of alveolar macs (AMs). Myeloid-restricted MafB deficiency profoundly impaired the full development and the identities of mature RTM across mouse tissues, with important consequences for RTM functions and tissue homeostasis. Among more than conserved 4,000 MafB binding sites identified, we found that MafB directly regulated key differentiation and identity genes, including *Csf1r* and *Fcgr1*, both in mice and humans. Finally, we provided evidence that MafB-dependent regulation of mac identity was highly conserved across

96 species, thereby revealing MafB as a critical and evolutionarily conserved regulator of RTM

97 development and identity.

RESULTS

Elevated MafB expression and activity are conserved in mouse RTMs

To identify transcriptional regulators of mac identity, we analyzed ImmGen microarray data from monocyte, DC, and RTMs.[38] Core mac genes, such as *Csf1r*, *C1q* and *Mertk*, as well as the gene encoding *Mafb* TF, ranked among the top genes upregulated in RTMs *versus* DCs and monocytes (Figure 1A). *Mafb* expression was low in AMs, consistent with previous findings.[37,39] Using the Tabula Muris Senis scRNA-seq dataset[40], we found high MafB expression and predicted TF activity based on the co-expression of target genes[41] in brain MG, liver Kupffer cells (KCs), lung IM and other tissue macs, but not in AMs (Figures 1B–1F). Intracellular flow cytometry confirmed higher MafB protein expression in RTM populations from C57BL/6 wild-type (WT) mice, except in AM, compared with blood monocytes and DCs from the same tissues (Figures 1G, 1H, and S1). In the colon, where colonic macs (CMs) are continuously renewed through the "monocyte waterfall"[42], MafB expression gradually increased along this trajectory (Figures 1I and 1J). A similar pattern was observed in the peritoneal cavity, where Ly6C^{+} monocytes progressively differentiate into F4/80^{+} large peritoneal macs (LPMs) via F4/80^{lo} small peritoneal macs (SPMs)[43] (Figures 1K and 1L). Hence, MafB is highly and exclusively expressed in RTM populations across tissues and its expression is upregulated during mac differentiation from monocytes.

MafB deficiency impedes the full differentiation of macs *in vitro*

To examine the role of MafB in mac differentiation *ex vivo*, BM monocytes (BMMos) from myeloid-intrinsic MafB-deficient (i.e., *Lyz2*^{Cre}*Mafb*$^{fl/fl}$ [37]) or control (*Mafb*$^{fl/fl}$) mice were cultured with Csf1 to generate BM-derived macs (BMDMs) (Figure 2A). Although BMMos from *Lyz2*^{Cre}*Mafb*$^{fl/fl}$ and control mice both produced CD11b^{hi}F4/80^{hi} cells (Figure S2A), MafB-deficient BMDMs did not adopt a typical amoeboid spindle-like cell shape with distinct lamellipodia and remained smaller, spherical and with few filopodia (Figures 2B, 2C, and S2B; Videos S1 and S2), suggesting impaired differentiation. Bulk RNA-seq analyses identified 808 differentially expressed genes (DEGs) ($\log_2$ fold change > 1 or < −1, adjusted *P* value < 5×10^{-2}) between control and MafB-deficient BMDM (Figures 2D and 2E; Table S1), with reduced *Mafb* and prototypical mac genes, such as *Mertk* and C1q complement genes (*C1qa*, *C1qb* and *C1qc*), and increased monocyte genes (*Ly6c, Ccr2*) in MafB-deficient BMDMs compared to control BMDMs (Figure 2D). We generated monocyte and mac signature scores by comparing monocytes and RTMs in the ImmGen database (Table S2) and found, using Gene Set Enrichment Analysis (GSEA), that the monocyte signature was significantly enriched in MafB-deficient BMDMs, while the mac signature was enriched in control BMDMs (Figure 2F). In addition, BMDMs from *Lyz2*^{Cre}*Mafb*$^{fl/fl}$ mice exhibited significantly higher protein expression of the classical monocyte markers Ly6C, CD62L and CD11a and lower protein expression of the mac markers MerTK, C1qA and FR-β compared to those from control mice (Figures 2G and S2C). Gene ontology (GO) analyses revealed an enrichment of developmental processes (e.g., differentiation, development) in control BMDMs, and of stimulus response (e.g., communication, activation) in MafB-deficient BMDMs (Figures S2D and S2E), reminiscent of a plastic monocyte phenotype. These findings indicate that MafB regulates Csf1-dependent mac differentiation *ex vivo*.

MafB controls RTM development and transcriptional identity *in vivo*

Next, to assess whether MafB could also mediate monocyte-to-RTM development *in vivo*, we generated BM competitive chimeras in which CD45.1.2 mice were irradiated and reconstituted with a 1:1 BM cell mix from congenic CD45.1 WT and CD45.2 *Lyz2*^{Cre}*Mafb*$^{fl/fl}$ mice (Figure 3A). At week 5 after transfer, the ratio of WT donor chimerism over total donor chimerism of blood neutrophils and monocytes, as well as of SPMs, was between 20 and 45%, while in all other RTMs, such ratio was between 80 and 100% (Figures 3B and 3C), demonstrating that, in this competitive setting, myeloid-restricted MafB deficiency impaired the ability of monocytes to differentiate in RTMs, at the exception of SPMs.

Next, we asked whether MafB deficiency altered the transcriptional identity of RTMs. Live peritoneal lavage CD45$^+$Lin$^-$Ly6C$^-$CD11b$^+$CD115$^+$ cells, liver CD45$^+$Lin$^-$Ly6C$^-$CD11b$^{int/+}$F4/80$^+$CD64$^+$ cells, colon CD45$^+$Lin$^-$CD11b$^+$F4/80$^+$CD64$^+$ cells and brain CD45$^+$Lin$^-$Ly6C$^-$CD11b$^+$F4/80$^+$CD64$^+$ cells were isolated from *Lyz2*^{Cre}*Mafb*$^{fl/fl}$ and *Mafb*$^{fl/fl}$ littermate controls, were hashtag-barcoded and subjected to single cell (sc)RNA-seq (Figure 3D). Curated data were integrated with previously published scRNA-seq data containing CD45$^+$SSC^{lo}CD11b$^+$F4/80$^+$CD64$^+$ lung IMs from *Lyz2*^{Cre}*Mafb*$^{fl/fl}$ mice and *Mafb*$^{fl/fl}$ littermate controls[37] and were projected in UMAP plots (Figures 3E and S3A). Based on the expression of hashtag barcodes and known RTM-specific genes, we identified mac populations corresponding to SPMs (*Cd226*, *Retnla*) and LPMs (*Gata6*, *Icam2*) in the peritoneal lavage; KCs (*Clec4f*, *Cdh5*) in the liver; IMs (*Mgl2*, *Ccl2*) in the lung; and MG (*Tmem119*, *Sall1*) in the brain (Figure 3F). In the colon, we identified two clusters of CMs characterized by high expression of *Plac8* and *Ly6c2* or of *Cd4* and *H2-M2*, respectively (Figure 3F). Signature scoring based on

DEGs between Ly6C$^+$ cells and MHC-II$^+$ cells from the monocyte waterfall (Table S2)[44] revealed that these clusters corresponded to Ly6C$^+$ CMs and MHC-II$^+$ CMs, respectively (Figure S3B).

Mafb mRNA was not detected in SPMs, LPMs, KCs, IMs and CMs from *Lyz2^{Cre}Mafb$^{fl/fl}$* mice, while *Mafb* depletion was only partial in MG from *Lyz2^{Cre}Mafb$^{fl/fl}$* mice (Figure S3C). Next, we conducted differential gene expression analysis between RTMs from *Lyz2^{Cre}Mafb$^{fl/fl}$* mice and *Mafb$^{fl/fl}$* littermate controls and identified 92 DEGs in SPMs, 535 DEGs in LPMs, 262 DEGs in KCs, 287 DEGs in IMs, 723 DEGs in Ly6C$^+$ CMs, 150 DEGs in MHC-II$^+$ CMs and 299 DEGs in MG (Figures S3D–S3J; Table S3). Of note, RTM-specific identity genes such as *Retnla* for SPMs, *Vsig4* for LPMs, *Cd163* for KCs, and *Fcrls* for MG were significantly lower expressed in MafB-deficient cells. Next, we created RTM subset-specific scores based on the DEGs of each control RTM subset compared to other RTMs in our scRNA-seq data and found that each RTM subsets from *Lyz2^{Cre}Mafb$^{fl/fl}$* mice, except for IMs, exhibited a significantly lower score for RTM-subset specific signatures as compared to their respective controls (Figure 3G; Table S2). To examine whether MafB deficiency also affected global mac differentiation, we mapped previously identified signatures of erythro-myeloid progenitors (EMP), pre-mac and mac comprising different stages of mac differentiation (Table S2).[45] EMP signatures were low in all subsets similar between MafB-deficient and control RTMs (Figure 3H). All MafB-deficient RTMs exhibited a significantly higher pre-mac score as compared to control RTMs (Figure 3H). Moreover, global mac signature scores were all significantly lower in MafB-deficient RTMs as compared to their WT counterparts (Figure 3H). To explore this further, we built a macrophage differentiation atlas from published scRNA-seq data containing CD11b$^{low/+}$ fetal liver cells at embryonic developmental day E14.5 (Figures 3I and S3K).[46] Using Slingshot pseudotime, we identified *Cd52* as highly expressed in pre-mac but downregulated at the pre-mac to mac transition, coinciding with increased *Mafb* expression (Figures 3J and S3L). Of note, *Cd52* was

higher expressed in most MafB-deficient RTMs as compared to their WT counterparts, with the exception of Ly6C^{+} CMs (Figure 3K), and surface expression of CD52 was elevated in SPMs, LPMs, IMs and KCs from *Lyz2^{Cre}Mafb$^{fl/fl}$* mice as compared to controls (Figure 3L). Together, these findings show that MafB mediates RTM differentiation and identity across embryonically-derived and monocyte-derived RTMs, and its absence leads to incomplete differentiation with a persistent CD52^{high} immature signature and loss of subset-specific programs.

Loss of MafB profoundly alters RTM phenotype across tissues

Next, we assessed how MafB deficiency affected RTM abundance and phenotype. MafB deficiency did not alter blood monocyte numbers or proportions, CD62L expression on classical monocytes (cMos), nor the proportion of GMP- or MDP-derived cMos (Figures S4A–S4D).[47] In peritoneal lavages, *Lyz2^{Cre}Mafb$^{fl/fl}$* mice displayed higher proportion and numbers of LPMs (Figures 4A and 4B). MafB-deficient SPMs expressed lower MHC-II and Relmα, while LPMs had reduced F4/80, MerTK and Vsig4 expression (Figures 4C and 4D). In livers of *Lyz2^{Cre}Mafb$^{fl/fl}$* mice, KC proportions decreased while F4/80^{lo}CD11b^{hi} monocyte-macrophage intermediate cells (Mo-Macs) increased (Figures 4E and 4F). In addition, KC markers FR-β, Tim4, Vsig4, CD163 were reduced in KCs from *Lyz2^{Cre}Mafb$^{fl/fl}$* mice as compared to controls (Figure 4G). Similar decreases in Tim4, Vsig4, CD163 expression were seen in KCs from *Clec4f^{Cre}Maf$^{fl/fl}$Mafb$^{fl/fl}$* mice as compared to controls (Figure S5A). Of note, confocal microscopy analyses revealed that KCs from *Lyz2^{Cre}Mafb$^{fl/fl}$* and from *Clec4f^{Cre}Maf$^{fl/fl}$Mafb$^{fl/fl}$* mice displayed a less stellate morphology and lower Tim4 expression compared to control KCs (Figures S5B–S5E). In lungs, as reported[37], *Lyz2^{Cre}Mafb$^{fl/fl}$* mice showed an imbalance between CD64^{+} monocytes and IMs with fewer IMs (Figures S4E and S4F). MafB-deficient IMs expressed

more CD11b but less F4/80, MHC-II and CD206, while IM subset proportions were unchanged (Figures S4G–S4I). In the colons of *Lyz2^{Cre}Mafb$^{fl/fl}$* mice, Ly6C^{+} CMs increased while Ly6C^{+}MHC-II^{+} CMs decreased (Figures S4J and S4K). MHC-II^{+} CM numbers were unchanged, but MafB-deficient MHC-II^{+} CMs expressed more CD11b and less CD163 (Figure S4L). CD163 expression in MHC-II^{+} CMs has been proposed to distinguish CD163^{-} colonic lamina propria macs (C LPMs) and CD163^{+} muscularis macs (MMs)[48]. Nevertheless, the proportions and counts of C-LPMs and MMs were unaffected in *Lyz2^{Cre}Mafb$^{fl/fl}$* mice (Figures S4M and S4N). In *Lyz2^{Cre}Mafb$^{fl/fl}$* brains, MG and border-associated mac (BAM) numbers were unchanged (Figures 4H and 4I), but MG showed reduced P2ry12 and Fcrls expression (Figure 4J). Lower MG-intrinsic P2ry12 expression was also observed in tamoxifen-treated *Tmem119^{CreERT2}Mafb$^{fl/fl}$* mice compared to controls (Figure S5F). Higher percentage and numbers of MHC-II^{+} BAMs were also found in the brains of *Lyz2^{Cre}Mafb$^{fl/fl}$* mice (Figures 4K and 4L). In *Lyz2^{Cre}Mafb$^{fl/fl}$* spleen, red pulp macs (RPMs) tended to decrease while CD11b^{+} mac increased, and RPMs showed decreased Cd163 expression, similar to KCs (Figures 4O–4Q). In kidneys of *Lyz2^{Cre}Mafb$^{fl/fl}$* mice, kidney resident mac (KRM) proportions decreased among CD11b^{+} cells, with reduced F4/80 and increased Ly6C expression (Figures S4N–S4P). These results support that MafB deficiency profoundly disrupts RTM abundance and phenotype across tissues.

MafB mediates key RTM phagocytic and homeostatic functions

Next, we examined the functional consequences of MafB loss on RTMs. First, we focused on the core function of macs, phagocytosis. Upon intraperitoneal injection of *S. aureus* pHrodo-Red particles, both the proportion of positive LPMs and the particle load per cell were significantly reduced in *Lyz2^{Cre}Mafb$^{fl/fl}$* mice compared to controls (Figures 5A and 5B). KC phagocytosis was even more impaired after intravenous (i.v.) injection (Figures 5C and 5D).

Given the key role of splenic RPMs in erythrocyte recycling and iron homeostasis[49], we injected PKH26-labeled senescent red blood cells (sRBCs) i.v. and found that MafB-deficient RPMs showed reduced erythrophagocytosis (Figures 5E and 5F). These observations were also reflected at the tissue level without sRBC injection, with *Lyz2*^{Cre}*Mafb*$^{fl/fl}$ mice suffering from splenomegaly and abnormal iron accumulation in the spleen red pulp, as revealed by Perl's Prussian blue staining (Figures 5G and 5H). Since IMs and CMs have been shown to support lung mechanics[50] and gut motility[51], respectively, we measured these functions in *Lyz2*^{Cre}*Mafb*$^{fl/fl}$ mice. We observed increased lung compliance and decreased elastance (Figures 5I and 5J), along with delayed whole gut transit time (WGTT) and increased colon length (Figures 5K–5M), consistent with impaired mucosal RTM functions. Finally, given the role of KRM in preventing kidney stone formation[52], we tested this function using sodium oxalate injections and found abnormal oxalate crystal accumulation within the renal medulla of *Lyz2*^{Cre}*Mafb*$^{fl/fl}$ mice, as revealed by Alizarin Red S stain (Figures 5N and 5O). Altogether, our data support that MafB deficiency disrupts RTM phenotypes across multiple tissues and leads to impaired phagocytosis, defective tissue clearance functions, and compromised RTM-mediated homeostatic functions.

MafB directly regulates mac differentiation and identity through *cis*-regulatory elements

Although our data so far position MafB as a key regulator of mac functional identity, its direct targets and the underlying mechanisms remain unclear. To address this, we performed cleavage under targets and release using nuclease (CUT&RUN) for MafB on BMDMs from *Mafb*$^{fl/fl}$ and *Lyz2*^{Cre}*Mafb*$^{fl/fl}$ mice. We identified 7,242 reproducible MafB binding sites in WT BMDMs, whereas MafB-deficient BMDMs yielded only 14 sites (Figures 6A, 6B, and S6A–S6C; Table S4). These sites were distributed across introns (33%), promoters or transcription start

sites (TSS) (31%), intergenic regions (26%), exons (6%), and transcription termination sites (TTS) (2%) (Figure 6C). To connect MafB binding with transcriptional activity, we also performed CUT&RUN for histone H3 lysine 27 acetylation (H3K27ac), a histone mark of active enhancers and promoters. MafB-deficient BMDMs showed reduced H3K27ac tag counts at MafB binding sites compared with controls, supporting that MafB promotes transcriptional activation from these regions (Figures 6D and 6E).

By linking MafB binding sites to genes within ±2 kbp of TSSs, we identified 3,511 MafB targets in BMDMs, including 303 core mac signature genes (Table S2). These included known targets (*C1qa, C1qb*, *C1qc*) and key mac markers (*Csf1r*, *Fcgr1*, *Mertk*) (Figures 6F and 6G). MafB also bound regulatory regions for TFs central to mac differentiation and identity, such as *Zeb2, Mafb* itself, *Maf*, *Spi1* (PU.1), and *Cebpb*[53–55] (Figures 6G and S6D), as well as *Cd163*, consistent with its reduced expression in KCs, RPMs and MHC-II^{+} CMs. To test whether MafB regulated mac signature genes, we performed GSEA and found significant enrichment of MafB target genes in control BMDMs compared to MafB-deficient BMDMs (Figure 6H). Consistently, RTMs from *Lyz2*^{Cre}*Mafb*$^{fl/fl}$ mice showed reduced MafB target scores (Figure S6E).

Next, to assess whether MafB also regulates mac identity in primary RTMs, we performed CUT&RUN for MafB on LPMs from *Mafb*$^{fl/fl}$ or *Lyz2*^{Cre}*Mafb*$^{fl/fl}$ mice. We identified 10,858 reproducible binding sites in WT LPMs, whereas MafB-deficient LPMs yielded fewer than 150 sites (Figures 6I, 6J, and S6F–S6H; Table S4). MafB sites were largely intronic, intergenic, or at promoters (Figure 6K), and ~70% sites and target genes overlapped between BMDMs and LPMs, including core mac identity genes, supporting a conserved MafB program (Figure 6N). In addition, MafB bound LPM-specific genes such as *Pf4* and *Vsig4*, suggesting that MafB also contributes to tissue-specific mac specialization (Figure 6O).

Given the importance of Csf1r signaling to RTM biology[56–58], we assessed its regulation and found *Csf1r* and surface CD115 reduced in multiple RTMs, but not blood monocytes, from *Lyz2*^{Cre}*Mafb*$^{fl/fl}$ mice as compared to controls (Figures S6I and S6J). Altogether, these data suggest that MafB directly imprints mac differentiation and identity though regulation of enhancer and promoter programs.

MafB-driven mac programs are conserved from mouse to human and across vertebrates

To assess whether MafB directly controls conserved *cis*-regulatory elements underlying macrophage identity across species, we first examined the evolutionarily conserved FIRE enhancer in the second intron of *Csf1r*, which regulates mac-specific *Csf1r* transcription.[59–61] MafB bound FIRE (Figure 7A), consistent with predictions of conserved MafB occupancy [62] and with studies showing that FIRE deletion impairs *Csf1r* expression and RTM development.[58] Genome-wide, 91% of MafB binding sites overlapped with *cis*-regulatory elements (cREs) that together represent only 3% of the mouse genome (Figures 7B and 7C). Conservation analysis across 60 vertebrates revealed elevated phastCons and phyloP scores at FIRE (Figures 7A and S7A) and broadly at MafB sites (Figures 7D and 7E), which were more conserved than those of PU.1 (Figures 7D and 7E).

To extend these findings to humans, we performed CUT&RUN for MafB on monocyte-derived macs (MDMs). We identified 24,577 reproducible binding sites, which, similar to mouse BMDMs and LPMs, were predominantly located in introns, intergenic regions, and promoters/TSS (Figures 7F–7H and S7B–S7D; Table S4). Importantly, MafB binding sites and target genes in human MDMs overlapped with 55% of those identified in mouse BMDMs, including at core mac identity genes such as *C1Qs, CSF1R, FCGR1, MERTK, CD163,* and *ZEB2*,

307 indicating a conserved MafB-driven regulatory program between mouse and human (Figures
308 7I–7K).

309 Finally, across diverse vertebrate single-cell atlases, Mafb expression positively correlated
310 with both mac signature genes and conserved MafB target genes (Figures 7L–7N and S7E–
311 S7J), supporting a deeply conserved role for MafB in mac development and the establishment
312 of a core mac identity program.

DISCUSSION

Our study identifies MafB as a pivotal and evolutionarily conserved transcriptional regulator of RTM development, identity and function across diverse tissues. Using conditional gene targeting combined with epigenetic, transcriptomic, phenotypic and functional analyses, we have shown that MafB deficiency disrupted RTM-specific transcriptional programs, altered RTM phenotypes and functions, and impaired tissue homeostasis in mice. Mechanistically, we have shown that MafB directly controlled pivotal mac differentiation and identity genes through *cis*-regulatory elements, establishing a core mac regulatory network preserved across vertebrates.

In the first part of the work, we showed that MafB-deficient BMDMs exhibited impaired differentiation, as reflected by altered morphology together with an immature transcriptomic profile and phenotype. A previous study reports that MafB-deficient macs display increased membrane protrusions[32], a phenotype opposite to our observations. This discrepancy may arise from differences in experimental models, as that study used in vitro-derived macs from fetal liver cells of globally MafB-deficient mice, whereas we analyzed BMDMs from conditionally targeted mice. Of note, in our study, MafB-deficient KCs *in vivo* also showed reduced pseudopods, validating the phenotype observed in BMDMs.

In BMDMs, MafB is activated downstream of Csf1 receptor signaling to orchestrate transcriptional programs critical for mac differentiation and functional identity, as reported.[63,64] A major contribution of this work is the delineation of MafB's direct regulatory network. By identifying over 4,000 MafB binding sites in BMDMs, we provided direct evidence that MafB activated critical mac genes through enhancer and promoter elements, including the evolutionarily conserved FIRE enhancer within the *Csf1r* locus.[59–61]. Of note, MafB's binding sites exhibit greater evolutionary conservation across vertebrates than those of PU.1,

revealing an unappreciated central role in mac biology and suggesting that MafB integrates tissue-specific cues and translates them into core transcriptional programs define RTM identity across diverse tissues and species. Beyond Csf1, the tissue-specific effects of MafB deficiency and the identification of additional MafB target genes in primary LPMs suggest that additional niche-derived factors may modulate MafB activity *in vivo*. Identifying such upstream regulators will clarify how MafB integrates tissue-specific cues to tailor mac phenotypes to their environment. Finally, the extensive dataset of MafB binding sites in mouse BMDMs, LPMs and human MDMs provides a valuable resource for exploring the therapeutic potential of targeting MafB in mac-mediated processes.

Previous studies using transplants from MafB constitutive deficient mice or conditional targeting reported no defects in global mac numbers.[34–36] Using a recently published *Mafb* floxed construct[37], we examined RTMs across tissues and found profound disruptions in transcriptomic profiles, maturity phenotypes and monocyte-to-RTM development in the absence of MafB. Our data are consistent with the idea that, in the absence of MafB, RTMs fail to fully mature and persist in an immature state, irrespective of embryonic or postnatal origin. First, both embryonic RTMs (i.e., MG) and postnatal monocyte-derived RTMs (i.e., CMs) were affected by MafB targeting. Second, immaturity was supported by reduced expression of maturity markers, including Tim4, Vsig4 and CD163 in KCs, Vsig4 in LPMs, P2RY12 in MG, or CD163 in RPMs and in MHC-II^{+} CMs, while the pre-mac markers CD52 remained elevated. Third, downregulation of RTM maturity markers in MG and KCs upon MafB deletion with cell type-specific Cre drivers (Tmem119 for MG, Clec4f for KCs) supported MafB's dual role in both RTM development and maintenance of identity *in vivo*. Finally, our findings are also consistent with the idea that MafB-deficient RTMs fail to adapt to their niches or occupy alternative spatial niches, subsequently leading to phenotypical and functional deficits. Advanced imaging

techniques and spatial proteogenomic approaches will be instrumental in clarifying how RTMs interact with their microenvironment in specific tissues and to what extent such interactions are modulated by MafB.

Our study has demonstrated that MafB deficiency profoundly impairs RTM functions *in vivo*, including phagocytosis, tissue clearance, and multiple homeostatic processes across organs. While the list of functions tested is not exhaustive, the extent of defects observed supports MafB's essential role in sustaining RTM activity and tissue homeostasis. These impairments are likely to have even greater consequences with aging or under environmental, inflammatory, or metabolic stressors, raising the possibility that MafB deficiency predisposes RTMs to dysfunction under challenge. Notably, whereas previous studies report normal mac functionality in the absence of MafB *ex vivo*[32,33], our *in vivo* analyses challenge this notion and reveal clear defects in RTM phagocytosis and clearance functions, highlighting the importance of assessing mac biology in tissue contexts. How MafB integrates stress responses and environmental cues to safeguard RTM functions over the lifespan represents exciting perspectives for future research.

In conclusion, our study has explored MafB's pivotal role in shaping RTM populations and revealed its indispensable function in orchestrating global and subset-specific RTM transcriptional programs, phenotypes and functions via direct regulation of conserved cis-regulatory elements essential for mac core identity.

Limitations

First, the mouse experiments were conducted in a single syngeneic mouse background, using relatively young mice raised under SPF conditions, and focused primarily on prominent RTM populations. Caution is therefore when extrapolating these findings to other genetic

385 backgrounds, age groups, health conditions, or less well-characterized RTM subsets. Second,
386 while *in silico* analyses suggest conservation of MafB functions across species, most
387 experiments were conducted in mice. Although we provide epigenetic profiling of human
388 MDMs, supporting conservation of MafB-driven programs across species, additional loss-of-
389 function studies will be required to validate MafB's role in regulating human mac maturation
390 and function. Third, while epigenetic analyses of mouse BMDMs and one primary RTM subset
391 (LPMs) revealed tissue-specific effects, expanding such analyses to a broader range of RTMs
392 will be necessary to fully capture the diversity of MafB regulatory programs, despite the
393 technical challenges posed by these rare populations. Finally, future studies employing
394 CRISPRi-mediated perturbation of MafB-bound regulatory elements will be necessary to
395 functionally validate the regulatory role of these sites in controlling target gene expression.

RESOURCE AVAILABILITY

Lead contact

Reagent and resource requests should be addressed to and will be fulfilled by the lead contact, Thomas Marichal (t.marichal@uliege.be).

Materials availability

This study did not generate new unique reagents.

Data and code availability

Bulk RNA-Seq, single-cell RNA-Seq and CUT&RUN data have been deposited at GEO and are publicly available under accession GSE287347.

All codes for analysis of sequencing data have been deposited at GitHub and are publicly available at: https://github.com/dovneste/MafB_Mac.

ACKNOWLEDGEMENTS

We thank all members of the Immunophysiology Laboratory (GIGA Institute, Liège, Belgium) for discussions; S. Ormenese, R. Stefan, A. Hego, G. Lefevre, and C. Vanwinge from the GIGA In Vitro Imaging Platform; P. Drion, N. Moula, G. Lambert, and all staff members from the GIGA Mouse Facility and Transgenics Platform; W. Coppieters, L. Karim, M. Deckers, A. Mayer, A. Lavergne, and members from the GIGA Genomics Platform; and R. Fares, I. Sbai, and A. Lio for excellent technical and administrative support; O. Butovsky for sharing the Fcrls antibody; MT Ysebaert for statistical advices.

Thomas Marichal acknowledges support from the F.R.S.-FNRS (Incentive Grant for Scientific Research), from the FRFS-Welbio, from the Acteria Foundation and from an ERC Starting Grant (ERC StG 2018 IM-ID: 801823). Thomas Marichal is supported by a Research Project Grant of the F.R.S.-FNRS, by a FRFS-Welbio Advanced Grant (WELBIO-CR-2022A-10), by an ERC Consolidator Grant (ERC CoG 2023 MoMacTrajectALI: 101124390), by the Baillet Latour Fund and by the Léon Fredericq Foundation. Coraline Radermecker is a Research Associate of the F.R.S.-FNRS and is supported by the Baillet Latour Fund. This research was supported by the European Regional Development Fund (FEDER-SYSTIMM).

AUTHOR CONTRIBUTIONS

T.M. and D.V. conceived the project and designed the experiments. D.V. did most of the experiments, compiled the data and prepared the figures. W.P. helped with *in vivo*-related experiments. Z.L. and C.L.S. performed confocal microscopy experiments and analyzed KC-specific Maf/MafB-deficient mice. M.H. prepared MDM. R.L.R. analyzed KC morphology. J.A. and DV performed all the bioinformatic analyses. A.B. and B.M. helped with isolation and analysis of CM. F.P. and D.C. performed the invasive measurements of lung function. A.H. analyzed BMDM morphology. P.C. performed electron microscopy experiments. F.B. generated myeloid-restricted MafB-deficient mice and F.B. and C.R. helped with the initial characterization of those mice. T.M. and D.V. wrote the manuscript. All authors provided feedback on the manuscript. T.M. supervised and secured funding for the project.

DECLARATION OF INTERESTS

The authors declare no competing interests.

Figure legends

Figure 1. Elevated MafB expression and activity define mature RTMs in mice

(A) Heatmap showing the top 50 genes upregulated in macs compared with monocytes (Mo) and DCs, inferred from microarray data on the Gene Expression Commons platform.

(B) UMAP of myeloid cell transcriptional identity from the Tabula Muris Senis (TMS) dataset.

(C) Feature plot of *Mafb* expression, as in B.

(D) Violin plot of *Mafb* expression across myeloid cell clusters, as in C (height, expression; width, cell abundance).

(E) Feature plot of MafB activity inferred with decoupleR, as in B.

(F) Violin plot of MafB activity across myeloid cell clusters, as in E.

(G) Bar graphs of MafB expression in blood Mo (blue) and RTM (red) populations, measured byflow cytometry (n = 4).

(H) Bar graphs of MafB expression in DC and RTM populations from indicated organs, measured by flow cytometry (n = 4).

(I) Scatter plot of Ly6C and MHC-II expression in colon $CD45^+Lin^-F4/80^+CD64^+$ cells colored by Wanderlust pseudotime (merged from 4 mice).

(J) MafB expression along pseudotime, as in I.

(K) Scatter plot of Ly6C and F4/80 expression in $CD45^+Lin^-CD11b^+CD115^+$ peritoneal cells colored by Wanderlust pseudotime (merged from 4 mice).

(L) MafB expression along pseudotime, as in K.

Data are mean ± SEM (G and H). *P* values were calculated using one-way ANOVA with Tukey's post hoc test (G), two-tailed Student's t test (H, spleen, kidney, and colon), or one-way ANOVA with Dunnett's post hoc test (H and other organs). *, $P < 0.05$; **, $P < 0.01$; ***, $P < 0.001$;

460 ****, $P < 0.0001$. cDC, conventional DC; C LPM, colonic lamina propria macs; cMoP, common
461 Mo progenitors;DM, dermal macs; GMP, granulocyte–monocyte progenitors; LC, Langerhans
462 cells; LCM, liver capsular macs; LN, lymph node; MFI, mean fluorescence intensity; MLN,
463 mesenteric lymph nodes; Neu, neutrophils; pDC, plasmacytoid DC; pMo, patrolling Mo; RM,
464 resident mac; SI LPM, small intestinal lamina propria macs; SI MM, small intestinal muscularis
465 macs; SLN, skin-draining lymph nodes.
466
467 See also Figure S1.

Figure 2. MafB deficiency impedes monocyte-to-mac development and mac functional identity *ex vivo.*

(A) Experimental outline.

(B) Representative phase-contrast images of BMDM (n = 3). Scale bar, 100 μm.

(C) Representative scanning electron microscopy images of BMDM, as in B (n = 3). Scale bar, 20 μm.

(D) Volcano plot of DEGs between BMDM from *Mafb*$^{fl/fl}$ and *Lyz2*^{Cre}*Mafb*$^{fl/fl}$ mice (n = 4 mice/group). Transcripts enriched in *Mafb*$^{fl/fl}$ and *Lyz2*^{Cre}*Mafb*$^{fl/fl}$ BMDM are shown in blue and red, respectively ($\log_2$ fold change > 1 or < −1; adjusted $P < 0.05$).

(E) Heatmap of DEGs, as in D.

(F) GSEA of Mo and Mac signature genes in DEGs, as in D.

(G) Bar graphs of mRNA and protein expression of Mo and Mac markers (n = 4–7).

Data are mean ± SEM, pooled from two independent experiments (G). *P* values were calculated using a Wald test with Benjamini–Hochberg correction (D and G [mRNA]) or a two-tailed Student's t test (G [protein]). **, $P < 0.01$; ***, $P < 0.001$; ****, $P < 0.0001$. FDR, false discovery rate; NES, normalized enrichment score; TPM, transcripts per kilobase million.

See also Figure S2 and Tables S1 and S2.

Figure 3. Global and subset-specific RTM signatures are disrupted upon myeloid-intrinsic MafB depletion *in vivo*.

(A) Experimental outline.

(B) Bar graphs of donor WT, donor *Lyz2*^{Cre}*Mafb*$^{fl/fl}$, and host chimerism in blood Neu, Mo, and RTM populations, as in A (n = 5–8).

(C) Heatmap of the percentage of WT donor cells relative to total donor chimerism, as in B.

(D) Experimental outline.

(E) UMAP plot of RTM transcriptional identity from *Mafb*$^{fl/fl}$ and *Lyz2*^{Cre}*Mafb*$^{fl/fl}$ mice.

(F) Dot plot of average expression and percentage of cells expressing the indicated genes within RTM populations, as in E.

(G) Violin plots of RTM subset-specific signature scores in *Mafb*$^{fl/fl}$ and *Lyz2*^{Cre}*Mafb*$^{fl/fl}$ RTMs (height, score; width, abundance).

(H) Violin plots of EMP, pre-Mac, and Mac signature scores in RTM populations from *Mafb*$^{fl/fl}$ and *Lyz2*^{Cre}*Mafb*$^{fl/fl}$ mice.

(I) UMAP of transcriptional identity (top) and pseudotime trajectory (bottom) of fetal liver EMP, pre-Mac, and Mac at embryonic day E14.5.

(J) Gene expression of *Cd52* (top) and Mafb (bottom) along pseudotime, as in I.

(K) Violin plot of *Cd52* expression across RTM populations of *Mafb*$^{fl/fl}$ and *Lyz2*^{Cre}*Mafb*$^{fl/fl}$ mice (height, expression; width, abundance).

(L) Bar graphs of CD52 expression in SPM, LPM, KC, and IM, assessed by flow cytometry in *Mafb*$^{fl/fl}$ and *Lyz2*^{Cre}*Mafb*$^{fl/fl}$ mice (n = 5).

Data are mean ± SEM and are pooled from two independent experiments (B and L). *P* values were calculated using a one-way ANOVA with Sidak's post hoc test (C), a Wilcoxon rank-sum

511 test (G, H, and K) or a two-tailed Student's t test (L). *, $P < 0.05$; **, $P < 0.01$; ***, $P < 0.001$;

512 ****, $P < 0.0001$.

513

514 See also Figure S3 and Tables S2 and S3.

Figure 4. Myeloid-specific MafB-deficient mice exhibit drastic changes in the proportion and phenotype of tissue RTMs.

(A) Representative contour plots of MHC-II and F4/80 expression in peritoneal $CD45^+Lin^-Ly6C^-CD11b^+CD115^+$ cells from $Mafb^{fl/fl}$ and $Lyz2^{Cre}Mafb^{fl/fl}$ mice (left) and percentages of SPM and LPM, as gated on the contour plots (right) (n = 7–9). All subsequent panels compare $Mafb^{fl/fl}$ and $Lyz2^{Cre}Mafb^{fl/fl}$ mice.

(B) Absolute numbers of SPM and LPM, as in A.

(C) Histograms (top) and bar graphs (bottom) of MHC-II and RELMα expression in SPM, as in A.

(D) Histograms (top) and bar graphs (bottom) of F4/80, MerTK, Tim4, and Vsig4 expression in LPM, as in A.

(E) Representative contour plots of F4/80 and CD11b expression in liver $CD45^+Lin^-Ly6C^-$ cells (left) and percentages of $F4/80^-CD11b^{lo}$ cells, $CD11b^{hi}$ Mo-Macs, and KCs, as gated on the contour plots (right) (n = 8).

(F) Absolute numbers of $CD11b^{hi}$ Mo-Macs and KCs, as in E.

(G) Histograms (top) and bar graphs (bottom) of MerTK, Clec4F, Tim4, Vsig4, FR-β, and CD163 expression in KCs, as in E.

(H) Representative contour plots of CD206 and MHC-II expression in brain $CD45^+Lin^-Ly6C^-F4/80^+CD64^+$ cells (left) and percentages of MG and BAM , as gated on the contour plots (right) (n = 6–8).

(I) Absolute numbers of MG and BAM, as in H.

(J) Histograms (top) and bar graphs (bottom) of P2RY12 and FCRLS expression in MG, as in H.

(K) Representative contour plots of CD206 and MHC-II expression in BAM (left) and percentages of $MHC\text{-}II^-$ and $MHC\text{-}II^+$ BAM, as gated on the contour plot (right) (n = 6–8).

(L) Absolute numbers of MHC-II$^-$ and MHC-II$^+$ BAM, as in K.

(M) Representative contour plots of CD206 and CD11b expression in spleen CD45$^+$Lin$^-$Ly6C$^-$F4/80$^+$CD64$^+$ cells (left) and percentages of RPM and CD11b$^+$ mac, as gated on the contour plots (right) (n = 6–7).

(N) Absolute numbers of RPM and CD11b$^+$ macs, as in M.

(O) Histograms (top) and bar graphs (bottom) of CD163 expression in RPM, as in M.

Data are mean ± SEM and are pooled from two independent experiments. *P* values were calculated using a two-tailed Student's t test. *, $P < 0.05$; **, $P < 0.01$; ***, $P < 0.001$; ****, $P < 0.0001$. ns, not significant.

See also Figures S4 and S5.

Figure 5. MafB deficiency impacts essential core and tissue-specific RTM functions.

(A) Experimental outline.

(B) Representative histograms (left) and bar graphs (middle, right) of *S. aureus* pHrodo-Red Bioparticle uptake in LPMs, depicting the percentage of pHrodo$^+$ cells (middle) and MFI (right), as in A (n = 6–7).

(C) Experimental outline.

(D) Representative histograms (left) and bar graphs (middle, right) of *S. aureus* pHrodo-Red Bioparticle uptake in KCs, depicting the percentage of pHrodo$^+$ cells (middle) and MFI (right), as in C (n = 5).

(E) Experimental outline.

(F) Representative histograms (left) and bar graphs (middle, right) of sRBC-PKH26 uptake in RPMs, depicting the percentage of PKH26$^+$ cells (middle) and MFI (right), as in E (n = 5–6).

(G) Representative images (top) and bar graphs of spleen weight (bottom) from *Mafb*$^{fl/fl}$ and *Lyz2*^{Cre}*Mafb*$^{fl/fl}$ mice (n = 6). Scale bar, 0.5 cm.

(H) Representative images of spleens from *Mafb*$^{fl/fl}$ and *Lyz2*^{Cre}*Mafb*$^{fl/fl}$ mice stained with Perl's Prussian blue to examine iron deposition (left; overview, scale bars 1 mm; bottom, magnified views, scale bars 200 µm) and bar graphs of Prussian blue$^+$ area (right) (n = 6).

(I) Experimental outline.

(J) Bar graphs of lung compliance (left) and elastance (right) from *Mafb*$^{fl/fl}$ and *Lyz2*^{Cre}*Mafb*$^{fl/fl}$ mice measured by FlexiVent assay, as in I (n = 5–9).

(K) Experimental outline.

(L) Bar graphs of WGTT, as in K (n = 3–4).

(M) Representative images (left) and bar graphs of colon length (right) from *Mafb*$^{fl/fl}$ and *Lyz2*^{Cre}*Mafb*$^{fl/fl}$ mice (n = 6–8). Scale bar, 2 cm.

(N) Experimental outline.

(O) Representative images of kidneys from *Mafb*$^{fl/fl}$ and *Lyz2*^{Cre}*Mafb*$^{fl/fl}$ mice stained with Alizarin Red S to examine CaOx crystal deposition (left; overview, scale bars 1 mm; inset, magnified views, scale bars 500 µm) and bar graphs of Alizarin Red S^{+} area (right), as in N (n = 4–6).

Data are mean ± SEM and are pooled from two independent experiments. *P* values were calculated using a two-tailed Student's t test. *, $P < 0.05$; **, $P < 0.01$; ****, $P < 0.0001$.

Figure 6. MafB binds to *cis*-regulatory elements to promote transcription of key mac differentiation and identity genes.

(A and B) Histograms (left) and heatmaps (right) (A) and scatterplot (B) of normalized tag counts at MafB peaks in BMDMs from *Mafb*$^{fl/fl}$ and *Lyz2*^{Cre}*Mafb*$^{fl/fl}$ mice, as quantified by CUT&RUN.

(C) Genomic distribution of MafB binding sites in BMDMs.

(D and E) Histograms (D) and scatterplot (E) of normalized H3K27ac tag counts at MafB binding sites in BMDMs from *Mafb*$^{fl/fl}$ and *Lyz2*^{Cre}*Mafb*$^{fl/fl}$ mice, as quantified by CUT&RUN.

(F) Venn diagram showing the overlap between mac signature genes and MafB target genes in BMDMs.

(G) CUT&RUN tracks depicting MafB binding around representative mac signature genes in BMDMs from *Mafb*$^{fl/fl}$ and *Lyz2*^{Cre}*Mafb*$^{fl/fl}$ mice, visualized with the integrative genome viewer (IGV). Horizontal red bars, MafB binding sites in BMDMs.

(H) GSEA of mac-specific MafB target genes using bulk RNA-seq data from BMDMs of *Mafb*$^{fl/fl}$ and *Lyz2*^{Cre}*Mafb*$^{fl/fl}$ mice.

(I and J) Histograms (left) and heatmaps (right) (I) and scatterplot (J) of normalized tag counts at MafB peaks in LPMs from *Mafb*$^{fl/fl}$ and *Lyz2*^{Cre}*Mafb*$^{fl/fl}$ mice, as quantified by CUT&RUN.

(K) Genomic distribution of MafB binding sites in LPMs.

(L and M) Venn diagrams showing the overlap between MafB binding sites (L) and target genes (M) in LPMs and BMDMs.

(N and O) CUT&RUN tracks depicting MafB binding around indicated mac (N) and LPMs (O) signature genes in LPMs, visualized with IGV. Horizontal green bars, MafB binding sites in LPMs.

607 *P* values were calculated using a Wilcoxon signed rank test (E) or a permutation test (H).

608

609 See also Figure S6 and Table S4.

Figure 7. MafB binding sites and MafB-dependent regulation of mac identity are highly conserved across species.

(A) CUT&RUN tracks depicting MafB binding at the FIRE enhancer within the second intron of the *Csf1r* gene in BMDMs from *Mafb*$^{fl/fl}$ and *Lyz2*^{Cre}*Mafb*$^{fl/fl}$ mice (top), and phastCons and phyloP conservation scoring tracks around the FIRE enhancer (bottom), visualized with IGV. Horizontal red bars, MafB binding sites in BMDMs; horizontal blue bar, FIRE enhancer.

(B) Genomic distribution of cREs in mice.

(C) Overlap between MafB binding sites in BMDMs and cREs.

(D and E) Distribution of mean phastCons (D) and phyloP (E) scores around PU.1 and MafB binding sites (−500 to +500 bp from peak center).

(F and G) Histograms (left) and heatmaps (right) (F) and scatterplot (G) of normalized tag counts at MafB peaks in MDMs, as quantified by CUT&RUN.

(H) Pie chart showing the genomic distribution of MafB binding sites in MDMs.

(I and J) Venn diagrams showing the overlap between MafB binding sites (I) and target genes (J) in human MDMs and mouse BMDMs.

(K) CUT&RUN tracks depicting MafB binding around representative mac signature genes in MDMs, visualized with IGV. Horizontal purple bars, MafB binding sites in MDMs; horizontal red bars, conserved MafB binding sites in human MDMs and mouse BMDMs, as in I.

(L) Overview of cross-species single-cell RNA-seq datasets from mouse (TMS), human (TS), mouse lemur (TM), pig (PCA), clawed frog (XCL), and zebrafish (ZCL), used to calculate correlations of *Mafb* expression with mac and conserved MafB target gene signature scores, as in Figure S7E–J.

(M and N) Heatmaps of Pearson correlations between *Mafb* expression and either mac (M) or conserved MafB target gene (N) signature scores across species, as in L.

634

635 *P* values were calculated using a pairwise Wilcoxon signed-rank test with Benjamini–Hochberg

636 correction (D and E) or a Wilcoxon signed rank exact test (M and N). **, $P < 0.01$;

637 ****$P < 0.0001$.

638

639 See also Figure S7 and Table S4

STAR ★ Methods

EXPERIMENTAL MODEL AND STUDY PARTICIPANT DETAILS

In vivo animal studies

The following mice on the C57BL/6 background were used: CD45.2 WT C57BL/6J (The Jackson Laboratory), CD45.1 WT C57BL/6J (The Jackson Laboratory, 002014), *Maf*$^{fl/fl}$[65], *Mafb*$^{fl/fl}$[37], *Lyz2*^{Cre} [66] (The Jackson Laboratory, 004781), *Clec4f*^{Cre}[53], and *Tmem119*^{CreERT2}[67] (The Jackson Laboratory, 031820). Myeloid-restricted *Mafb* depletion was achieved by crossing *Mafb*$^{fl/fl}$ mice with *Lyz2*^{Cre} mice. The corresponding littermate control mice were *Mafb*$^{fl/fl}$ mice. KC-specific Maf/MafB-deficient mice were generated by crossing *Maf*$^{fl/fl}$*Mafb*$^{fl/fl}$ mice with *Clec4f*^{Cre} mice, with *Maf*$^{fl/fl}$*Mafb*$^{fl/fl}$ littermates serving as controls. MG-specific MafB-deficient mice were obtained by crossing *Tmem119*^{CreERT2} mice with *Mafb*$^{fl/fl}$ mice, with recombination induced by oral gavage of tamoxifen (5 mg/day for 5 consecutive days); corn oil–treated littermates were used as controls. CD45.1.2 mice were generated by crossing CD45.1 with CD45.2 mice.

No differences between sexes were observed in pilot experiments. Each experiment included both male and female mice aged 6 to 10 weeks, except for chimera experiments, which used mice aged 11 to 15 weeks. The mice were bred and housed under specific-pathogen-free conditions at the GIGA Institute (Liège University, Belgium), maintained on a 12-hour light-dark cycle, with access to standard chow and water *ad libitum*. Mice were identified by genotype, and all experiments were conducted using age- and sex-matched littermates. Investigators were not blinded during data collection and analysis.

All animals and experimental procedures, except experiments involving *Clec4f*^{Cre}*Maf*$^{fl/fl}$*Mafb*$^{fl/fl}$ mice were reviewed and approved by the Institutional Animal Care and Use Committee of the University of Liège (ethical approval no. 1956 & 2462).

664 *Clec4f*^{Cre}*Maf*$^{fl/fl}$*Mafb*$^{fl/fl}$ mice were bred and maintained at the VIB (Belgium) in accordance
665 with the ethical committee of the Faculty of Science, UGent and VIB (ethical approval no.
666 LN1691). The study adhered to the "Guide for the Care and Use of Laboratory Animals" from
667 the Institute of Laboratory Animal Resources, National Research Council, published by the
668 National Academy Press, as well as relevant European and local legislation. Temperature and
669 relative humidity were maintained at 21°C and 45–60%, respectively.
670
671 **METHOD DETAILS**
672 **Isolation of blood, bone marrow and tissue leukocytes**
673 Blood was collected through retro-orbital plexus bleeding from terminally anesthetized mice.
674 Red blood cells were lysed in ACK lysis buffer (155 mM NH_4Cl [VWR, 21235.297], 10 mM $KHCO_3$
675 [Sigma-Aldrich, 60338], 0.1 mM EDTA [Merck Millipore, 1084181000]). Mice were then
676 sacrificed by cervical dislocation. Peritoneal lavage was obtained by injecting 10 ml PBS
677 (Thermo Fisher Scientific, 14190094) containing 10 mM EDTA into the peritoneal cavity and
678 collecting the washout. Mice were then perfused with 20 ml PBS though the left ventricle, and
679 liver, kidney, lung, small intestine, colon and brain were dissected.
680 For BM cell preparation, femurs and tibias were dissected and cleaned of muscle tissue.
681 Bones were opened at the knee joint with a razor blade, and BM was spun out by
682 centrifugation. Cell pellets were resuspended in ice-cold PBS containing 10 mM EDTA and cell
683 suspensions were filtered using a cell strainer (70 µm, Corning, 352350) to obtain a single-cell
684 suspension.
685 Spleen leukocytes were isolated by crushing the spleen through a 70 µm cell strainer with a
686 syringe plunger. Red blood cells were lysed in ACK lysis buffer.

687 Liver, kidney, lung and brain were diced into small pieces with razor blades, and digested for
688 1 h at 37 °C in RPMI (Thermo Fisher Scientific, 21875034) containing 10% vol/vol FBS (Thermo
689 Fisher Scientific, A3160802), 1 mg/ml collagenase IV (Thermo Fisher Scientific, 17104019) and
690 0.05 mg/ml DNase I (Sigma-Aldrich, 11284932001). After 45 min of digestion, the suspension
691 was homogenized using an 18-gauge needle. Ice-cold PBS containing 10 mM EDTA was added
692 to stop the digestion process and cell suspensions were filtered using a 70 µm cell strainer.
693 Red blood cells were lysed in ACK lysis buffer. Lung mononuclear leukocytes were enriched by
694 Percoll (GE Healthcare) density gradient centrifugation and collecting cells from the
695 1.080:1.038 g/ml interface. Brain leukocytes were enriched by Percoll density centrifugation
696 and harvesting cells at the 80%:40% interface.

697 For gut leukocyte collection, small intestine and colon were washed in ice-cold PBS and
698 remaining fat tissue and Peyer's patches were removed. The intestines were opened
699 longitudinally, cut into segments of 3–4 mm and washed in ice-cold HBSS (Thermo Fisher
700 Scientific, 14025-050) with 2% FBS. To remove mucus and epithelial cells, intestines were
701 incubated with HBSS containing 2 mM EDTA and 1 mM 1,4-Dithiothreitol (DTT) (Sigma-Aldrich,
702 10708984001) at 37°C with agitation for 20 min followed by an incubation in HBSS
703 supplemented with 2 mM EDTA at 37°C with agitation for 40 min. The remaining tissue was
704 washed in ice-cold PBS and digested for 1 h at 37 °C with agitation in RPMI containing 5% FBS,
705 1 mg/ml collagenase VIII (Sigma-Aldrich, C2139) and 0.05 mg/ml DNase I. Ice-cold PBS
706 containing 2 mM EDTA was added to stop the digestion process and cell suspensions were
707 filtered using a 70 µm cell strainer.

708 For skin preparation, ears were dissected, separated in dorsal and ventral sections, and
709 digested for 90 min at 37 °C in HBSS supplemented with 5 U/ml Dispase (Sigma-Aldrich,
710 D4693). Dorsal and ventral sections were cut into small pieces using scissors, and further

digested for 1 h at 37°C in RPMI containing 10% FBS, 1 mg/ml collagenase IV and 0.05 mg/ml DNase I. After 45 min of digestion, the suspension was homogenized using an 18-gauge needle. Ice-cold PBS containing 10 mM EDTA was added to stop the digestion process and cell suspensions were filtered using a 70 µm cell strainer.

Flow cytometry and cell sorting

Cells ($0.5–5 \times 10^6$) were pre-incubated for 10 min at 4 °C with Mouse BD Fc Block (BD Biosciences, 553142) to block unspecific binding to Fc receptors. Cells were then stained with fluorophore-conjugated antibodies for 30 min at 4°C. Lineage markers used RTM analysis included CD3e, CD19, CD49b, Ly6G and SiglecF. For MafB staining, extracellular-stained cells were permeabilized using FoxP3 Transcription Factor Staining Kit (eBioscience™, 00-5523-00), stained with anti-MafB antibody (Bethyl, A700-046) and secondary AF488 Goat anti-Rabbit IgG (H+L) (Thermo Fisher Scientific, A11008) or AF647 Donkey anti-rabbit IgG (Biolegend, 406414). Stained cell suspensions were maintained at 4 °C and analyzed with an LSR Fortessa (BD Biosciences). For scRNA-seq, RTM were sorted using a MA900 (Sony). Dead cells were excluded using by LIVE/DEAD Fixable Near-IR (775) stain (Thermo Fisher Scientific, L34976). The full list of antibodies used for flow cytometry can be found in the Key Resources Table. Flow cytometry data were analyzed using FlowJo software (TreeStar).

Wanderlust pseudotime

On flow cytometry data, $CD45^+Lin^-F4/80^+CD64^+$ colon cells and $CD45^+Lin^-CD11b^+CD115^+$ peritoneal cells were gated, down sampled (1×10^4 cells/ sample) and concatenated using FlowJo. Wanderlust pseudotime[68] was calculated on concatenated flow cytometry data based

on Ly6C and MHC-II expression or Ly6C and F4/80 expression for colon and peritoneal cells, respectively.

Bone marrow-derived macrophage differentiation

BMMos were isolated from BM using Monocyte Isolation Kit (BM) (Miltenyi Biotec, 130100629) and were seeded in tissue culture-treated plates and cultured for 4 days in RPMI supplemented with 10% FBS, 1 mM Sodium Pyruvate (Thermo Fisher Scientific, 11360070), 1X Minimum Essential Medium Non-Essential Amino Acids (MEM NEAA; Thermo Fisher Scientific, 11140050), 50 µM β-mercaptoethanol (Thermo Fisher Scientific, 31350010) and 40 ng/ml Csf-1 (Peprotech, 31502) to differentiate them into BMDMs.

Scanning electron microscopy

Fifty thousand BMMos from *Mafb*$^{fl/fl}$ or *Lyz2*^{Cre}*Mafb*$^{fl/fl}$ mice were isolated, seeded on discoid coverslips in tissue culture-treated 24-well plates (Greiner, 662160) and differentiated into BMDMs, as described above. After 4 days, the cells were washed with PBS and fixed for 2 hours in 2.5% glutaraldehyde prepared in 0.1 M sodium cacodylate buffer (pH 7.2). Following fixation, the cells were rinsed in 0.2 M cacodylate buffer and MilliQ water, then post-fixed for 1 hour in aqueous 1% osmium tetroxide. The cells were washed three times with MilliQ water and subsequently dehydrated through a graded ethanol series (30%, 50%, 70%, 90%, and 100%). After three rinses in absolute ethanol, the glass coverslips containing the cells were dried with CO_2 using a critical point dryer (Leica EM CPD300). The dried coverslips were fixed to glass slides using double-sided carbon tape and coated with a 20 nm layer of gold using a Balzers SCD 004 sputter coater (Balzers). Imaging was performed using a Tescan Clara FEG-

SEM (Tescan) equipped with an Everhart-Thornley secondary electron detector under an accelerating voltage of 15 kV.

Cell morphology

Fifty thousand BMMos from *Mafb*$^{fl/fl}$ or *Lyz2*^{Cre}*Mafb*$^{fl/fl}$ mice were isolated, seeded in a CELLview™ Advanced TC™ petri dish (Greiner, 627975) and differentiated into BMDMs, as described above. After 4 days, differential interference contrast (DIC) images of BMDM cells were acquired using a Zeiss Axio Observer microscope equipped with a 25×/0.8 DIC oil immersion objective and an AxioCam 506 monochromatic camera. For cell segmentation in DIC images, the pre-trained LC2 model of Cellpose 2.0 was retrained with a set of annotated images to enhance its performance and better capture the morphological characteristics of the cells. Predictions were automated using FIJI (1.54) with an ImageJ macro and the BIOP plugin. Morphological characteristics of the segmented cells, including area, perimeter, circularity, roundness, solidity and Feret diameter, were extracted from the masks generated by Cellpose 2.0. One hundred cells were analyzed per biological replicate and three biological replicates were analyzed per group.

Bulk RNA sequencing library preparation

Two hundred fifty thousand BMMos from *Mafb*$^{fl/fl}$ or *Lyz2*^{Cre}*Mafb*$^{fl/fl}$ mice were isolated, seeded in tissue culture-treated 6-well plates (Greiner, 657160) and differentiated into BMDMs, as described above. After 4 days, non-adherent cells were washed off with ice-cold PBS and total RNA was isolated with the standard TRIzol (Thermo Fisher Scientific, 15596018) RNA extraction protocol. Total RNA was further purified and concentrated using a RNA Clean & Concentrator Kit (Zymo Research, R1013) according to manufacturer's instructions. RNA

quality and quantity were evaluated using a 5200 Fragment Analyzer (Agilent). Samples with a RIN > 9.9 were selected for sequencing. One hundred nanograms of RNA was used to generate the libraries using the TruSeq Stranded mRNA kit (Illumina, 20020594). These libraries were sequenced on an NovaSeq 6000 (Illumina) sequencer on an S4 flow cell.

Bulk RNA sequencing analysis

Preprocessing, alignment to the mouse genome (GRCm38/mm10), sequence counting, and quality control of the bulk RNA-Seq data were carried out with the *nf-core/rnaseq* pipeline. RNA-Seq data were further analyzed using R Bioconductor (4.2.3) and the DESeq2 package (1.38.3)[69]. DEGs were calculated using the DESeq function. Gene Ontology (GO) enrichment analyses on DEGs was performed using the *dag_enrich_on_genes* function from the simona package .

Gene Set Enrichment Analysis

For bulk RNA-Seq, GSEA was performed using GSEA software (4.1.0). In brief, genes from gene sets were ranked according to their expression in $Mafb^{fl/fl}$ BMDM and $Lyz2^{Cre}Mafb^{fl/fl}$ BMDMs using the *Signal2Noise* method. The Normalized Enrichment Score (NES), False Discovery Rate (FDR), and nominal *P*-values were determined through 1000 sample permutations across different phenotypes.

Monocyte signature genes and mac signature genes were retrieved by comparing gene expression between monocytes and macs in the ImmGen database using the ImmGen Population Comparison data browser.

Bone marrow chimeras

For mixed bone marrow competitive chimeras, CD45.1.2 mice received two doses of 5.5 Gy lethal irradiation, 15 minutes apart, and were reconstituted by intravenous injection of 10^7 bone marrow cells, consisting of a 1:1 mix of cells from CD45.1 WT and CD45.2 *Lyz2*^{Cre}*Mafb*$^{fl/fl}$ mice. Starting from the day of irradiation, mice were treated with enrofloxacin (0.05 mg/ml; Baytril, Bayer) in their drinking water for 4 weeks. Four weeks after irradiation, blood chimerism was evaluated by flow cytometry.

Single-cell RNA sequencing library preparation

Two independent scRNA-seq experiments were performed. In the first experiment, peritoneal macrophages and liver macrophages were isolated. In the second experiment, colonic and brain macrophages were isolated. For each experiment, cells were FACS-sorted from *Lyz2*^{Cre}*Mafb*$^{fl/fl}$ mice and *Mafb*$^{fl/fl}$ littermate controls.

Specifically, in the first experiment we sorted 5 × 10^4 CD45+Lin−Ly6C−CD11b+CD115+ live cells from the peritoneal lavage and 5 × 10^4 CD45$^+$Lin$^-$Ly6C$^-$CD11b$^{int/+}$F4/80$^+$CD64$^+$ live cells from the liver. In the second experiment we sorted 5 × 10^4 CD45$^+$Lin$^-$CD11b$^+$F4/80$^+$CD64$^+$ live cells from the colon and 5 × 10^4 CD45$^+$Lin$^-$Ly6C$^-$CD11b$^+$F4/80$^+$CD64$^+$ live cells from the brain. Sorting was performed in PBS with 5% FBS. Sorted cells were barcoded with TotalSeq™-B anti-mouse Hashtag antibodies (Biolegend). Hashtag barcoded cells were washed, pooled per genotype, spun down and resuspended in PBS with 0.04% UltraPure™ BSA (Thermo Fisher Scientific, AM2616) at an estimated final concentration of 1000 cells/µl. Cell suspensions were loaded into the Chromium iX (10x Genomics) at a target recovery of 2 x 10^3 cell per sorted population and single-cell RNA-Seq libraries were prepared using Chromium Single Cell 3' GEM, Library & Gel Bead Kit v3.1 (10x Genomics, 1000128) according to demonstrated 10x Genomics protocol "Next GEM Single Cell 3' Reagent Kits v3.1 with Feature Barcoding

technology for Cell Surface Protein" (CG000206 Rev D). In brief, single-cell Gene Expression Matrices (GEMs) were generated by combining barcoded Single Cell 3' v3.1 Gel Beads, a Master Mix, and hashtag-labeled cells with Partitioning Oil on a Chromium Chip G (10x Genomics). Reverse transcription was performed using a Veriti Thermocycler (Thermo Fisher Scientific) at 53°C for 45 minutes, 85°C for 5 minutes, and holding at 4°C. Next, GEMs were disrupted, and pooled fractions were purified using DynaBeads MyOne Silane Beads (10x Genomics, No. 2000048). Full-length cell-barcoded cDNA and hashtag were amplified via PCR with a 12-cycle reaction module at 98°C for 3 minutes, 11 cycles at 98°C for 15 seconds, 63°C for 20 seconds, and 72°C for 1 minute, followed by a final extension at 72°C for 1 minute. Feature cDNA Primer 2 (PN2000097, 10x Genomics) was used to amplify both cDNA and hashtag. The cDNA reaction was purified and size-selected for library preparation using SPRI Beads (Beckman Coulter). The supernatant, containing Cell barcoded hashtag amplicons, was separated and purified again for hashtag library preparation. For 3' Gene Expression library construction, amplified cDNA was fragmented and size-selected. Adaptors (read 2 sequences) were added through End Repair, A-tailing, and partial Adaptor Ligation. Libraries were then amplified by PCR (indexing PCR) using different dual index primers per sample (PN-3000431 Dual Index Plate TT Set A). Purified hashtag amplicons were processed in an indexing PCR using Feature SI Primers 2 (PN2000099, 10x Genomics) with single index primers (PN-2000240 Single Index Plate T Set A, 10x Genomics). Both the 3' Gene Expression and hashtag libraries were quality-checked on QIAxel and quantified by qPCR using Kapa SyberFast (Roche). Libraries were sequenced on an NovaSeq 6000 (Illumina) using an S4 flow cell for paired-end 150 cycles, but demultiplexed with read 1: 28 cycles; read 2: 91 cycles; index i7: 10 cycles; index i5:10 cycles, with a sequencing depth of 20,000 reads per cell for cDNA and 5,000 reads per cell for hashtag libraries.

853

854 **Single-cell RNA sequencing analysis**

855 Demultiplexing, alignment to the mouse genome (GRCm38/mm10), filtering, unique
856 molecular identifier counting and construction of gene-barcode matrices of the single-cell
857 RNA-Seq data were performed using Cell Ranger (7.1.0). Single-cell RNA-Seq data were further
858 analyzed using R Bioconductor (4.2.3) and the Seurat package (4.3.0). Filtered matrices
859 containing cell IDs and feature names for each sample were used to construct a Seurat object.
860 Datasets from both experiments were merged and integrated with previously published
861 single-cell RNA-seq data containing $CD45^{+}SSC^{lo}CD11b^{+}F4/80^{+}CD64^{+}$ lung IM cells of
862 $Lyz2^{Cre}Mafb^{fl/fl}$ mice and $Mafb^{fl/fl}$ littermate controls (GSE193891). Quality control was
863 performed by excluding cells with fewer than 200 detected genes, genes detected in fewer
864 than three cells, and cells with more than 10% mitochondrial gene content. Gene counts for
865 each sample were normalized using the default *LogNormalize* method, with a scale factor of
866 10,000 followed by log transformation. The top 2,000 highly variable features were identified
867 using the vst method. Contaminating and actively proliferating cells were removed based on
868 the expression of specific genes. Cells were clustered using the *FindClusters* function and the
869 macrophage subsets were identified based on the expression of Hashtag barcodes and known
870 macrophage subset specific genes. DEGs between macrophages subsets from $Mafb^{fl/fl}$ and
871 $Lyz2^{Cre}Mafb^{fl/fl}$ mice were determined using the *FindMarkers* method.

872

873 **Signature scoring**

874 For scRNA-seq, gene set signature scores were calculated using the *AddModuleScore* function
875 (Seurat). The scores were saved within a Seurat object and visualized using the Seurat

876 package. Differences in gene set signature scores between macrophages subsets from *Mafb*$^{fl/fl}$
877 and *Lyz2*^{Cre}*Mafb*$^{fl/fl}$ mice were determined using a Wilcoxon rank sum test.
878 Mac subset-specific signature scores were calculated using the scRNA-seq data of RTMs from
879 *Mafb*$^{fl/fl}$ mice by comparing each RTM subset to all other subsets in the dataset using the
880 *FindAllMarker* function (Seurat).
881 EMP, preMac and Mac signature genes have been previously described.[45]
882
883 **Confocal microscopy**
884 Confocal microscopy was performed as described previously.[71] Immediately after euthanizing
885 mice with CO_2, the inferior vena cava was cannulated, and the liver was perfused with
886 Antigenfix (Diapath, P0014) at 5 ml/min for 5 min at room temperature. Liver slices (2–3 mm)
887 were then fixed by immersion in Antigenfix for 1 h at 4 °C, washed in PBS, cryoprotected
888 overnight in 34% sucrose, and embedded in Tissue-Tek OCT compound (Sakura Finetek).
889 Cryosections (20 µm) were cut using a Microm HM 560 cryostat (Thermo Fisher Scientific),
890 rehydrated in PBS for 5 min, permeabilized with 0.5% saponin (Sigma-Aldrich, 4521), and
891 blocked for 30 min with 2% bovine serum albumin, 1% fetal calf serum, and 1% donkey serum
892 (Abcam, ab7475). Sections were incubated overnight at 4 °C with primary antibodies, followed
893 by incubation with DAPI (Thermo Fisher Scientific, D3571) and secondary antibodies for 1 h at
894 room temperature. Slides were mounted with ProLong Diamond (Thermo Fisher Scientific,
895 P36970), imaged on a Zeiss LSM980 confocal microscope equipped with a spectral detector
896 using spectral unmixing. For image analysis, Z-stacks were converted to single-plane, per-
897 channel images by mean projection along the Z axis. The projected 2D images were imported
898 into QuPath (0.5.1), where a pixel classifier was first trained and then applied to all images
899 and class-specific binary masks were exported. Each mask was cleaned in scikit-image (0.20.0)

using binary opening (disk radius = 2 px), filling of small holes (< 64 px), and removal of very small objects (< 100 px). Masks were resized with nearest-neighbor interpolation to match the measurement-image resolution and converted to labeled objects via connected components (skimage.measure.label; connectivity = 2). A final size filter retained objects with area ≥ 1,500 px for analysis. For each labeled object (cell), solidity and Tim4 expression were quantified using scikit-image (skimage.measure; regionprops/regionprops_table): solidity was defined as the ratio of the object area to the area of its convex hull, and Tim4 expression was measured as the mean intensity of the Tim4 channel within the object mask.

In vivo phagocytosis assay

pHrodo™ Red S. aureus Bioparticles (Thermo Fisher Scientific, A10010) were prepared in PBS according to the manufacturer's instructions. *Mafb*$^{fl/fl}$ or *Lyz2*^{Cre}*Mafb*$^{fl/fl}$ mice received 50 µg Bioparticles either intraperitoneally (i.p.) to assess uptake by LPMs or intravenously (i.v.) to assess uptake by KCs. Mice were sacrificed 20 min (i.p.) or 30 min (i.v.) post-injection, followed by collection of peritoneal lavage or dissection of the liver, respectively. As a negative control, one mouse was sacrificed immediately after injection. Bioparticle uptake by LPMs and KCs was analyzed by FACS.

In vivo erythrophagocytosis assay

C57BL/6J wild-type mice were terminally anesthetized and perfused via the left ventricle with 20 ml PBS containing 10 mM EDTA. Perfusate was collected via a small incision in the right atrium using fine scissors, and cells were pelleted by centrifugation at 800 × g for 10 min. $CD45^+$ immune cells were depleted using MACS with CD45 MicroBeads (Miltenyi Biotec,

130052301), the flowthrough containing red blood cells (RBCs) was recovered and centrifuged at 800 × g for 10 min.

Senescent RBCs (sRBCs) were generated by mild heat treatment for 20 min at 48 °C under continuous agitation. For labeling, a total of 1×10^{10} sRBCs were resuspended in 1 ml Diluent C and incubated with an equal volume of Diluent C containing 4 µM PKH26 (Sigma-Aldrich, MIDI26) for 5 min at room temperature in the dark. The reaction was quenched with 10 ml PBS supplemented with 0.5% BSA and 2% FCS, followed by two washes with PBS. PKH26-labeled sRBCs were resuspended in PBS at a final concentration of 1×10^{10} cells/ml.

For the erythrophagocytosis assay, *Mafb*$^{fl/fl}$ or *Lyz2*^{Cre}*Mafb*$^{fl/fl}$ mice were injected i.v. with 1×10^9 PKH26-labeled sRBCs. After 30 min, mice were sacrificed, spleens were harvested, and RPM uptake of PKH26-sRBCs was analyzed by flow cytometry.

Iron stain

Spleens from *Mafb*$^{fl/fl}$ or *Lyz2*^{Cre}*Mafb*$^{fl/fl}$ mice were dissected, weighed, fixed overnight in 4% formaldehyde (Fisher, BP531500) in PBS, paraffin-embedded, cut into 5-µm sections, stained with Perl's Prussian blue solution and counterstained with Nuclear Fast Red. Images were acquired on a Axioscan 7 (Zeiss) and analyzed by QuPath (0.5.1).

Lung function measurements

Mice were anesthetized via i.p. administration of 50 mg/kg sodium pentobarbital (Nembutal). Following a midline incision in the neck, the trachea was exposed and intubated with an 18-gauge blunt metal cannula with a resistance of 0.18 $cmH_2O{\cdot}s/ml$. The cannula was secured in place using nylon suture and connected to a computer-controlled small animal ventilator (flexiVent, SCIREQ) through FX adaptor Y-tubing. Ventilator settings were adjusted to standard

murine parameters: tidal volume of 10 ml/kg, respiratory rate of 150 breaths/min, positive end-expiratory pressure (PEEP) of 3 cmH_2O, and a fraction of inspired oxygen (FiO_2) of 0.21 (room air). Respiratory system mechanics were then quantified using the forced oscillation technique (FOT) with flexiWare software (8.1.3).

Whole gut transit time assay

Whole-gut transit time was measured using carmine red gavage. After an overnight fast, *Mafb*$^{fl/fl}$ or *Lyz2*^{Cre}*Mafb*$^{fl/fl}$ mice were orally gavaged with a 6% (w/v) solution of carmine red (Sigma-Aldrich, C1022) prepared in sterile 0.5% methyl cellulose (Sigma-Aldrich, 423181) and subsequently single-housed. Animals were observed at 15-minute intervals, and the time from gavage to the appearance of the first red-colored fecal pellet was recorded as the total whole-gut transit time.

Kidney stone model

Mafb$^{fl/fl}$ or *Lyz2*^{Cre}*Mafb*$^{fl/fl}$ mice were injected i.p. with sodium oxalate (NaOx, Sigma-Aldrich, 223433) at 40 mg/kg daily for 7 days. Twenty-four hours after the final injection, mice were sacrificed and perfused with cold PBS followed by 4% formaldehyde in PBS. Kidneys were dissected fixed overnight in 4% formaldehyde, paraffin-embedded, sectioned at 5 µm, and stained with 0.2% Alizarin Red S (pH 6.8) for 10 min at 37 °C. Images were acquired on a Axioscan 7 (Zeiss) and analyzed by QuPath (0.5.1).

Human monocyte-derived macrophages differentiation

Buffy coats from healthy volunteers were obtained through the Belgian Red Cross. Peripheral blood mononuclear cells were isolated by density gradient centrifugation on Lymphoprep

(1.077 g/ml; StemCell Technologies). Classical monocytes were negatively selected using the Classical Monocyte Isolation Kit (Miltenyi Biotec, 130117337) according to the manufacturer's instructions. Monocytes were seeded in Petri dishes (10×10^6 cells/dish) in RPMI supplemented with 10% FBS, 1× MEM NEAA (Thermo Fisher Scientific, 11140050), 50 µM β-mercaptoethanol, and 50 ng/ml recombinant human CSF-1 (Immunotools, 11343115). Fresh differentiation medium was added on day 3. On day 7, monocyte-derived macrophages (MDMs) were detached using cold PBS containing 0.25 mM EDTA.

CUT&RUN library preparation

CUT&RUN was performed using the CUTANA ChIC/CUT&RUN Kit (EpiCypher, 141048) according to the manufacturer's instructions, with minor modifications. BMDMs or LPMs from *Mafb*$^{fl/fl}$ or *Lyz2*^{Cre}*Mafb*$^{fl/fl}$ mice, as well as human MDMs from healthy donors, were washed with ice-cold PBS and fixed with 0.1% formaldehyde in PBS for 2 min at room temperature. Fixation was quenched with 0.125 M glycine (Merck, 104691000). For each CUT&RUN sample, 0.5×10^6 fixed cells were incubated with 0.5 µg antibody. The following antibodies were used: anti-MafB (Cell Signaling Technology, 41019), anti-H3K27ac (Thermo Fisher Scientific, MA5-23516), and IgG negative control (EpiCypher, 13-0042). CUT&RUN libraries were prepared using the CUTANA CUT&RUN Library Prep Kit (EpiCypher, 141001) following the manufacturer's instructions and sequenced on a NovaSeq 6000 (Illumina) with an S4 flow cell at a depth of 10 million reads per sample.

CUT&RUN analysis

Raw reads were processed using the *nf-core/cutandrun* pipeline for adapter trimming, alignment to the mouse reference genome (GRCm38/mm10), and quality control. For MafB

CUT&RUN, peaks were called using SEACR (Sparse Enrichment Analysis for CUT&RUN) in stringent mode.[72] Normalized tag counts were calculated with the *annotatePeaks.pl* function from HOMER. MafB binding sites were defined as peaks with higher normalized tag counts in wild-type compared with MafB-deficient cells. MafB binding sites were assigned to target genes based on proximity to transcription start sites (±2 kb) using HOMER. CUT&RUN signal tracks were visualized with the Integrative Genomics Viewer (IGV).

Evolutionary conservation scoring

Multiple alignments of 60 vertebrate species to the mouse genome (mm10) and measurements of evolutionary conservation based on the alignment (*phastCons* and *phyloP*) were retrieved from the UCSC Genome Browser. A phylogenetic tree from the multiple genome alignment was constructed using ETE Toolkit (3.1.3). Evolutionary conservation at MafB and PU.1 binding sites was quantified by calculating the mean *phastCons* and *phyloP* score around −500 to +500 bp from peak center. Global evolutionary conservation was quantified by subdividing the mouse genome in fragments of 1 kbp and calculating the mean *phastCons* and *phyloP* score of each fragment.

Analysis of published scRNA-seq data

To create a single-cell transcriptomic myeloid cell atlas, we selected myeloid cell clusters form the Tabula Muris Senis atlas[40], based on the combined expression of *Ptprc* (CD45) and *Lyz2*. Cells were reclustered using the *FindClusters* function from the Seurat package (4.3.0). Clusters of contaminating and actively proliferating cells were removed and myeloid cells clusters were identified based on the expression of specific genes. To infer TF activity, we ran a Univariate Linear Model using the decoupleR package (2.10.0).[41] Briefly, for each TF, a linear

model is fitted, which predicts the observed gene expression based TF -target gene interaction weights. The t-value of the slope from the fitted linear model is extracted as TF enrichment score. A TF with a positive score is interpreted as active, while a TF with a negative score is considered inactive.

To generate a single-cell transcriptomic map of macrophage differentiation, we selected clusters of mac and mac progenitors from recently published scRNA-seq data of FACS-sorted CD11b$^{low/+}$ fetal liver cells at embryonic day of development E14.5[46], based on the expression EMP, preMac and Mac signature genes (Table S2).[45] Cells were reclustered using the *FindClusters* function from the Seurat package (4.3.0). To evaluate trajectory-based pseudotime analysis, we used the Slingshot package (2.14.0) with EPM as starting cluster and mac as ending cluster.

To quantify the correlation between Mafb expression and the expression of mac signature genes or MafB target genes in single-cell atlases across different species, genes were converted into species-specific orthologs using g:Profiler. Mac signature genes or MafB target genes scores were calculated using the *AddModuleScore* function from the Seurat package. Correlation between Mafb expression and the expression of mac signature genes or MafB target genes was calculated using Pearson correlation.

QUANTIFICATION AND STATISTICAL ANALYSIS

Data was visualized with Prism 9 (GraphPad) and R Bioconductor (4.2.3) using packages *ggplot2* and *ComplexHeatmap*. Data are presented as mean ± SEM unless stated otherwise. Sample sizes were not pre-determined by statistical methods but are consistent with those used in previous publications.[37,73–75] Data were assumed to follow a normal distribution for parametric tests, though this was not formally tested. Results from independent experiments

were combined for analysis in each panel, unless otherwise specified, and no data were excluded. Investigators were not blinded during data collection and analysis. Statistical analyses were carried out using Prism 9 (GraphPad), and R Bioconductor (4.2.3) with DESeq2 (1.38.3) for bulk RNA-seq and Seurat (4.3.0) for scRNA-seq data. Detailed statistical methods for each experiment are provided in the figure legends. A *P*-value of less than 0.05 was considered statistically significant (*, $P < 0.05$; **, $P < 0.01$; ***, $P < 0.001$; ****, $P < 0.0001$; ns, not significant).

SUPPLEMENTAL INFORMATION

Document S1. Figures S1–S7.

Table S1. Differentially expressed genes between BMDM from *Lyz2^{Cre}Mafb$^{fl/fl}$* mice and *Mafb$^{fl/fl}$* littermate controls, related to Figure 2.

Table S2. Table S2. Gene signatures used for GSEA and signature scoring analyses, related to Figures 2 and 3.

Table S3. Differentially expressed genes between RTMs from *Lyz2^{Cre}Mafb$^{fl/fl}$* mice and *Mafb$^{fl/fl}$* littermate controls, related to Figure 3.

Table S4. MafB binding sites in BMDM, LPM and MDM, related to Figures 6 and 7.

Video S1. *Ex vivo* differentiation of BMMo from *Mafb$^{fl/fl}$* littermate control mice, related to Figure 2.

Video S2. *Ex vivo* differentiation of BMMo from *Lyz2^{Cre}Mafb$^{fl/fl}$* mice, related to Figure 2.

REFERENCES

1. Blériot, C., Chakarov, S., and Ginhoux, F. (2020). Determinants of Resident Tissue Macrophage Identity and Function. Immunity *52*, 957–970. https://doi.org/10.1016/j.immuni.2020.05.014.

2. Guilliams, M., Thierry, G.R., Bonnardel, J., and Bajenoff, M. (2020). Establishment and Maintenance of the Macrophage Niche. Immunity *52*, 434–451. https://doi.org/10.1016/j.immuni.2020.02.015.

3. Lavin, Y., Winter, D., Blecher-Gonen, R., David, E., Keren-Shaul, H., Merad, M., Jung, S., and Amit, I. (2014). Tissue-resident macrophage enhancer landscapes are shaped by the local microenvironment. Cell *159*, 1312–1326. https://doi.org/10.1016/j.cell.2014.11.018.

4. Lavin, Y., Mortha, A., Rahman, A., and Merad, M. (2015). Regulation of macrophage development and function in peripheral tissues. Nat Rev Immunol *15*, 731–744. https://doi.org/10.1038/nri3920.

5. Park, M.D., Silvin, A., Ginhoux, F., and Merad, M. (2022). Macrophages in health and disease. Cell *185*, 4259–4279. https://doi.org/10.1016/j.cell.2022.10.007.

6. Ginhoux, F., and Guilliams, M. (2016). Tissue-Resident Macrophage Ontogeny and Homeostasis. Immunity *44*, 439–449. https://doi.org/10.1016/j.immuni.2016.02.024.

7. Chakarov, S., Lim, H.Y., Tan, L., Lim, S.Y., See, P., Lum, J., Zhang, X.-M., Foo, S., Nakamizo, S., Duan, K., et al. (2019). Two distinct interstitial macrophage populations coexist across tissues in specific subtissular niches. Science *363*. https://doi.org/10.1126/science.aau0964.

8. Ginhoux, F., Greter, M., Leboeuf, M., Nandi, S., See, P., Gokhan, S., Mehler, M.F., Conway, S.J., Ng, L.G., Stanley, E.R., et al. (2010). Fate mapping analysis reveals that adult microglia derive from primitive macrophages. Science (New York, N.Y.) *330*, 841–845. https://doi.org/10.1126/science.1194637.

9. Gomez Perdiguero, E., Klapproth, K., Schulz, C., Busch, K., Azzoni, E., Crozet, L., Garner, H., Trouillet, C., de Bruijn, M.F., Geissmann, F., et al. (2015). Tissue-resident macrophages originate from yolk-sac-derived erythro-myeloid progenitors. Nature *518*, 547–551. https://doi.org/10.1038/nature13989.

10. Hashimoto, D., Chow, A., Noizat, C., Teo, P., Beasley, M.B., Leboeuf, M., Becker, C.D., See, P., Price, J., Lucas, D., et al. (2013). Tissue-resident macrophages self-maintain locally throughout adult life with minimal contribution from circulating monocytes. Immunity *38*, 792–804. https://doi.org/10.1016/j.immuni.2013.04.004.

11. Yona, S., Kim, K.-W., Wolf, Y., Mildner, A., Varol, D., Breker, M., Strauss-Ayali, D., Viukov, S., Guilliams, M., Misharin, A., et al. (2013). Fate mapping reveals origins and dynamics of monocytes and tissue macrophages under homeostasis. Immunity *38*, 79–91. https://doi.org/10.1016/j.immuni.2012.12.001.

12. Guilliams, M., and Svedberg, F.R. (2021). Does tissue imprinting restrict macrophage plasticity? Nat Immunol *22*, 118–127. https://doi.org/10.1038/s41590-020-00849-2.

13. Hume, D.A., Irvine, K.M., and Pridans, C. (2019). The Mononuclear Phagocyte System: The Relationship between Monocytes and Macrophages. Trends Immunol *40*, 98–112. https://doi.org/10.1016/j.it.2018.11.007.

14. Liu, Z., Gu, Y., Chakarov, S., Bleriot, C., Kwok, I., Chen, X., Shin, A., Huang, W., Dress, R.J., Dutertre, C.-A., et al. (2019). Fate Mapping via Ms4a3-Expression History Traces Monocyte-Derived Cells. Cell *178*, 1509-1525.e19. https://doi.org/10.1016/j.cell.2019.08.009.

15. Ginhoux, F., Schultze, J.L., Murray, P.J., Ochando, J., and Biswas, S.K. (2016). New insights into the multidimensional concept of macrophage ontogeny, activation and function. Nat Immunol *17*, 34–40. https://doi.org/10.1038/ni.3324.

16. Aegerter, H., Lambrecht, B.N., and Jakubzick, C.V. (2022). Biology of lung macrophages in health and disease. Immunity *55*, 1564–1580. https://doi.org/10.1016/j.immuni.2022.08.010.

17. Guilliams, M., and Scott, C.L. (2022). Liver macrophages in health and disease. Immunity *55*, 1515–1529. https://doi.org/10.1016/j.immuni.2022.08.002.

18. Vanneste, D., and Marichal, T. (2025). Transcriptional Regulation of Macrophage Specification and Function. Eur J Immunol *55*, e70097. https://doi.org/10.1002/eji.70097.

19. Hume, D.A., Pavli, P., Donahue, R.E., and Fidler, I.J. (1988). The effect of human recombinant macrophage colony-stimulating factor (CSF-1) on the murine mononuclear phagocyte system in vivo. J Immunol *141*, 3405–3409.

20. Tagliani, E., Shi, C., Nancy, P., Tay, C.-S., Pamer, E.G., and Erlebacher, A. (2011). Coordinate regulation of tissue macrophage and dendritic cell population dynamics by CSF-1. J Exp Med *208*, 1901–1916. https://doi.org/10.1084/jem.20110866.

21. Allen, J.M., and Seed, B. (1989). Isolation and Expression of Functional High-Affinity Fc Receptor Complementary DNAs. Science *243*, 378–381. https://doi.org/10.1126/science.2911749.

22. Gautier, E.L., Shay, T., Miller, J., Greter, M., Jakubzick, C., Ivanov, S., Helft, J., Chow, A., Elpek, K.G., Gordonov, S., et al. (2012). Gene-expression profiles and transcriptional regulatory pathways that underlie the identity and diversity of mouse tissue macrophages. Nature immunology *13*, 1118–1128. https://doi.org/10.1038/ni.2419.

23. Scott, E.W., Simon, M.C., Anastasi, J., and Singh, H. (1994). Requirement of transcription factor PU.1 in the development of multiple hematopoietic lineages. Science *265*, 1573–1577. https://doi.org/10.1126/science.8079170.

24. Molawi, K., and Sieweke, M.H. (2013). Transcriptional control of macrophage identity, self-renewal, and function. Adv Immunol *120*, 269–300. https://doi.org/10.1016/B978-0-12-417028-5.00010-7.

25. Scott, C.L., T'Jonck, W., Martens, L., Todorov, H., Sichien, D., Soen, B., Bonnardel, J., De Prijck, S., Vandamme, N., Cannoodt, R., et al. (2018). The Transcription Factor ZEB2 Is Required to Maintain the Tissue-Specific Identities of Macrophages. Immunity *49*, 312-325.e5. https://doi.org/10.1016/j.immuni.2018.07.004.

26. Kataoka, K., Fujiwara, K.T., Noda, M., and Nishizawa, M. (1994). MafB, a new Maf family transcription activator that can associate with Maf and Fos but not with Jun. Mol Cell Biol *14*, 7581–7591. https://doi.org/10.1128/mcb.14.11.7581-7591.1994.

27. Sieweke, M.H., Tekotte, H., Frampton, J., and Graf, T. (1996). MafB is an interaction partner and repressor of Ets-1 that inhibits erythroid differentiation. Cell *85*, 49–60. https://doi.org/10.1016/s0092-8674(00)81081-8.

28. Kelly, L.M., Englmeier, U., Lafon, I., Sieweke, M.H., and Graf, T. (2000). MafB is an inducer of monocytic differentiation. EMBO J *19*, 1987–1997. https://doi.org/10.1093/emboj/19.9.1987.

29. Hamada, M. (2003). The Mouse mafB 5'-Upstream Fragment Directs Gene Expression in Myelomonocytic Cells, Differentiated Macrophages and the Ventral Spinal Cord in Transgenic Mice. Journal of Biochemistry *134*, 203–210. https://doi.org/10.1093/jb/mvg130.

30. Moriguchi, T., Hamada, M., Morito, N., Terunuma, T., Hasegawa, K., Zhang, C., Yokomizo, T., Esaki, R., Kuroda, E., Yoh, K., et al. (2006). MafB Is Essential for Renal Development and F4/80 Expression in Macrophages. Mol Cell Biol *26*, 5715–5727. https://doi.org/10.1128/MCB.00001-06.

31. Wu, X., Briseño, C.G., Durai, V., Albring, J.C., Haldar, M., Bagadia, P., Kim, K.-W., Randolph, G.J., Murphy, T.L., and Murphy, K.M. (2016). Mafb lineage tracing to distinguish macrophages from other immune lineages reveals dual identity of Langerhans cells. J Exp Med *213*, 2553–2565. https://doi.org/10.1084/jem.20160600.

32. Aziz, A., Vanhille, L., Mohideen, P., Kelly, L.M., Otto, C., Bakri, Y., Mossadegh, N., Sarrazin, S., and Sieweke, M.H. (2006). Development of macrophages with altered actin organization in the absence of MafB. Mol Cell Biol *26*, 6808–6818. https://doi.org/10.1128/MCB.00245-06.

33. Aziz, A., Soucie, E., Sarrazin, S., and Sieweke, M.H. (2009). MafB/c-Maf deficiency enables self-renewal of differentiated functional macrophages. Science *326*, 867–871. https://doi.org/10.1126/science.1176056.

34. Tran, M.T.N., Hamada, M., Jeon, H., Shiraishi, R., Asano, K., Hattori, M., Nakamura, M., Imamura, Y., Tsunakawa, Y., Fujii, R., et al. (2017). MafB is a critical regulator of complement component C1q. Nat Commun *8*, 1700. https://doi.org/10.1038/s41467-017-01711-0.

35. Matcovitch-Natan, O., Winter, D.R., Giladi, A., Vargas Aguilar, S., Spinrad, A., Sarrazin, S., Ben-Yehuda, H., David, E., Zelada González, F., Perrin, P., et al. (2016). Microglia development follows a stepwise program to regulate brain homeostasis. Science *353*, aad8670. https://doi.org/10.1126/science.aad8670.

36. Yadav, M.K., Ishida, M., Gogoleva, N., Liao, C.-W., Salim, F.N., Kanai, M., Kuno, A., Hayashi, T., Shahri, Z.J., Kulathunga, K., et al. (2024). MAFB in macrophages regulates cold-induced neuronal density in brown adipose tissue. Cell Rep *43*, 113978. https://doi.org/10.1016/j.celrep.2024.113978.

37. Vanneste, D., Bai, Q., Hasan, S., Peng, W., Pirottin, D., Schyns, J., Maréchal, P., Ruscitti, C., Meunier, M., Liu, Z., et al. (2023). MafB-restricted local monocyte proliferation precedes lung interstitial macrophage differentiation. Nat Immunol *24*, 827–840. https://doi.org/10.1038/s41590-023-01468-3.

38. Heng, T.S.P., Painter, M.W., and Immunological Genome Project Consortium (2008). The Immunological Genome Project: networks of gene expression in immune cells. Nat Immunol *9*, 1091–1094. https://doi.org/10.1038/ni1008-1091.

39. Soucie, E.L., Weng, Z., Geirsdottir, L., Molawi, K., Maurizio, J., Fenouil, R., Mossadegh-Keller, N., Gimenez, G., VanHille, L., Beniazza, M., et al. (2016). Lineage-specific enhancers activate self-renewal genes in macrophages and embryonic stem cells. Science *351*, aad5510. https://doi.org/10.1126/science.aad5510.

40. Tabula Muris Consortium (2020). A single-cell transcriptomic atlas characterizes ageing tissues in the mouse. Nature *583*, 590–595. https://doi.org/10.1038/s41586-020-2496-1.

41. Badia-I-Mompel, P., Vélez Santiago, J., Braunger, J., Geiss, C., Dimitrov, D., Müller-Dott, S., Taus, P., Dugourd, A., Holland, C.H., Ramirez Flores, R.O., et al. (2022). decoupleR: ensemble of computational methods to infer biological activities from omics data. Bioinform Adv *2*, vbac016. https://doi.org/10.1093/bioadv/vbac016.

42. Tamoutounour, S., Henri, S., Lelouard, H., de Bovis, B., de Haar, C., van der Woude, C.J., Woltman, A.M., Reyal, Y., Bonnet, D., Sichien, D., et al. (2012). CD64 distinguishes macrophages from dendritic cells in the gut and reveals the Th1-inducing role of mesenteric lymph node macrophages during colitis. European journal of immunology *42*, 3150–3166. https://doi.org/10.1002/eji.201242847.

43. Bain, C.C., Hawley, C.A., Garner, H., Scott, C.L., Schridde, A., Steers, N.J., Mack, M., Joshi, A., Guilliams, M., Mowat, A.M.I., et al. (2016). Long-lived self-renewing bone marrow-derived macrophages displace embryo-derived cells to inhabit adult serous cavities. Nat Commun *7*, ncomms11852. https://doi.org/10.1038/ncomms11852.

44. Schridde, A., Bain, C.C., Mayer, J.U., Montgomery, J., Pollet, E., Denecke, B., Milling, S.W.F., Jenkins, S.J., Dalod, M., Henri, S., et al. (2017). Tissue-specific differentiation of colonic macrophages requires TGFβ receptor-mediated signaling. Mucosal Immunol *10*, 1387–1399. https://doi.org/10.1038/mi.2016.142.

45. Mass, E., Ballesteros, I., Farlik, M., Halbritter, F., Günther, P., Crozet, L., Jacome-Galarza, C.E., Händler, K., Klughammer, J., Kobayashi, Y., et al. (2016). Specification of tissue-resident macrophages during organogenesis. Science *353*, aaf4238. https://doi.org/10.1126/science.aaf4238.

46. Kayvanjoo, A.H., Splichalova, I., Bejarano, D.A., Huang, H., Mauel, K., Makdissi, N., Heider, D., Tew, H.M., Balzer, N.R., Greto, E., et al. (2024). Fetal liver macrophages contribute to the hematopoietic stem cell niche by controlling granulopoiesis. Elife *13*, e86493. https://doi.org/10.7554/eLife.86493.

47. Trzebanski, S., Kim, J.-S., Larossi, N., Raanan, A., Kancheva, D., Bastos, J., Haddad, M., Solomon, A., Sivan, E., Aizik, D., et al. (2024). Classical monocyte ontogeny dictates their functions and fates as tissue macrophages. Immunity *57*, 1225-1242.e6. https://doi.org/10.1016/j.immuni.2024.04.019.

48. Prise, I.E., Jayaraman, V., Kästele, V., Daw, R.H., Wemyss, K., Bridgeman, H., Tamburrano, S., Strangward, P., Chew, C., Martens, L., et al. (2023). CD163 and Tim-4 identify resident intestinal macrophages across sub-tissular regions that are spatially regulated by TGF-β. Preprint, https://doi.org/10.1101/2023.08.21.553672 https://doi.org/10.1101/2023.08.21.553672.

49. Kohyama, M., Ise, W., Edelson, B.T., Wilker, P.R., Hildner, K., Mejia, C., Frazier, W.A., Murphy, T.L., and Murphy, K.M. (2009). Role for Spi-C in the development of red pulp macrophages and splenic iron homeostasis. Nature *457*, 318–321. https://doi.org/10.1038/nature07472.

50. Peng, W., Vanneste, D., Bejarano, D., Abinet, J., Meunier, M., Radermecker, C., Perin, F., Cataldo, D., Bureau, F., Schlitzer, A., et al. (2025). Endothelial-driven TGFβ signaling supports lung interstitial macrophage development from monocytes. Sci Immunol *10*, eadr4977. https://doi.org/10.1126/sciimmunol.adr4977.

51. Viola, M.F., Chavero-Pieres, M., Modave, E., Delfini, M., Stakenborg, N., Estévez, M.C., Fabre, N., Appeltans, I., Martens, T., Vandereyken, K., et al. (2023). Dedicated macrophages organize and maintain the enteric nervous system. Nature *618*, 818–826. https://doi.org/10.1038/s41586-023-06200-7.

52. He, J., Cao, Y., Zhu, Q., Wang, X., Cheng, G., Wang, Q., He, R., Lu, H., Weng, Y., Mao, G., et al. (2024). Renal macrophages monitor and remove particles from urine to prevent tubule obstruction. Immunity *57*, 106-123.e7. https://doi.org/10.1016/j.immuni.2023.12.003.

53. Scott, C.L., T'Jonck, W., Martens, L., Todorov, H., Sichien, D., Soen, B., Bonnardel, J., De Prijck, S., Vandamme, N., Cannoodt, R., et al. (2018). The Transcription Factor ZEB2 Is Required to Maintain the Tissue-Specific Identities of Macrophages. Immunity *49*, 312-325 e5. https://doi.org/10.1016/j.immuni.2018.07.004.

54. Moura Silva, H., Kitoko, J.Z., Queiroz, C.P., Kroehling, L., Matheis, F., Yang, K.L., Reis, B.S., Ren-Fielding, C., Littman, D.R., Bozza, M.T., et al. (2021). c-MAF-dependent perivascular macrophages regulate diet-induced metabolic syndrome. Sci Immunol *6*, eabg7506. https://doi.org/10.1126/sciimmunol.abg7506.

55. Nakamura, M., Hamada, M., Hasegawa, K., Kusakabe, M., Suzuki, H., Greaves, D.R., Moriguchi, T., Kudo, T., and Takahashi, S. (2009). c-Maf is essential for the F4/80 expression in macrophages in vivo. Gene *445*, 66–72. https://doi.org/10.1016/j.gene.2009.06.003.

56. Dai, X.-M., Ryan, G.R., Hapel, A.J., Dominguez, M.G., Russell, R.G., Kapp, S., Sylvestre, V., and Stanley, E.R. (2002). Targeted disruption of the mouse colony-stimulating factor 1 receptor gene results in osteopetrosis, mononuclear phagocyte deficiency, increased primitive progenitor cell frequencies, and reproductive defects. Blood *99*, 111–120. https://doi.org/10.1182/blood.v99.1.111.

57. Pridans, C., Raper, A., Davis, G.M., Alves, J., Sauter, K.A., Lefevre, L., Regan, T., Meek, S., Sutherland, L., Thomson, A.J., et al. (2018). Pleiotropic Impacts of Macrophage and Microglial Deficiency on Development in Rats with Targeted Mutation of the Csf1r Locus. J Immunol *201*, 2683–2699. https://doi.org/10.4049/jimmunol.1701783.

58. Rojo, R., Raper, A., Ozdemir, D.D., Lefevre, L., Grabert, K., Wollscheid-Lengeling, E., Bradford, B., Caruso, M., Gazova, I., Sánchez, A., et al. (2019). Deletion of a Csf1r enhancer selectively impacts CSF1R expression and development of tissue macrophage populations. Nat Commun *10*, 3215. https://doi.org/10.1038/s41467-019-11053-8.

59. Hume, D.A., Wollscheid-Lengeling, E., Rojo, R., and Pridans, C. (2017). The evolution of the macrophage-specific enhancer (Fms intronic regulatory element) within the CSF1R locus of vertebrates. Sci Rep *7*, 17115. https://doi.org/10.1038/s41598-017-15999-x.

60. Sasmono, R.T., Oceandy, D., Pollard, J.W., Tong, W., Pavli, P., Wainwright, B.J., Ostrowski, M.C., Himes, S.R., and Hume, D.A. (2003). A macrophage colony-stimulating factor receptor-green fluorescent protein transgene is expressed throughout the mononuclear phagocyte system of the mouse. Blood *101*, 1155–1163. https://doi.org/10.1182/blood-2002-02-0569.

61. Pridans, C., Lillico, S., Whitelaw, B., and Hume, D.A. (2014). Lentiviral vectors containing mouse Csf1r control elements direct macrophage-restricted expression in multiple species of birds and mammals. Mol Ther Methods Clin Dev *1*, 14010. https://doi.org/10.1038/mtm.2014.10.

62. Hecker, N., Kempynck, N., Mauduit, D., Abaffyová, D., Vandepoel, R., Dieltiens, S., Sarropoulos, I., González-Blas, C.B., Leysen, E., Moors, R., et al. (2024). Enhancer-driven cell type comparison reveals similarities between the mammalian and bird pallium. bioRxiv, 2024.04.17.589795. https://doi.org/10.1101/2024.04.17.589795.

63. Cuevas, V.D., Anta, L., Samaniego, R., Orta-Zavalza, E., Vladimir de la Rosa, J., Baujat, G., Domínguez-Soto, Á., Sánchez-Mateos, P., Escribese, M.M., Castrillo, A., et al. (2017). MAFB Determines Human Macrophage Anti-Inflammatory Polarization: Relevance for the Pathogenic Mechanisms Operating in Multicentric Carpotarsal Osteolysis. J Immunol *198*, 2070–2081. https://doi.org/10.4049/jimmunol.1601667.

64. Goudot, C., Coillard, A., Villani, A.-C., Gueguen, P., Cros, A., Sarkizova, S., Tang-Huau, T.-L., Bohec, M., Baulande, S., Hacohen, N., et al. (2017). Aryl Hydrocarbon Receptor Controls Monocyte Differentiation into Dendritic Cells versus Macrophages. Immunity *47*, 582-596.e6. https://doi.org/10.1016/j.immuni.2017.08.016.

65. Wende, H., Lechner, S.G., Cheret, C., Bourane, S., Kolanczyk, M.E., Pattyn, A., Reuter, K., Munier, F.L., Carroll, P., Lewin, G.R., et al. (2012). The transcription factor c-Maf controls touch receptor development and function. Science *335*, 1373–1376. https://doi.org/10.1126/science.1214314.

66. Clausen, B.E., Burkhardt, C., Reith, W., Renkawitz, R., and Forster, I. (1999). Conditional gene targeting in macrophages and granulocytes using LysMcre mice. Transgenic research *8*, 265–277.

67. Kaiser, T., and Feng, G. (2019). Tmem119-EGFP and Tmem119-CreERT2 Transgenic Mice for Labeling and Manipulating Microglia. eNeuro *6*, ENEURO.0448-18.2019. https://doi.org/10.1523/ENEURO.0448-18.2019.

68. Bendall, S.C., Davis, K.L., Amir, E.-A.D., Tadmor, M.D., Simonds, E.F., Chen, T.J., Shenfeld, D.K., Nolan, G.P., and Pe'er, D. (2014). Single-cell trajectory detection

uncovers progression and regulatory coordination in human B cell development. Cell *157*, 714–725. https://doi.org/10.1016/j.cell.2014.04.005.

69. Love, M.I., Huber, W., and Anders, S. (2014). Moderated estimation of fold change and dispersion for RNA-seq data with DESeq2. Genome Biol *15*, 550. https://doi.org/10.1186/s13059-014-0550-8.

70. Gu, Z. (2023). simona: a Comprehensive R package for Semantic Similarity Analysis on Bio-Ontologies. bioRxiv, 2023.12.03.569758. https://doi.org/10.1101/2023.12.03.569758.

71. Bonnardel, J., T'Jonck, W., Gaublomme, D., Browaeys, R., Scott, C.L., Martens, L., Vanneste, B., De Prijck, S., Nedospasov, S.A., Kremer, A., et al. (2019). Stellate Cells, Hepatocytes, and Endothelial Cells Imprint the Kupffer Cell Identity on Monocytes Colonizing the Liver Macrophage Niche. Immunity *51*, 638-654.e9. https://doi.org/10.1016/j.immuni.2019.08.017.

72. Meers, M.P., Tenenbaum, D., and Henikoff, S. (2019). Peak calling by Sparse Enrichment Analysis for CUT&RUN chromatin profiling. Epigenetics Chromatin *12*, 42. https://doi.org/10.1186/s13072-019-0287-4.

73. Schyns, J., Bai, Q., Ruscitti, C., Radermecker, C., De Schepper, S., Chakarov, S., Farnir, F., Pirottin, D., Ginhoux, F., Boeckxstaens, G., et al. (2019). Non-classical tissue monocytes and two functionally distinct populations of interstitial macrophages populate the mouse lung. Nat Commun *10*, 3964. https://doi.org/10.1038/s41467-019-11843-0.

74. Radermecker, C., Sabatel, C., Vanwinge, C., Ruscitti, C., Maréchal, P., Perin, F., Schyns, J., Rocks, N., Toussaint, M., Cataldo, D., et al. (2019). Locally instructed CXCR4hi neutrophils trigger environment-driven allergic asthma through the release of neutrophil extracellular traps. Nat. Immunol. *20*, 1444–1455. https://doi.org/10.1038/s41590-019-0496-9.

75. Ruscitti, C., Abinet, J., Maréchal, P., Meunier, M., de Meeûs, C., Vanneste, D., Janssen, P., Dourcy, M., Thiry, M., Bureau, F., et al. (2024). Recruited atypical Ly6G+ macrophages license alveolar regeneration after lung injury. Sci Immunol *9*, eado1227. https://doi.org/10.1126/sciimmunol.ado1227.

76. Butovsky, O., Jedrychowski, M.P., Moore, C.S., Cialic, R., Lanser, A.J., Gabriely, G., Koeglsperger, T., Dake, B., Wu, P.M., Doykan, C.E., et al. (2014). Identification of a unique TGF-β-dependent molecular and functional signature in microglia. Nat Neurosci *17*, 131–143. https://doi.org/10.1038/nn.3599.

77. Tabula Sapiens Consortium*, Jones, R.C., Karkanias, J., Krasnow, M.A., Pisco, A.O., Quake, S.R., Salzman, J., Yosef, N., Bulthaup, B., Brown, P., et al. (2022). The Tabula Sapiens: A multiple-organ, single-cell transcriptomic atlas of humans. Science *376*, eabl4896. https://doi.org/10.1126/science.abl4896.

78. The Tabula Microcebus Consortium, Ezran, C., Liu, S., Chang, S., Ming, J., Botvinnik, O., Penland, L., Tarashansky, A., de Morree, A., Travaglini, K.J., et al. (2024). Tabula Microcebus: A transcriptomic cell atlas of mouse lemur, an emerging primate model organism. bioRxiv, 2021.12.12.469460. https://doi.org/10.1101/2021.12.12.469460.

79. Wang, F., Ding, P., Liang, X., Ding, X., Brandt, C.B., Sjöstedt, E., Zhu, J., Bolund, S., Zhang, L., de Rooij, L.P.M.H., et al. (2022). Endothelial cell heterogeneity and microglia regulons revealed by a pig cell landscape at single-cell level. Nat Commun *13*, 3620. https://doi.org/10.1038/s41467-022-31388-z.

80. Liao, Y., Ma, L., Guo, Q., E, W., Fang, X., Yang, L., Ruan, F., Wang, J., Zhang, P., Sun, Z., et al. (2022). Cell landscape of larval and adult Xenopus laevis at single-cell resolution. Nat Commun *13*, 4306. https://doi.org/10.1038/s41467-022-31949-2.

81. Wang, R., Zhang, P., Wang, J., Ma, L., E, W., Suo, S., Jiang, M., Li, J., Chen, H., Sun, H., et al. (2023). Construction of a cross-species cell landscape at single-cell level. Nucleic Acids Res *51*, 501–516. https://doi.org/10.1093/nar/gkac633.

82. Huerta-Cepas, J., Serra, F., and Bork, P. (2016). ETE 3: Reconstruction, Analysis, and Visualization of Phylogenomic Data. Mol Biol Evol *33*, 1635–1638. https://doi.org/10.1093/molbev/msw046.

83. Schindelin, J., Arganda-Carreras, I., Frise, E., Kaynig, V., Longair, M., Pietzsch, T., Preibisch, S., Rueden, C., Saalfeld, S., Schmid, B., et al. (2012). Fiji: an open-source platform for biological-image analysis. Nat. Methods *9*, 676–682. https://doi.org/10.1038/nmeth.2019.

84. Subramanian, A., Tamayo, P., Mootha, V.K., Mukherjee, S., Ebert, B.L., Gillette, M.A., Paulovich, A., Pomeroy, S.L., Golub, T.R., Lander, E.S., et al. (2005). Gene set enrichment analysis: a knowledge-based approach for interpreting genome-wide expression profiles. Proc Natl Acad Sci U S A *102*, 15545–15550. https://doi.org/10.1073/pnas.0506580102.

85. Kolberg, L., Raudvere, U., Kuzmin, I., Adler, P., Vilo, J., and Peterson, H. (2023). g:Profiler-interoperable web service for functional enrichment analysis and gene identifier mapping (2023 update). Nucleic Acids Res *51*, W207–W212. https://doi.org/10.1093/nar/gkad347.

86. Heinz, S., Benner, C., Spann, N., Bertolino, E., Lin, Y.C., Laslo, P., Cheng, J.X., Murre, C., Singh, H., and Glass, C.K. (2010). Simple combinations of lineage-determining transcription factors prime cis-regulatory elements required for macrophage and B cell identities. Mol Cell *38*, 576–589. https://doi.org/10.1016/j.molcel.2010.05.004.

87. Robinson, J.T., Thorvaldsdóttir, H., Winckler, W., Guttman, M., Lander, E.S., Getz, G., and Mesirov, J.P. (2011). Integrative genomics viewer. Nat Biotechnol *29*, 24–26. https://doi.org/10.1038/nbt.1754.

88. Ewels, P.A., Peltzer, A., Fillinger, S., Patel, H., Alneberg, J., Wilm, A., Garcia, M.U., Di Tommaso, P., and Nahnsen, S. (2020). The nf-core framework for community-curated bioinformatics pipelines. Nat Biotechnol *38*, 276–278. https://doi.org/10.1038/s41587-020-0439-x.

89. Bankhead, P., Loughrey, M.B., Fernández, J.A., Dombrowski, Y., McArt, D.G., Dunne, P.D., McQuaid, S., Gray, R.T., Murray, L.J., Coleman, H.G., et al. (2017). QuPath: Open source software for digital pathology image analysis. Sci Rep *7*, 16878. https://doi.org/10.1038/s41598-017-17204-5.

90. van der Walt, S., Schönberger, J.L., Nunez-Iglesias, J., Boulogne, F., Warner, J.D., Yager, N., Gouillart, E., Yu, T., and scikit-image contributors (2014). scikit-image: image processing in Python. PeerJ *2*, e453. https://doi.org/10.7717/peerj.453.

91. Perez, G., Barber, G.P., Benet-Pages, A., Casper, J., Clawson, H., Diekhans, M., Fischer, C., Gonzalez, J.N., Hinrichs, A.S., Lee, C.M., et al. (2024). The UCSC Genome Browser database: 2025 update. Nucleic Acids Res, gkae974. https://doi.org/10.1093/nar/gkae974.

1 **KEY RESOURCES TABLE**

REAGENT or RESOURCE	SOURCE	IDENTIFIER
Antibodies		
Anti-mouse C1qA Monoclonal Antibody (Mouse, clone JL-1), biotin conjugated	Novus	Cat#NBP1-51140B; RRID: AB_11014205
Anti-mouse CD3e Monoclonal Antibody (Armenian Hamster, clone 145-2C11), PE conjugated	BD Biosciences	Cat#553064; RRID: AB_394597
Anti-mouse CD11b Monoclonal Antibody (Rat, clone M1/70), BUV395 conjugated	BD Biosciences	Cat#563553; RRID: AB_2738276
Anti-mouse CD11b Monoclonal Antibody (Rat, clone M1/70), FITC conjugated	BD Biosciences	Cat#557396; RRID: AB_396679
Anti-mouse CD11b Monoclonal Antibody (Rat, clone M1/70), BV605 conjugated	BD Biosciences	Cat#563015; RRID: AB_2737951
Anti-mouse CD11b Monoclonal Antibody (Rat, clone M1/70), PE-Cy7 conjugated	BD Biosciences	Cat#552850; RRID: AB_394491
Anti-mouse CD11c Monoclonal Antibody (Armenian Hamster, clone N418), eFluor 450 conjugated	Thermo Fisher Scientific	Cat#48-0114-82; RRID: AB_1548654
Anti-mouse CD11c Monoclonal Antibody (Hamster, clone HL3), BV786 conjugated	BD Biosciences	Cat#563735; RRID: AB_2738394
Anti-mouse CD16/32 (Mouse BD Fc Block™) Monoclonal Antibody (Rat, clone 2.4G2), unconjugated	BD Biosciences	Cat#553142; RRID: AB_394657
Anti-mouse CD19 Monoclonal Antibody (Rat, clone 1D3), PE conjugated	BD Biosciences	Cat#553786; RRID: AB_395050
Anti-mouse CD19 Monoclonal Antibody (Rat, clone 1D3), RB780 conjugated	BD Biosciences	Cat#755522; RRID: AB_3676664
Anti-mouse CD24 Monoclonal Antibody (Mouse, clone M1/69), biotin conjugated	BioLegend	Cat#101803; RRID: AB_312836
Anti-mouse CD31 Monoclonal Antibody (Rat, clone 390), BV785 conjugated	BioLegend	Cat#102435; RRID: AB_2810334
Anti-mouse CD43 Monoclonal Antibody (Rat, clone S7), RY586 conjugated	BD Biosciences	Cat#753416
Anti-mouse CD45 Monoclonal Antibody (Rat, clone 30-F11), AF700 conjugated	Thermo Fisher Scientific	Cat# 56-0451-82, RRID: AB_891454
Anti-mouse CD45.1 Monoclonal Antibody (Mouse, clone A20), BUV395 conjugated	BD Biosciences	Cat#565212; RRID: AB_2722493
Anti-mouse CD45.1 Monoclonal Antibody (Mouse, clone A20), APC conjugated	BD Biosciences	Cat#558701; RRID: AB_1645214
Anti-mouse CD45.2 Monoclonal Antibody (Mouse, clone 104), BUV395 conjugated	BD Biosciences	Cat#564616; RRID: AB_2738867
Anti-mouse CD45.2 Monoclonal Antibody (Mouse, clone 104), FITC conjugated	BD Biosciences	Cat#561874; RRID: AB_10894189
Anti-mouse CD45.2 Monoclonal Antibody (Mouse, clone 104), PE-Cy7 conjugated	BD Biosciences	Cat#560696; RRID: AB_1727494
Anti-mouse CD45.2 Monoclonal Antibody (Mouse, clone 104), PerCP-Cy5.5 conjugated	BD Biosciences	Cat#552950; RRID: AB_394528
Anti-mouse CD45.2 Monoclonal Antibody (Mouse, clone 104), V500 conjugated	BD Biosciences	Cat#562129; RRID: AB_10897142
Anti-mouse CD49b Monoclonal Antibody (Rat, clone DX5), PE conjugated	BioLegend	Cat#108907; RRID: AB_313414
Anti-mouse CD52 Monoclonal Antibody (Rat, clone S20005A), PE conjugated	BioLegend	Cat#165705; RRID: AB_3662205

Anti-mouse CD62L Monoclonal Antibody (Rat, clone MEL-14), BV421 conjugated	BD Biosciences	Cat#562910; RRID: AB_2737885
Anti-mouse CD64 Monoclonal Antibody (Rabbit, clone 027), unconjugated	Thermo Fisher Scientific	Cat#MA5-29706; RRID: AB_2785530
Anti-mouse CD64 Monoclonal Antibody (Mouse, clone X54-5/7.1), BV421 conjugated	BioLegend	Cat#139309; RRID: AB_2562694
Anti-mouse CD64 Monoclonal Antibody (Mouse, clone X54-5/7.1), PE-Dazzle594 conjugated	BioLegend	Cat#139320; RRID: AB_2566559
Anti-mouse CD115 (CSF1R) Monoclonal Antibody (Rat, clone AFS98), AF488 conjugated	BioLegend	Cat#135511; RRID: AB_11218605
Anti-mouse CD115 (CSF1R) Monoclonal Antibody (Rat, clone AFS98), BV605 conjugated	BioLegend	Cat#135517; RRID: AB_2562760
Anti-mouse CD115 (CSF1R) Monoclonal Antibody (Rat, clone AFS98), APC conjugated	Thermo Fisher Scientific	Cat#17-1152-82; RRID: AB_1210789
Anti-mouse CD115 (CSF1R) Monoclonal Antibody (Rat, clone AFS98), PerCP-Cy5.5 conjugated	BioLegend	Cat#135526; RRID: AB_2566462
Anti-mouse CD163 Monoclonal Antibody (Rat, clone TNKUPJ), APC conjugated	Thermo Fisher Scientific	Cat#17-1631-80; RRID: AB_2784645
Anti-mouse CD163 Monoclonal Antibody (Rat, clone TNKUPJ), PE-eF610 conjugated	Thermo Fisher Scientific	Cat#61-1631-80; RRID: AB_2848497
Anti-mouse CD170 (SiglecF) Monoclonal Antibody (Rat, clone S17007L), FITC conjugated	BioLegend	Cat# 155504; RRID: AB_2750233
Anti-mouse CD170 (SiglecF) Monoclonal Antibody (Rat, clone E50-2440), PE conjugated	BD Biosciences	Cat#552126; RRID: AB_394341
Anti-mouse CD170 (SiglecF) Monoclonal Antibody (Rat, clone E50-2440), PE-CF594 conjugated	BD Biosciences	Cat#562757; RRID: AB_2687994
Anti-mouse CD170 (SiglecF) Monoclonal Antibody (Rat, clone E50-2440), BV750 conjugated	BD Biosciences	Cat#747316; RRID: AB_2872024
Anti-mouse CD177 Monoclonal Antibody (Rat, clone Y127), AF647 conjugated	BD Biosciences	Cat#566599; RRID: AB_2869790
Anti-mouse CD206 (MMR) Monoclonal Antibody (Rat, clone C068C2), AF647 conjugated	BioLegend	Cat#141712; RRID: AB_10900420
Anti-mouse CD206 (MMR) Monoclonal Antibody (Rat, clone C068C2), PE-Cy7 conjugated	BioLegend	Cat#141719; RRID: AB_2562247
Anti-mouse CD319 (CRACC) Monoclonal Antibody (Rat, clone 4G2), BV711 conjugated	BD Biosciences	Cat#747994; RRID: AB_2872455
Anti-mouse Clec-2 Monoclonal Antibody (Rat, clone 17D9), PE conjugated	BioLegend	Cat#146104; RRID: AB_2562383
Anti-mouse Clec4f Polyclonal Antibody (Goat), unconjugated	R&D Systems	Cat# AF2784; RRID: AB_2081339

Anti-mouse F4/80 Monoclonal Antibody (Rat, BM8), FITC conjugated	BioLegend	Cat#123108; RRID: AB_893502
Anti-mouse F4/80 Monoclonal Antibody (Rat, BM8), PE conjugated	Sony Biotechnology	Cat#1215550
Anti-mouse F4/80 Monoclonal Antibody (Rat, BM8), BV650 conjugated	BioLegend	Cat#123149; RRID: AB_2564589
Anti-mouse F4/80 Monoclonal Antibody (Rat, BM8), BV785 conjugated	BioLegend	Cat#123141; RRID: AB_2563667
Anti-mouse F4/80 Monoclonal Antibody (Rat, BM8), APC-eFluor 780 conjugated	Thermo Fisher Scientific	Cat# 47-4801-82; RRID: AB_2735036
Anti-mouse FCRLS Monoclonal Antibody (Rat, 4G11), AF647 conjugated	Butovsky Lab, validated in [76]	N/A
Anti-mouse FR-β Monoclonal Antibody (Rat, 10/FR2), APC conjugated	BioLegend	Cat#153305; RRID: AB_2721312
Anti-H3K27ac Monoclonal Antibody (Mouse), unconjugated	Thermo Fisher Scientific	Cat#MA5-23516; RRID: AB_2608307
Anti-mouse I-A/I-E (MHC-II) Monoclonal Antibody (Rat, clone M5/114.15.2), BV421 conjugated	BioLegend	Cat#107632; RRID: AB_10900075
Anti-mouse I-A/I-E (MHC-II) Monoclonal Antibody (Rat, clone M5/114.15.2), PerCP-Cy5.5 conjugated	BioLegend	Cat#107625; RRID: AB_2191072
Anti-mouse I-A/I-E (MHC-II) Monoclonal Antibody (Rat, clone M5/114.15.2), AF700 conjugated	Thermo Fisher Scientific	Cat#56-5321-80; RRID: AB_494010
Anti-goat IgG (H+L) Cross-Adsorbed Secondary Polyclonal Antibody (Donkey), AF555 conjugated	Thermo Fisher Scientific	Cat#A-21432; RRID: AB_2535853
Anti-rat IgG (H+L) Cross-Adsorbed Secondary Polyclonal Antibody (Donkey), AF488 conjugated	Thermo Fisher Scientific	Cat#A-21208; RRID: AB_141709
Anti-rabbit IgG (H+L) Cross-Adsorbed Secondary Polyclonal Antibody (Goat), AF488 conjugated	Thermo Fisher Scientific	Cat#A-11008; RRID: AB_143165
Anti-rabbit IgG (H+L) Cross-Adsorbed Secondary Polyclonal Antibody (Goat), AF647 conjugated	Thermo Fisher Scientific	Cat#A-31573; RRID: AB_2536183
Anti-rabbit IgG (minimal x-reactivity) Secondary Polyclonal Antibody (Donkey), AF647 conjugated	BioLegend	Cat#406414, RRID: AB_2563202
Anti-mouse Ly6C Monoclonal Antibody (Rat, clone AL-21), PE-CF594 conjugated	BD Biosciences	Cat#562728; RRID: AB_2737749
Anti-mouse Ly6C Monoclonal Antibody (Rat, clone HK1.4), BV570 conjugated	BioLegend	Cat#128030; RRID: AB_2562617
Anti-mouse Ly6C Monoclonal Antibody (Rat, clone HK1.4), AF700 conjugated	BioLegend	Cat#128024; RRID: AB_10643270
Anti-mouse Ly6G Monoclonal Antibody (Rat, clone 1A8), PE conjugated	BD Biosciences	Cat#551461; RRID: AB_394208
Anti-mouse Ly6G Monoclonal Antibody (Rat, clone 1A8), BV650 conjugated	BD Biosciences	Cat#740554; RRID: AB_2740255
Anti-mouse Ly6G Monoclonal Antibody (Rat, clone 1A8), PE-Cy7 conjugated	BD Biosciences	Cat#560601; RRID: AB_1727562
Anti-mouse MafB Recombinant Monoclonal Antibody (Rabbit, clone BLR046F), unconjugated	Bethyl	Cat#A700-046; RRID: AB_2891845

Anti-human MAFB Polyclonal Antibody (Rabbit), unconjugated	Cell Signaling Technology	Cat#41019; RRID: AB_2799192
Anti-mouse MerTK Monoclonal Antibody (Rat, clone DS5MMER), PerCP-eF710 conjugated	Thermo Fisher Scientific	Cat#46-5751-82; RRID: AB_2688094
Anti-mouse MerTK Monoclonal Antibody (Rat, clone DS5MMER), PE-Cy7 conjugated	Thermo Fisher Scientific	Cat#25-5751-80; RRID: AB_2573465
Anti-mouse NK1.1 Monoclonal Antibody (Mouse, clone PK136), AF660 conjugated	Thermo Fisher Scientific	Cat#606-5941-82; RRID: AB_2896296
Anti-mouse P2ry12 Monoclonal Antibody (Rat, clone S16007D), AF488 conjugated	BioLegend	Cat#848015; RRID: AB_2936702
Anti-mouse RELMα Monoclonal Antibody (Rat, clone DS8RELM), APC conjugated	Thermo Fisher Scientific	Cat#17-5441-82; RRID: AB_2762696
Anti-mouse Tim4 Monoclonal Antibody (Rat, clone RMT4-54), unconjugated	BioLegend	Cat# 130002; RRID: AB_1227802
Anti-mouse Tim4 Monoclonal Antibody (Rat, clone RMT4-54), AF647 conjugated	BioLegend	Cat#130007; RRID: AB_2201842
Anti-mouse Tim4 Monoclonal Antibody (Rat, clone RMT4-54), PE-Cy7 conjugated	BioLegend	Cat#130009; RRID: AB_2565718
Anti-mouse Vsig4 Monoclonal Antibody (Rat, clone NLA14), APC conjugated	Thermo Fisher Scientific	Cat#17-5752-80; RRID: AB_2637428
Anti-mouse Vsig4 Monoclonal Antibody (Rat, clone NLA14), SB600 conjugated	Thermo Fisher Scientific	Cat#63-5752-82; RRID: AB_2802437
Anti-mouse Vsig4 Monoclonal Antibody (Rat, clone NLA14), PE-Cy7 conjugated	Thermo Fisher Scientific	Cat#25-5752-82; RRID: AB_2637431
Anti-mouse XCR1 Monoclonal Antibody (Mouse, clone ZET), BV510 conjugated	BioLegend	Cat#148218; RRID: AB_2565231
Rabbit IgG Isotype Control Antibody (Rabbit, polyclonal), unconjugated	Thermo Fisher Scientific	Cat#31235; RRID: AB_243593
Rabbit IgG CUT&RUN Negative Control Antibody (Rabbit, polyclonal)	EpiCypher	Cat#13-0042; RRID: AB_2923178
TotalSeq™-B0301 anti-mouse Hashtag 1 Antibody	BioLegend	Cat#155831; RRID: AB_2814067
TotalSeq™-B0302 anti-mouse Hashtag 2 Antibody	BioLegend	Cat#155833; RRID: AB_2814068
TotalSeq™-B0303 anti-mouse Hashtag 3 Antibody	BioLegend	Cat#155835; RRID: AB_2814069
Chemicals, peptides, and recombinant proteins		
1,4-Dithiothreitol (DTT)	Sigma-Aldrich	Cat#10197777001
2-Mercaptoethanol	Thermo Fisher Scientific	Cat#31350010
Antigenfix	Diapath	Cat#P0014
Alizarin Red S	Thermo Fisher Scientific	Cat#400480250
Baytrill (enrofloxacine)	Bayer	Cat#616300
Bovine Serum Albumin (BSA)	Sigma-Aldrich	Cat#A7906
Brilliant Stain Buffer	BD Biosciences	Cat#563794
Collagenase A, from *Clostridium histolyticum*	Sigma-Aldrich	Cat#11088793001
Collagenase IV, from *Clostridium histolyticum*	Thermo Fisher Scientific	Cat#17104019
Collagenase VIII, from *Clostridium histolyticum*	Sigma-Aldrich	Cat#C2139
cOmplete™ Protease Inhibitor Cocktail	Sigma-Aldrich	Cat#11697498001
cOmplete™ EDTA-free Protease Inhibitor Cocktail	Sigma-Aldrich	Cat#11873580001
DAPI	Thermo Fisher Scientific	Cat#D3571
Dispase II	Sigma-Aldrich	Cat#D4693
Donkey Serum	Abcam	Cat#ab7475
DNase I	Sigma-Aldrich	Cat#11284932001
DPBS	Thermo Fisher Scientific	Cat#14190094
EDTA	Merck Millipore	Cat#1084181000

Fetal Bovine Serum (FBS)	Thermo Fisher Scientific	Cat#10270098
Glycine	Merck	Cat#104691000
Glycerol	Thermo Fisher Scientific	Cat#158920025
GlycoBlue™ Coprecipitant	Thermo Fisher Scientific	Cat#AM9515
HBSS without Phenol Red	Thermo Fisher Scientific	Cat# 14025050
HBSS with Phenol Red	Lonza	Cat#BE10-508F
IsoFlo (Isoflurane)	Zoetis	Cat#B506
MEM Non-Essential Amino Acids Solution	Thermo Fisher Scientific	Cat# 11140050
Mouse M-CSF Recombinant Protein	PeproTech	Cat#315-02
Nimatek (Ketamine)	Dechra	Cat#804132
Nonidet P 40 Substitute	Sigma-Aldrich	Cat#74385
Formaldehyde	Thermo Fisher Scientific	Cat#BP531-500
Percoll	GE Healthcare	Cat#17089101
PKH26	Sigma-Aldrich	Cat#MIDI26
ProLong™ Diamond Antifade Mountant	Thermo Fisher Scientific	Cat#P36970
Rompun (Xylazine)	Bayer	Cat#0076901
RPMI 1640 Medium	Thermo Fisher Scientific	Cat#21875034
Saponin	Sigma-Aldrich	Cat#4521
Sodium Pyruvate	Thermo Fisher Scientific	Cat#11360070
Streptavidin, PE-CF594 conjugated	BD Biosciences	Cat#562318; RRID: AB_11154218
Streptavidin, APC conjugated	BD Biosciences	Cat#554067; RRID: AB_10050396)
SYTOX™ Blue	Thermo Fisher Scientific	Cat#S11348
Tris(hydroxymethyl)aminomethane	Merck Millipore	Cat#108382
TRIzol Reagent	Thermo Fisher Scientific	Cat#10296010
Triton X-100	Merck	Cat#648466
Tween-20	Thermo Fisher Scientific	Cat#233360010
UltraPure BSA	Thermo Fisher Scientific	Cat#AM2616
Critical commercial assays		
Chromium Next GEM Single Cell 3' GEM, Library & Gel Bead Kit v3.1	10X Genomics	Cat#1000128
Chromium Next GEM Chip G Single Cell Kit	10X Genomics	Cat#1000120
Classical Monocyte Isolation Kit, human	Miltenyi Biotec	Cat#130-117-337
CUTANA™ ChIC/CUT&RUN Kit	EpiCypher	Cat#14-1048
CUTANA™ CUT&RUN Library Prep Kit	EpiCypher	Cat#14-1001
FoxP3 Transcription Factor Staining Kit	Thermo Fisher Scientific	Cat#00-5523-00
LIVE/DEAD™ Fixable Near-IR Dead Cell Stain Kit	Thermo Fisher Scientific	Cat#L34976
Monocyte Isolation Kit (BM), mouse	Miltenyi Biotec	Cat#130-100-629
NovaSeq 6000 S4 Reagent Kit v1.5 (300 cycles)	Illumina	Cat#20028312
pHrodo™ Red S. aureus BioParticles™ Conjugate for Phagocytosis	Thermo Fisher Scientific	Cat#A10010
RNA Clean & Concentrator Kit	Zymo Research	Cat#R1013
TruSeq Stranded mRNA kit	Illumina	Cat#20020594
Deposited data		
Microarray data	ImmGen	https://www.immgen.org/; RRID: SCR_021792
Tabula Muris Senis	The Tabula Muris Consortium[40]	https://registry.opendata.aws/tabula-muris-senis/; GEO: GSE132042
RNA-Seq of BMDM from *Mafb*$^{fl/fl}$ and *Lyz2*^{Cre}*Mafb*$^{fl/fl}$ mice	This paper	GEO: GSE286897

scRNA-Seq of RTM from *Mafb*$^{fl/fl}$ and *Lyz2*^{Cre}*Mafb*$^{fl/fl}$ mice	This paper	GEO: GSE287347
scRNA-Seq of lung IM from *Mafb*$^{fl/fl}$ and *Lyz2*^{Cre}*Mafb*$^{fl/fl}$ mice	Vanneste et al. [37]	GEO: GSE193891
MafB CUT&RUN of BMDM from *Mafb*$^{fl/fl}$ and *Lyz2*^{Cre}*Mafb*$^{fl/fl}$ mice	This paper	GEO: GSE287346
H3K27ac CUT&RUN of BMDM from *Lyz2*^{Cre} *Mafb*$^{fl/fl}$ mice and *Mafb*$^{fl/fl}$ littermate controls	This paper	GEO: GSE287476
MafB CUT&RUN of LPM from *Mafb*$^{fl/fl}$ and *Lyz2*^{Cre}*Mafb*$^{fl/fl}$ mice	This paper	GEO: GSE287346
MafB CUT&RUN of MDM	This paper	GEO: GSE287346
PU.1 ChIP-Seq data	Soucie et al. [39] ChIP-Atlas	http://chip-atlas.org/; RRID: SCR_015511; GEO: GSM1964736
Tabula Sapiens	The Tabula Sapiens Consortium[77]	https://registry.opendata.aws/tabula-sapiens/; GEO: GSE201333
Tabula Microcebus	The Tabula Microcebus Consortium[78]	https://figshare.com/projects/Tabula_Microcebus/112227
Pig Cell Atlas	Wang et al.[79]	https://dreamapp.biomed.au.dk/pigatlas/; GEO: GSE196055, GSE193975
Xenopus Cell Landscape	Liao et al.[80]	https://doi.org/10.6084/m9.figshare.19152839; GEO: GSE195790
Zebrafish Cell Landscape	Wang et al. [81]	https://figshare.com/s/1ab3c6d7648d12247eb2; GEO: GSE198571, GSE178150
Experimental models: Organisms/strains		
Mouse: C57BL/6J	The Jackson Laboratory	N/A
Mouse: C57BL/6J CD45.1: B6.SJL-*Ptprc*^{a} *Pepc*^{b}/BoyJ	The Jackson Laboratory	Cat#002014; RRID: IMSR_JAX:002014
Mouse: *Lyz2*^{Cre}: B6.129P2-*Lyz2*$^{tm1(cre)Ifo}$/J	Clausen et al. [66] The Jackson Laboratory	Cat#004781; RRID: IMSR_JAX:004781
Mouse: *Clec4f*^{Cre}: *Clec4f*$^{tm2.1(icre)Ciphe}$	Scott et al. [25]	N/A
Mouse: *Tmem119*^{CreERT2}: C57BL/6-*Tmem119*$^{em1(cre/ERT2)Gfng}$/J	Kaiser et al. [67] The Jackson Laboratory	Cat#031820; RRID: IMSR_JAX:031820
Mouse: *Maf*$^{fl/fl}$: *Maf*$^{tm2.1Cbm}$	Wende et al. [65]	N/A
Mouse: *Mafb*$^{fl/fl}$: *Mafb*$^{tm1.1Mari}$	Vanneste et al.[37]	N/A
Software and algorithms		
BioRender	BioRender	https://www.biorender.com/; RRID: SCR_018361
Cell Ranger	10X Genomics	RRID: SCR_023221
Code for analysis sequencing data	This paper	https://github.com/dovneste/MafB_Mac
ETE Toolkit	Huerta-Cepas et al.[82]	https://etetoolkit.org/
FIJI (ImageJ)	Schindelin et al.[83]	https://imagej.net/Fiji; RRID: SCR_003070
FlowJo	TreeStar	https://www.flowjo.com/; RRID: SCR_008520
Gene Set Enrichment Analysis	Subramanian et al. [84]	http://www.broadinstitute.org/gsea/; RRID: SCR_003199
g:Profiler	Kolberg et al. [85]	http://biit.cs.ut.ee/gprofiler/; RRID: SCR_006809

GraphPad Prism	GraphPad Software	https://www.graphpad.com/scientific-software/prism/; RRID: SCR_002798
HOMER	Heinz et al.[86]	http://homer.ucsd.edu/; RRID: SCR_010881
Illustrator	Adobe	https://www.adobe.com/; RRID: SCR_010279
Integrative Genomic Viewer	Robinson et al. [87]	https://igv.org; RRID: SCR_011793
nf-core	Ewels et al.[88]	https://nf-co.re/
QuPath	Bankhead et al.[89]	https://qupath.github.io/; RRID: SCR_018257
R Project for Statistical Computing	The R Foundation	http://www.r-project.org/; RRID: SCR_001905
SEACR	Meers et al.[72]	https://seacr.fredhutch.org/
scikit-image	van der Walt et al. [90]	https://scikit-image.org/; RRID: SCR_021142
UCSC Genome Browser	Perez et al.[91]	http://genome.ucsc.edu/; RRID: SCR_005780
Other		
Axioscan 7	Zeiss	N/A
Chromium iX	10X Genomics	N/A
LSM 980	Zeiss	N/A
LSRFortessa™ Cell Analyzer	BD Biosciences	N/A
MA900 Multi-Application Cell Sorter	Sony Biotechnology	N/A
NovaSeq 6000	Illumina	N/A

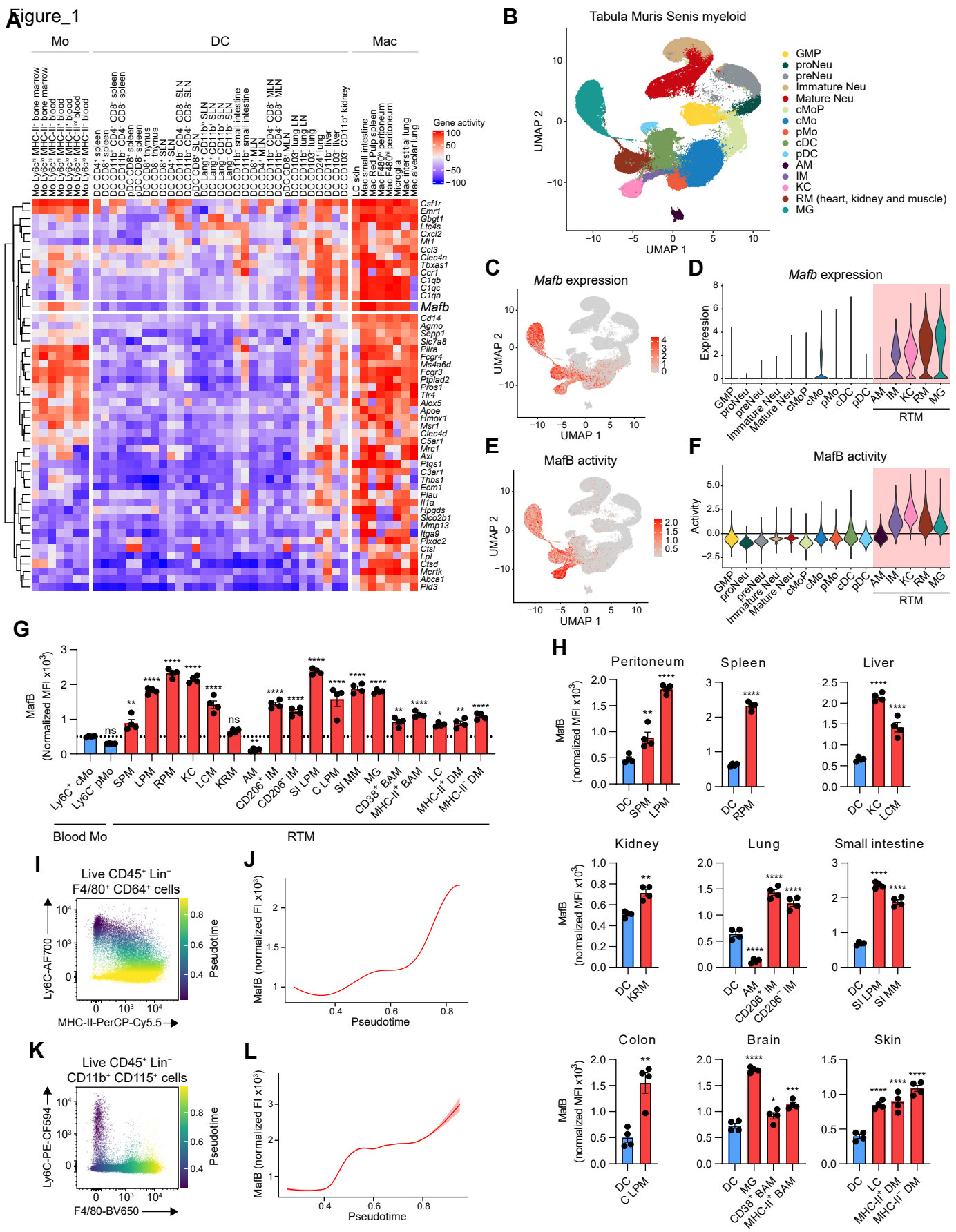
Figure_1
A
Mo
DC
Mac
Gene activity
100
50
0
−50
−100
Csf1r
Emr1
Gbgt1
Ltc4s
Cxcl2
Mt1
Ccl3
Clec4n
Tbxas1
Ccr1
C1qb
C1qc
C1qa
Mafb
Cd14
Agmo
Sepp1
Slc7a8
Pilra
Fcgr4
Ms4a6d
Fcgr3
Ptplad2
Pros1
Tlr4
Alox5
Apoe
Hmox1
Msr1
Clec4d
C5ar1
Mrc1
Axl
Ptgs1
C3ar1
Thbs1
Ecm1
Plau
Il1a
Hpgds
Slco2b1
Mmp13
Itga9
Plxdc2
Ctsl
Lpl
Ctsd
Mertk
Abca1
Pld3
B
Tabula Muris Senis myeloid
UMAP 1
UMAP 2
GMP
proNeu
preNeu
Immature Neu
Mature Neu
cMoP
cMo
pMo
cDC
pDC
AM
IM
KC
RM (heart, kidney and muscle)
MG
C
Mafb expression
D
Mafb expression
Expression
RTM
E
MafB activity
F
MafB activity
Activity
RTM
G
MafB
(Normalized MFI x10³)
Blood Mo
RTM
H
Peritoneum
Spleen
Liver
Kidney
Lung
Small intestine
Colon
Brain
Skin
MafB
(normalized MFI x10³)
I
Live CD45⁺ Lin⁻
F4/80⁺ CD64⁺ cells
Ly6C-AF700
MHC-II-PerCP-Cy5.5
Pseudotime
J
MafB (normalized FI x10³)
Pseudotime
K
Live CD45⁺ Lin⁻
CD11b⁺ CD115⁺ cells
Ly6C-PE-CF594
F4/80-BV650
Pseudotime
L
MafB (normalized FI x10³)
Pseudotime

Figure_2

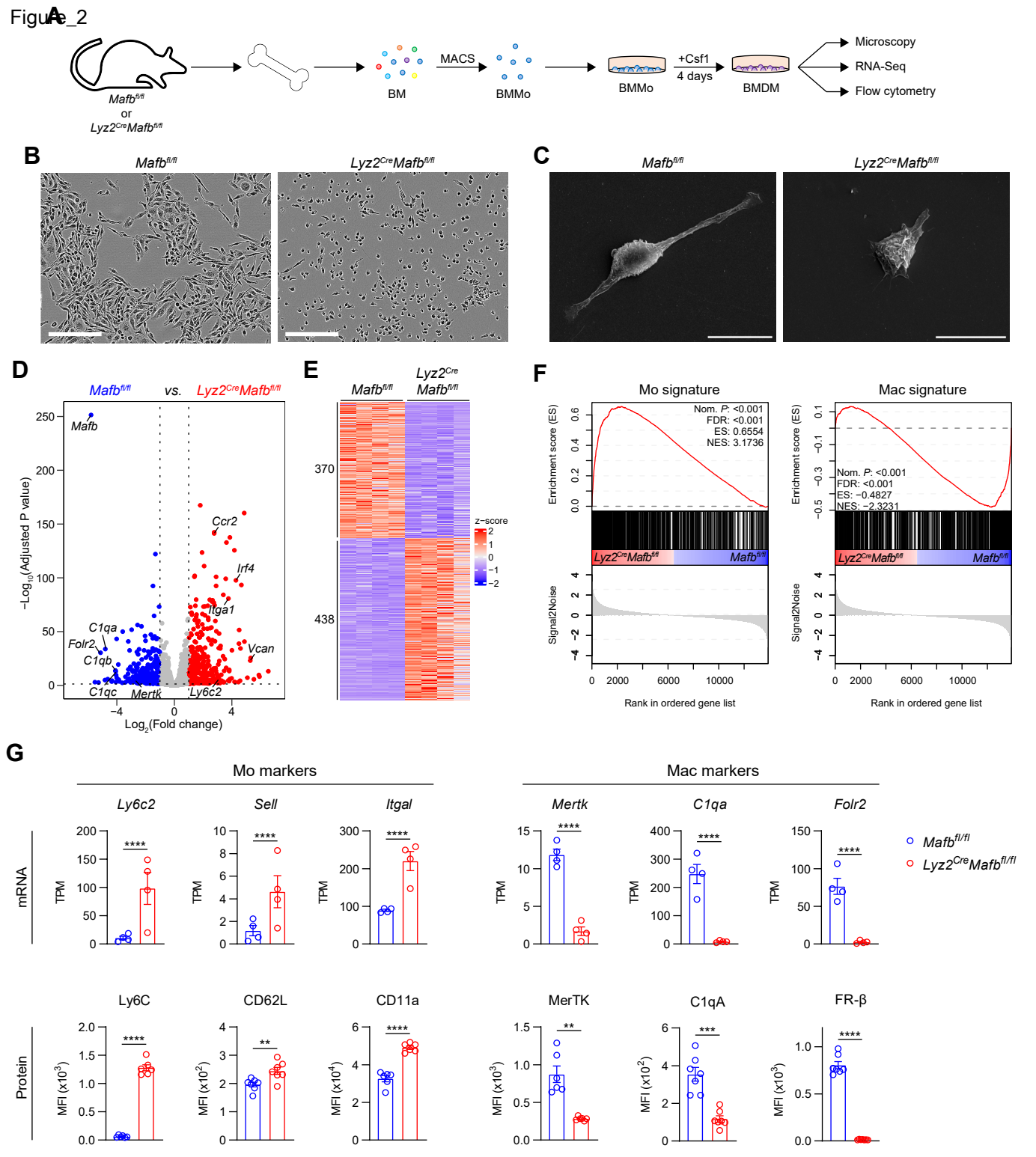
A
Mafb fl/fl
or
Lyz2Cre Mafb fl/fl
BM
MACS
BMMo
BMMo
+Csf1
4 days
BMDM
Microscopy
RNA-Seq
Flow cytometry
B
Mafb fl/fl
Lyz2Cre Mafb fl/fl
C
Mafb fl/fl
Lyz2Cre Mafb fl/fl
D
Mafb fl/fl
vs.
Lyz2Cre Mafb fl/fl
Mafb
Ccr2
Irf4
Itga1
C1qa
Folr2
C1qb
C1qc
Mertk
Ly6c2
Vcan
−Log10(Adjusted P value)
Log2(Fold change)
E
Mafb fl/fl
Lyz2Cre Mafb fl/fl
370
438
z−score
F
Mo signature
Mac signature
Enrichment score (ES)
Nom. P: <0.001
FDR: <0.001
ES: 0.6554
NES: 3.1736
Nom. P: <0.001
FDR: <0.001
ES: −0.4827
NES: −2.3231
Lyz2Cre Mafb fl/fl
Mafb fl/fl
Signal2Noise
Rank in ordered gene list
G
Mo markers
Mac markers
Ly6c2
Sell
Itgal
Mertk
C1qa
Folr2
mRNA
TPM
Mafb fl/fl
Lyz2Cre Mafb fl/fl
Protein
Ly6C
CD62L
CD11a
MerTK
C1qA
FR-β
MFI (x10³)
MFI (x10²)
MFI (x10⁴)

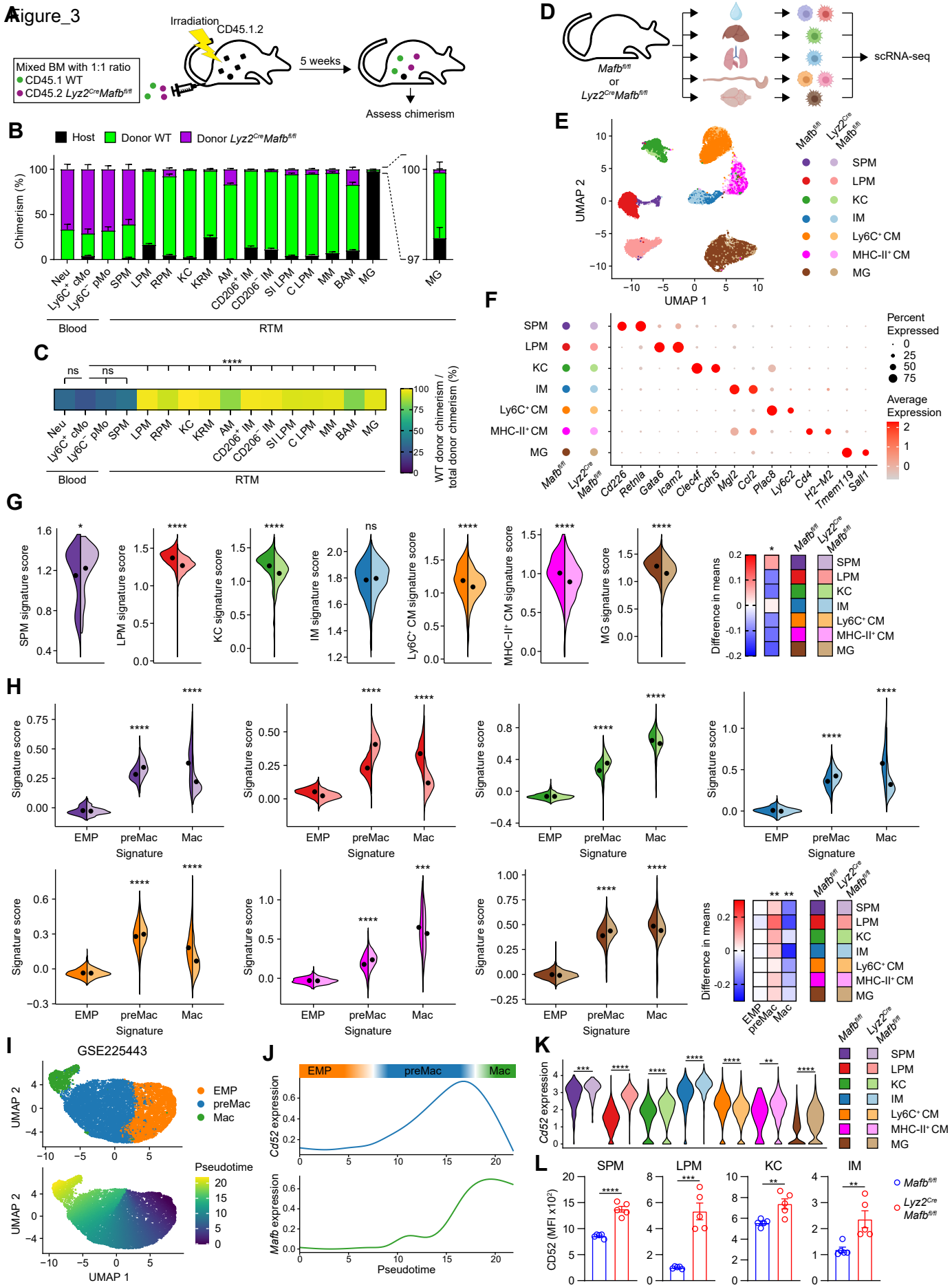
Figure_3
A
Irradiation
CD45.1.2
Mixed BM with 1:1 ratio
CD45.1 WT
CD45.2 Lyz2CreMaffl/fl
5 weeks
Assess chimerism
B
Host
Donor WT
Donor Lyz2CreMaffl/fl
Chimerism (%)
Neu
Ly6C+ cMo
Ly6C- pMo
SPM
LPM
RPM
KC
KRM
AM
CD206+ IM
CD206- IM
SI LPM
C LPM
MM
BAM
MG
Blood
RTM
C
ns
****
WT donor chimerism / total donor chimerism (%)
D
Maffl/fl
or
Lyz2CreMaffl/fl
scRNA-seq
E
UMAP 1
UMAP 2
SPM
LPM
KC
IM
Ly6C+ CM
MHC-II+ CM
MG
F
Percent Expressed
Average Expression
Cd226
Retnla
Gata6
Icam2
Clec4f
Cdh5
Mgl2
Ccl2
Plac8
Ly6c2
Cd4
H2-M2
Tmem119
Sall1
G
SPM signature score
LPM signature score
KC signature score
IM signature score
Ly6C+ CM signature score
MHC-II+ CM signature score
MG signature score
Difference in means
H
Signature score
EMP
preMac
Mac
Signature
I
GSE225443
Pseudotime
J
Cd52 expression
Maffa expression
K
L
SPM
LPM
KC
IM
CD52 (MFI x10²)

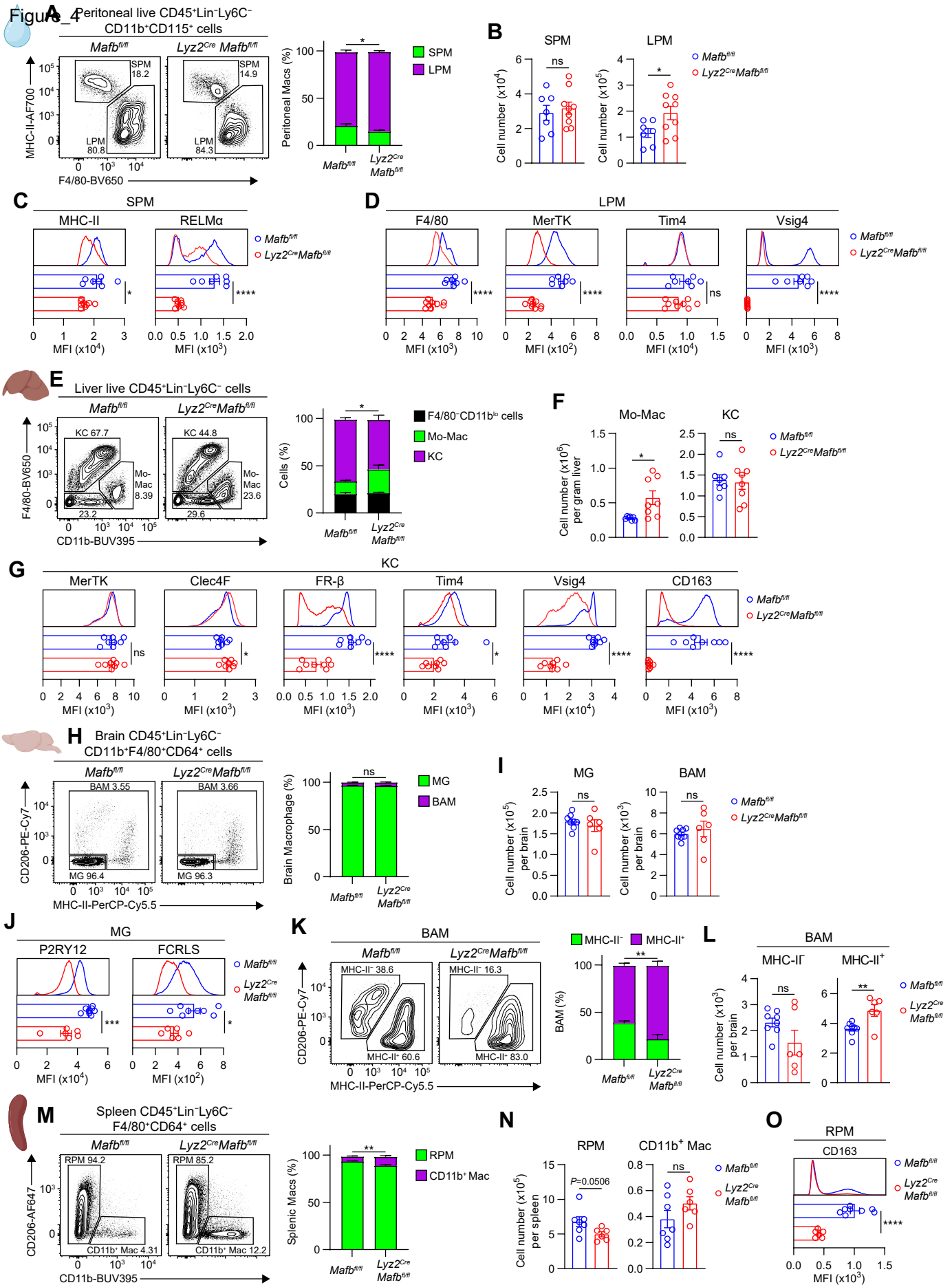
Figure_4
A
Peritoneal live CD45+Lin-Ly6C- CD11b+CD115+ cells
Mafbfl/fl
Lyz2Cre Mafbfl/fl
SPM 18.2
LPM 80.8
SPM 14.9
LPM 84.3
MHC-II-AF700
F4/80-BV650
Peritoneal Macs (%)
SPM
LPM
B
SPM
LPM
ns
Cell number (x10^4)
Cell number (x10^5)
C
SPM
MHC-II
RELMα
MFI (x10^4)
MFI (x10^3)
D
LPM
F4/80
MerTK
Tim4
Vsig4
MFI (x10^3)
MFI (x10^2)
MFI (x10^4)
E
Liver live CD45+Lin-Ly6C- cells
KC 67.7
Mo-Mac 8.39
KC 44.8
Mo-Mac 23.6
F4/80-BV650
CD11b-BUV395
Cells (%)
F4/80-CD11blo cells
Mo-Mac
KC
F
Mo-Mac
KC
Cell number (x10^6) per gram liver
G
KC
MerTK
Clec4F
FR-β
Tim4
Vsig4
CD163
MFI (x10^3)
MFI (x10^4)
H
Brain CD45+Lin-Ly6C- CD11b+F4/80+CD64+ cells
BAM 3.55
MG 96.4
BAM 3.66
MG 96.3
CD206-PE-Cy7
MHC-II-PerCP-Cy5.5
Brain Macrophage (%)
MG
BAM
I
MG
BAM
Cell number (x10^5) per brain
Cell number (x10^3) per brain
J
MG
P2RY12
FCRLS
MFI (x10^4)
MFI (x10^2)
K
BAM
MHC-II- 38.6
MHC-II+ 60.6
MHC-II- 16.3
MHC-II+ 83.0
MHC-II-
MHC-II+
BAM (%)
L
BAM
MHC-II-
MHC-II+
Cell number (x10^3) per brain
M
Spleen CD45+Lin-Ly6C- F4/80+CD64+ cells
RPM 94.2
CD11b+ Mac 4.31
RPM 85.2
CD11b+ Mac 12.2
CD206-AF647
CD11b-BUV395
Splenic Macs (%)
RPM
CD11b+ Mac
N
RPM
CD11b+ Mac
P=0.0506
Cell number (x10^5) per spleen
O
RPM
CD163
MFI (x10^3)
Mafbfl/fl
Lyz2Cre Mafbfl/fl

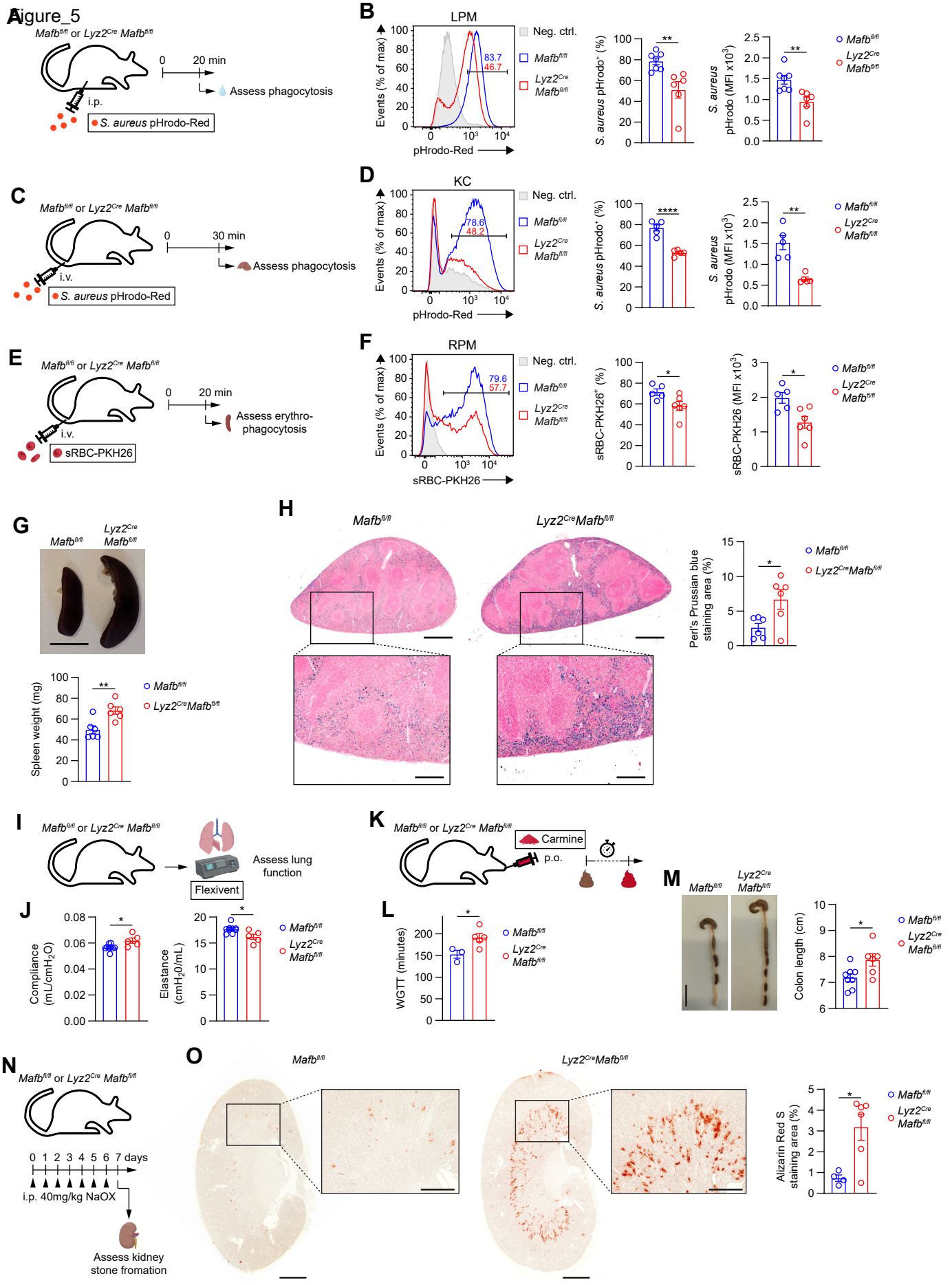
Figure_5
A
Mafb fl/fl or Lyz2 Cre Mafb fl/fl
0
20 min
Assess phagocytosis
i.p.
S. aureus pHrodo-Red
B
LPM
Events (% of max)
pHrodo-Red
Neg. ctrl.
Mafb fl/fl
Lyz2 Cre Mafb fl/fl
83.7
46.7
S. aureus pHrodo+ (%)
S. aureus pHrodo (MFI x10 3)
C
30 min
i.v.
D
KC
78.6
48.2
E
sRBC-PKH26
Assess erythro-phagocytosis
F
RPM
79.6
57.7
G
Spleen weight (mg)
H
Perl's Prussian blue staining area (%)
I
Flexivent
Assess lung function
J
Compliance (mL/cmH2O)
Elastance (cmH2O/mL)
K
Carmine
p.o.
L
WGTT (minutes)
M
Colon length (cm)
N
0 1 2 3 4 5 6 7 days
i.p. 40mg/kg NaOX
Assess kidney stone fromation
O
Alizarin Red S staining area (%)

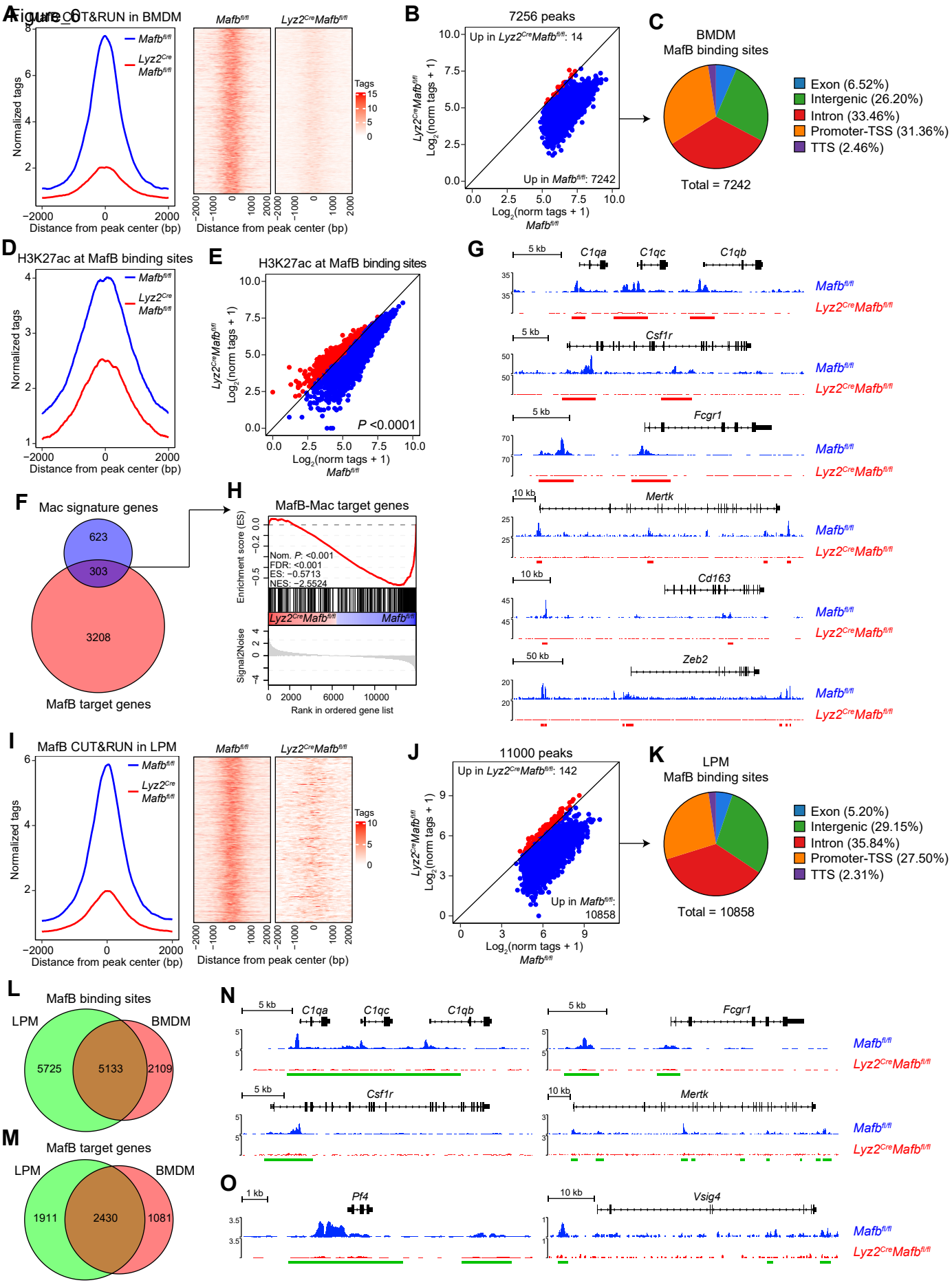
Figure 6
A
MafB CUT&RUN in BMDM
Mafb fl/fl
Lyz2Cre Mafb fl/fl
Normalized tags
Distance from peak center (bp)
Tags
B
7256 peaks
Up in Lyz2Cre Mafb fl/fl: 14
Up in Mafb fl/fl: 7242
Log2(norm tags + 1)
C
BMDM
MafB binding sites
Exon (6.52%)
Intergenic (26.20%)
Intron (33.46%)
Promoter-TSS (31.36%)
TTS (2.46%)
Total = 7242
D
H3K27ac at MafB binding sites
E
H3K27ac at MafB binding sites
P <0.0001
F
Mac signature genes
623
303
3208
MafB target genes
H
MafB-Mac target genes
Nom. P: <0.001
FDR: <0.001
ES: −0.5713
NES: −2.5524
Enrichment score (ES)
Signal2Noise
Rank in ordered gene list
G
C1qa
C1qc
C1qb
Csf1r
Fcgr1
Mertk
Cd163
Zeb2
5 kb
10 kb
50 kb
I
MafB CUT&RUN in LPM
J
11000 peaks
Up in Lyz2Cre Mafb fl/fl: 142
Up in Mafb fl/fl: 10858
K
LPM
MafB binding sites
Exon (5.20%)
Intergenic (29.15%)
Intron (35.84%)
Promoter-TSS (27.50%)
TTS (2.31%)
Total = 10858
L
MafB binding sites
LPM
BMDM
5725
5133
2109
M
MafB target genes
1911
2430
1081
N
O
Pf4
Vsig4
1 kb

Figure_7

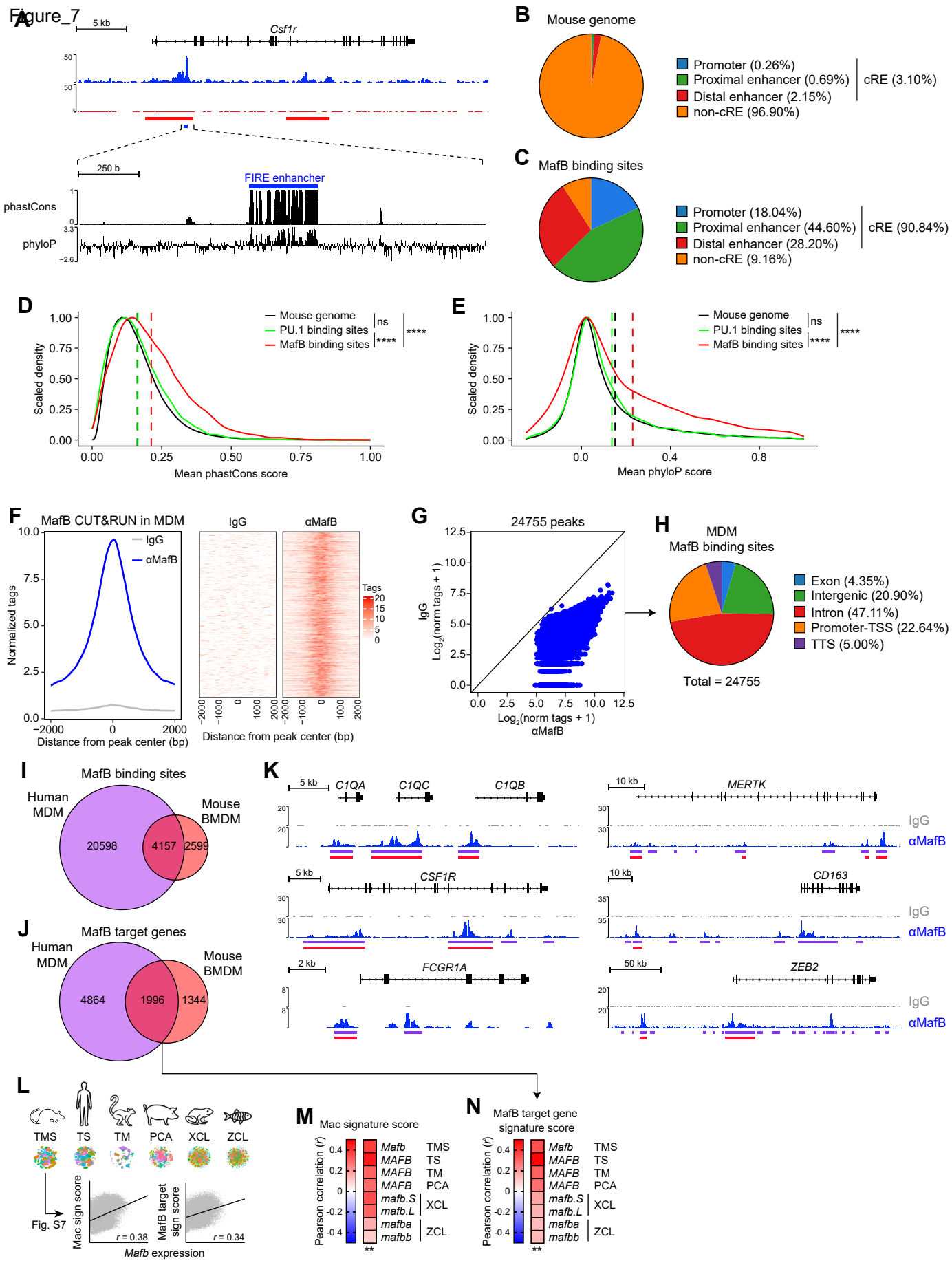
A
5 kb
Csf1r
250 b
FIRE enhancer
phastCons
phyloP
B
Mouse genome
Promoter (0.26%)
Proximal enhancer (0.69%)
Distal enhancer (2.15%)
non-cRE (96.90%)
cRE (3.10%)
C
MafB binding sites
Promoter (18.04%)
Proximal enhancer (44.60%)
Distal enhancer (28.20%)
non-cRE (9.16%)
cRE (90.84%)
D
Scaled density
Mean phastCons score
Mouse genome
PU.1 binding sites
MafB binding sites
ns
****
E
Scaled density
Mean phyloP score
F
MafB CUT&RUN in MDM
IgG
αMafB
Normalized tags
Distance from peak center (bp)
Tags
G
24755 peaks
IgG
αMafB
H
MDM
MafB binding sites
Exon (4.35%)
Intergenic (20.90%)
Intron (47.11%)
Promoter-TSS (22.64%)
TTS (5.00%)
Total = 24755
I
MafB binding sites
Human MDM
Mouse BMDM
20598
4157
2599
J
MafB target genes
Human MDM
Mouse BMDM
4864
1996
1344
K
C1QA
C1QC
C1QB
MERTK
CSF1R
CD163
FCGR1A
ZEB2
IgG
αMafB
L
TMS
TS
TM
PCA
XCL
ZCL
Fig. S7
Mac sign score
MafB target sign score
r = 0.38
r = 0.34
Mafb expression
M
Mac signature score
Pearson correlation (r)
Mafb
MAFB
mafb.S
mafb.L
mafba
mafbb
N
MafB target gene signature score

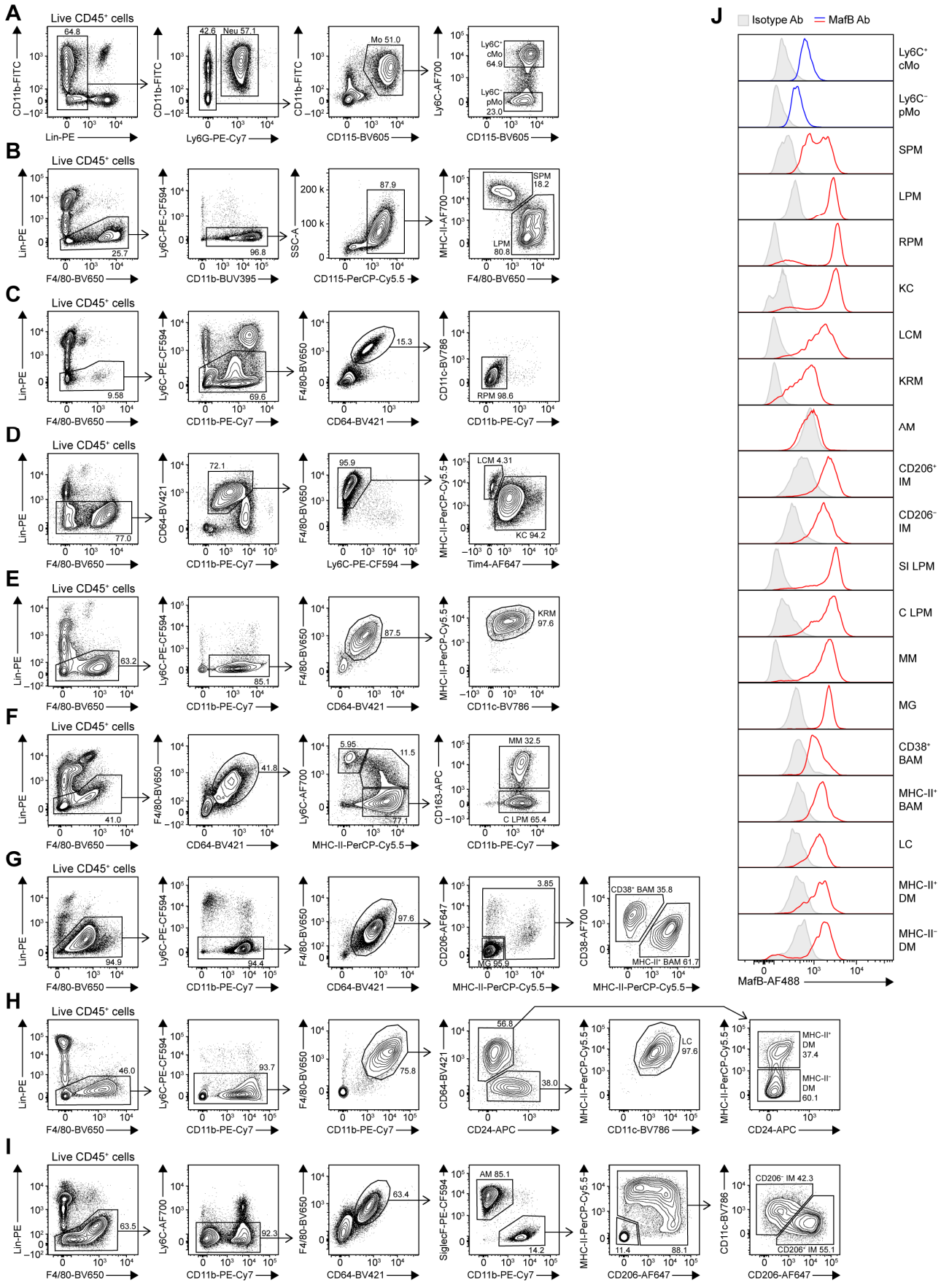
A
Live CD45⁺ cells
CD11b-FITC
Lin-PE
64.8
Ly6G-PE-Cy7
42.6
Neu 57.1
CD115-BV605
Mo 51.0
Ly6C-AF700
Ly6C⁺ cMo 64.9
Ly6C⁻ pMo 23.0
B
Live CD45⁺ cells
Lin-PE
F4/80-BV650
25.7
Ly6C-PE-CF594
CD11b-BUV395
96.8
SSC-A
CD115-PerCP-Cy5.5
87.9
MHC-II-AF700
SPM 18.2
LPM 80.8
C
Live CD45⁺ cells
9.58
CD11b-PE-Cy7
69.6
CD64-BV421
15.3
CD11c-BV786
RPM 98.6
D
Live CD45⁺ cells
77.0
72.1
95.9
Tim4-AF647
LCM 4.31
KC 94.2
E
Live CD45⁺ cells
63.2
85.1
87.5
KRM 97.6
F
Live CD45⁺ cells
41.0
41.8
MHC-II-PerCP-Cy5.5
5.95
11.5
77.1
CD163-APC
MM 32.5
C LPM 65.4
G
Live CD45⁺ cells
94.9
94.4
97.6
CD206-AF647
3.85
MC 95.3
CD38-AF700
CD38⁺ BAM 35.8
MHC-II⁺ BAM 61.7
H
Live CD45⁺ cells
46.0
93.7
75.8
CD24-APC
56.8
38.0
LC 97.6
MHC-II⁺ DM 37.4
MHC-II⁻ DM 60.1
I
Live CD45⁺ cells
63.5
92.3
63.4
SiglecF-PE-CF594
AM 85.1
14.2
11.4
88.1
CD206⁻ IM 42.3
CD206⁺ IM 55.1
J
Isotype Ab
MafB Ab
MafB-AF488
Ly6C⁺ cMo
Ly6C⁻ pMo
SPM
LPM
RPM
KC
LCM
KRM
AM
CD206⁺ IM
CD206⁻ IM
SI LPM
C LPM
MM
MG
CD38⁺ BAM
MHC-II⁺ BAM
LC
MHC-II⁺ DM
MHC-II⁻ DM

Figure S1. Flow cytometry gating strategies to delineate RTM and blood monocytes, related to Figure 1.

(A–I) Flow cytometry gating strategy used to delineate blood CD45$^+$Lin$^-$Ly6G$^-$CD11b$^+$CD115$^+$Ly6C$^+$ classical monocytes (Ly6C$^+$ cMo) or Ly6C$^-$ patrolling monocytes (Ly6C$^-$ pMo) (A), CD45$^+$Lin$^-$Ly6C$^-$CD11b$^+$CD115$^+$MHC-II$^+$F4/80$^-$ small peritoneal macs (SPM) and CD45$^+$Lin$^-$Ly6C$^-$CD11b$^+$CD115$^+$MHC-II$^-$F4/80$^+$ large peritoneal macs (LPM) (B), spleen CD45$^+$Lin$^-$Ly6C$^-$F4/80$^+$CD64$^+$CD11c$^-$CD11b$^-$ red pulp macs (RPM) (C), liver CD45$^+$Lin$^-$CD64$^+$CD11b^{int}F4/80$^+$Ly6C$^-$MHC-II^{lo}Tim4$^+$ Kupffer cells (KC) and CD45$^+$Lin$^-$CD64$^+$CD11b^{int}F4/80$^+$Ly6C$^-$MHC-II^{hi}Tim4$^-$ liver capsular macs (LCM) (D), CD45$^+$Lin$^-$Ly6C$^-$CD11b$^+$F4/80$^+$CD64$^+$MHC-II$^+$CD11c^{int} kidney resident macs (KRM) (E), CD45$^+$Lin$^-$F4/80$^+$CD64$^+$Ly6C$^-$MHC-II$^+$CD163$^-$ colonic lamina propria macs (C LMP) or CD163$^+$ muscularis macs (MM) (F), brain CD45$^+$Lin$^-$Ly6C$^-$F4/80$^+$CD64$^+$CD206$^-$MHC-II$^-$ microglia (MG), CD45$^+$Lin$^-$Ly6C$^-$F4/80$^+$CD64$^+$MHC-II$^-$CD38$^+$ border associated macs (CD38$^+$ BAM) and CD45$^+$Lin$^-$Ly6C$^-$F4/80$^+$CD64$^+$MHC-II$^+$CD38$^-$ border associated macs (MHC-II$^+$ BAM) (G), skin CD45$^+$Lin$^-$Ly6C$^-$F4/80$^+$CD64$^-$CD24$^+$MHC-II$^+$CD11c$^+$ Langerhans cells (LC), CD45$^+$Lin$^-$Ly6C$^-$F4/80$^+$CD64$^+$MHC-II$^+$ dermal macs (MHC-II$^+$ DM) or MHC-II$^-$ DM (H), lung CD45$^+$Lin$^-$Ly6C$^-$F4/80$^+$CD64$^+$SiglecF$^+$CD11b$^-$ alveolar macs (AM), CD45$^+$Lin$^-$Ly6C$^-$F4/80$^+$CD64$^+$SiglecF$^-$CD11b$^+$CD206$^+$ interstitial macs (CD206$^+$ IM) or CD206$^-$ IM (I).
(J) Representative histograms of intracellular MafB expression in the indicated blood monocyte (Mo) and resident tissue mac (RTM) populations from wild-type (WT) mice, as in A–I (n = 4).

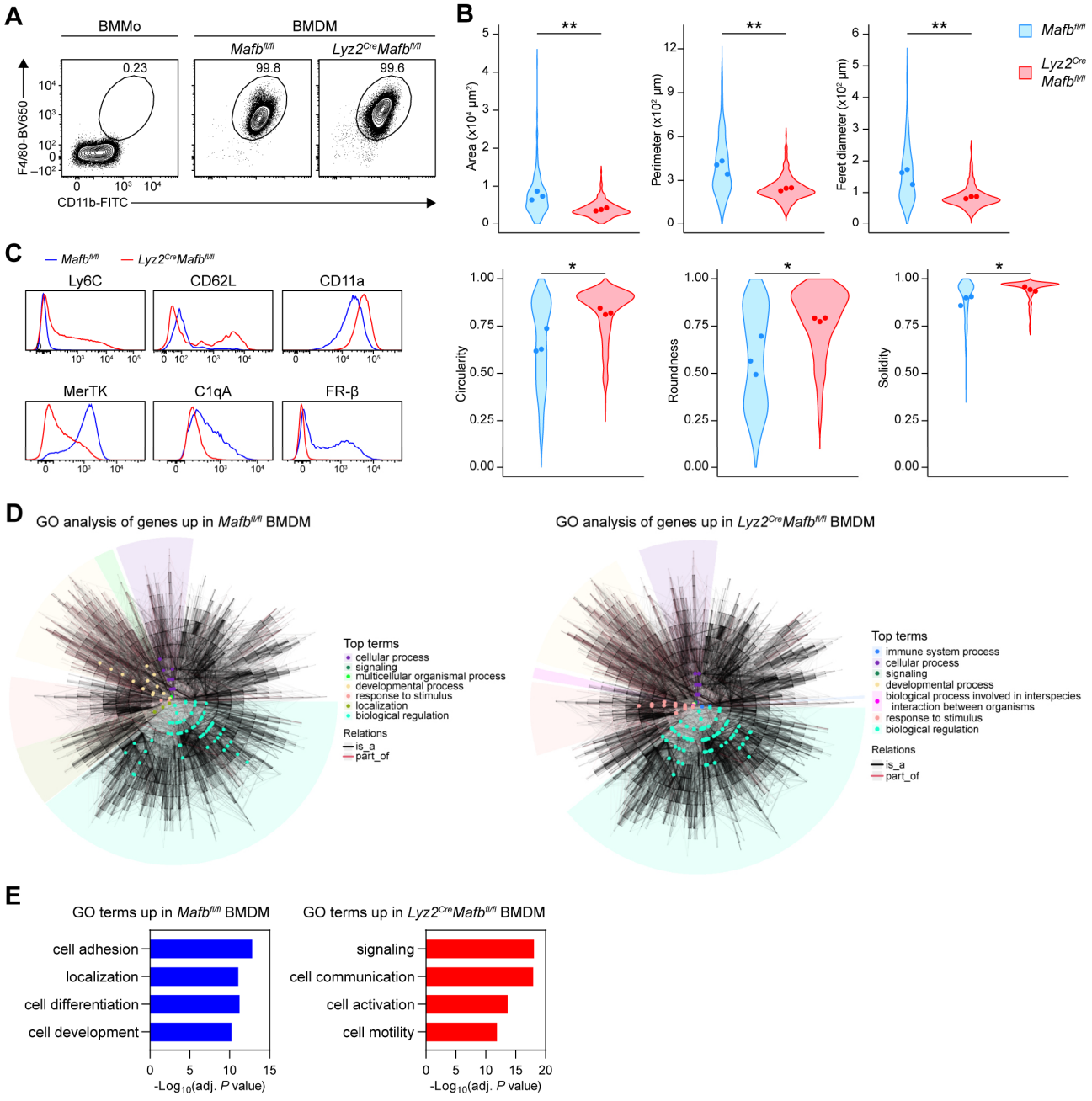

Figure S2. Differential morphology and Gene Ontology enrichment in BMDMs from myeloid-restricted MafB-deficient mice, related to Figure 2.

(A) Representative contour plots of F4/80 and CD11b expression in bone marrow monocytes (BMMo) from WT mice and bone marrow-derived macrophages (BMDM) from *Mafb*$^{fl/fl}$ and *Lyz2*^{Cre}*Mafb*$^{fl/fl}$ mice (n = 6).
(B) Violin plots of BMDM morphology quantified by differential interference contrast microscopy (n = 3). Height indicates morphological parameter; width indicates abundance of cells. One hundred cells were analyzed per biological replicate; dots represent mean values from each replicate.
(C) Representative histograms of Mo (top) and Mac (bottom) marker protein expression in BMDM from *Mafb*$^{fl/fl}$ and *Lyz2*^{Cre}*Mafb*$^{fl/fl}$ mice (n = 6–7).
(D) Circular directed acyclic graphs (DAG) of biological process (BP) gene ontology (GO) terms connected by hierarchical relations. Significant BP GO terms from a GO enrichment analysis of

differentially expressed genes (DEGs) upregulated in BMDMs from *Mafb*$^{fl/fl}$ (left) and *Lyz2*^{Cre}*Mafb*$^{fl/fl}$ (right) mice mice are highlighted as colored nodes.
(E) Bar graphs of the top enriched GO terms on DEGs upregulated in BMDMs from *Mafb*$^{fl/fl}$ (left) and *Lyz2*^{Cre}*Mafb*$^{fl/fl}$ (right) mice, as in D.

P values were calculated using a two-tailed Student's *t* test (B). **P* < 0.05; ***P* < 0.01.

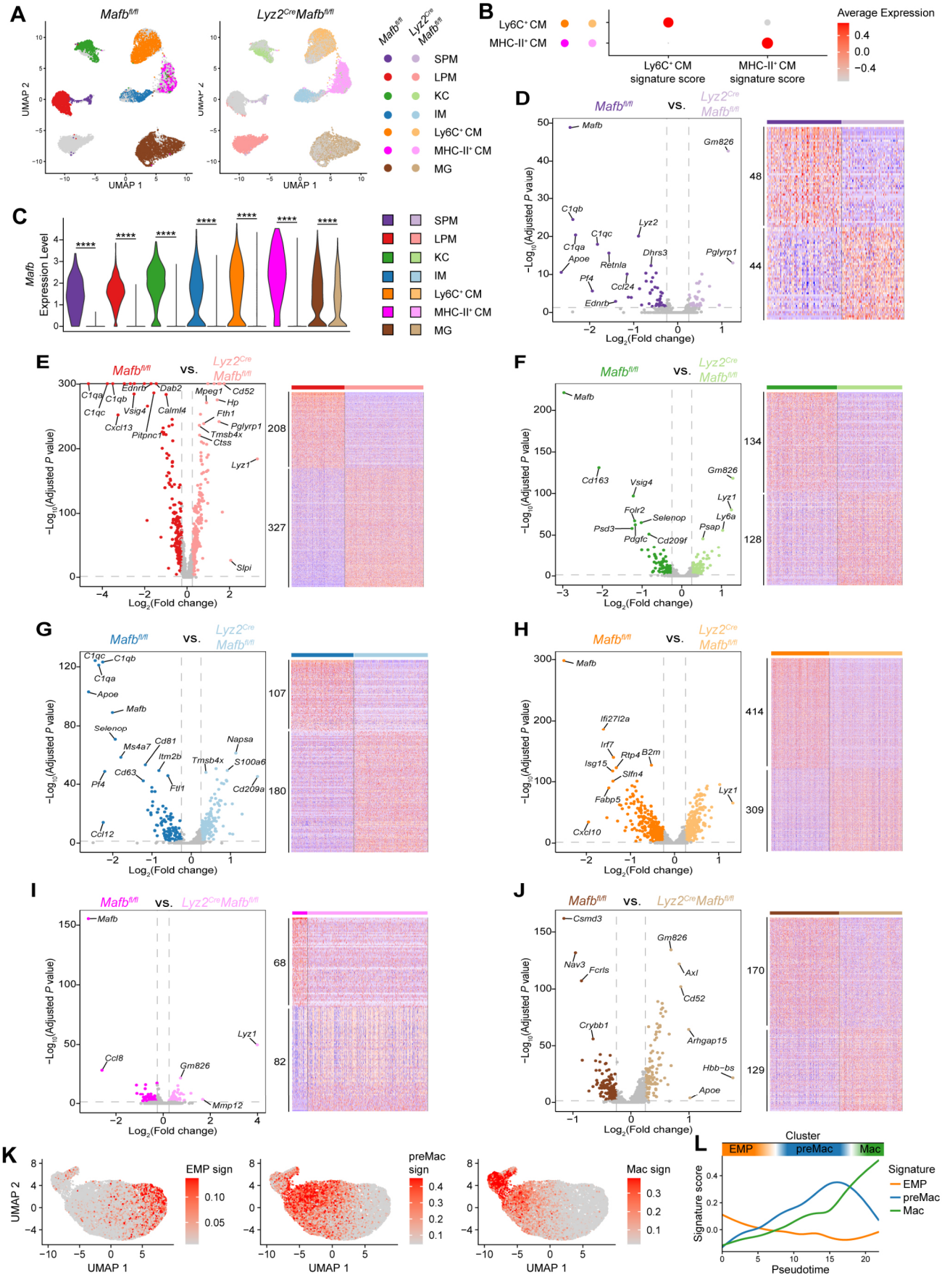
A
Mafb fl/fl
Lyz2Cre Mafb fl/fl
UMAP 1
UMAP 2
SPM
LPM
KC
IM
Ly6C+ CM
MHC-II+ CM
MG
B
Ly6C+ CM
MHC-II+ CM
Ly6C+ CM signature score
MHC-II+ CM signature score
Average Expression
C
Mafb Expression Level
****
D
Mafb fl/fl vs. Lyz2Cre Mafb fl/fl
−Log10(Adjusted P value)
Log2(Fold change)
Mafb
Gm826
C1qb
C1qc
C1qa
Apoe
Lyz2
Dhrs3
Retnla
Pf4
Ccl24
Ednrb
Pglyrp1
48
44
E
Mafb fl/fl vs. Lyz2Cre Mafb fl/fl
C1qa
C1qb
C1qc
Ednrb
Dab2
Vsig4
Calml4
Cxcl13
Pitpnc1
Mpeg1
Cd52
Hp
Fth1
Pglyrp1
Tmsb4x
Ctss
Lyz1
Slpi
208
327
F
Mafb fl/fl vs. Lyz2Cre Mafb fl/fl
Mafb
Cd163
Vsig4
Folr2
Selenop
Psd3
Pdgfc
Cd209f
Gm826
Lyz1
Ly6a
Psap
134
128
G
Mafb fl/fl vs. Lyz2Cre Mafb fl/fl
C1qc
C1qb
C1qa
Apoe
Mafb
Selenop
Ms4a7
Cd81
Itm2b
Cd63
Pf4
Ftl1
Tmsb4x
Napsa
S100a6
Cd209a
Ccl12
107
180
H
Mafb fl/fl vs. Lyz2Cre Mafb fl/fl
Mafb
Ifi27l2a
Irf7
Rtp4
B2m
Isg15
Slfn4
Fabp5
Cxcl10
Lyz1
414
309
I
Mafb fl/fl vs. Lyz2Cre Mafb fl/fl
Mafb
Lyz1
Ccl8
Gm826
Mmp12
68
82
J
Mafb fl/fl vs. Lyz2Cre Mafb fl/fl
Csmd3
Gm826
Nav3
Fcrls
Axl
Cd52
Crybb1
Arhgap15
Hbb−bs
Apoe
170
129
K
UMAP 2
UMAP 1
EMP sign
preMac sign
Mac sign
L
Cluster
EMP
preMac
Mac
Signature
EMP
preMac
Mac
Signature score
Pseudotime

Figure S3. Transcriptional identity differential gene expression across RTM subsets in myeloid-restricted MafB-deficient mice, related to Figure 3.

(A) UMAP of RTM populations from *Mafb*$^{fl/fl}$ (left) and *Lyz2*^{Cre}*Mafb*$^{fl/fl}$ (right) mice.
(B) Dot plots of Ly6C^{+} colonic mac (CM) and MHC-II^{+} CM signature scores within each CM subset from *Mafb*$^{fl/fl}$ and *Lyz2*^{Cre}*Mafb*$^{fl/fl}$ mice.
(C) Violin plots of *Mafb* expression within RTM populations from *Mafb*$^{fl/fl}$ and *Lyz2*^{Cre}*Mafb*$^{fl/fl}$ mice, as in A (height: expression; width: abundance of cells).
(D–J) Volcano plots and heatmaps of DEGs between *Mafb*$^{fl/fl}$ and *Lyz2*^{Cre}*Mafb*$^{fl/fl}$ RTMs, shown for SPM (D), LPM (E), KC (F), IM (G), Ly6C^{+} CM (H), MHC-II^{+} CM (I), and MG (J). Transcripts significantly upregulated in RTM from *Mafb*$^{fl/fl}$ and *Lyz2*^{Cre}*Mafb*$^{fl/fl}$ mice are shown in bold and light colors, respectively ($\log_2$ fold change > 0.25 or < −0.25; adjusted $P < 0.05$).
(K) Feature plots of EMP (left), preMac (middle) and Mac (right) signature scores, as in Figure 3I.
(L) EMP, preMac and Mac signature scores along pseudotime, as in Figure 3I.

P values were calculated using a Wilcoxon rank-sum test (C and D–J).

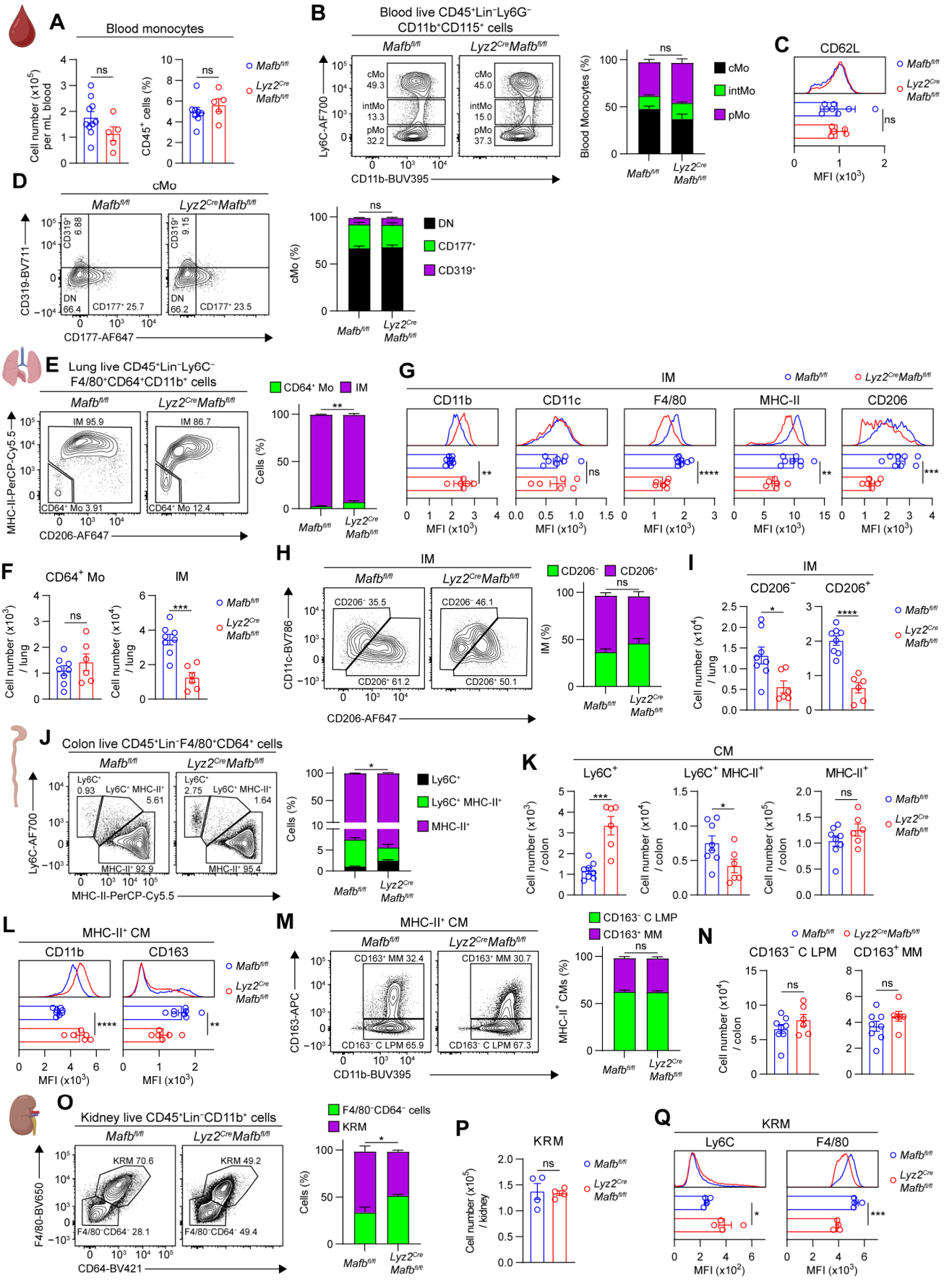
A
Blood monocytes
Cell number (x10^5) per mL blood
CD45+ cells (%)
ns
Mafb fl/fl
Lyz2Cre Mafb fl/fl
B
Blood live CD45+Lin-Ly6G- CD11b+CD115+ cells
Ly6C-AF700
CD11b-BUV395
cMo 49.3
intMo 13.3
pMo 32.2
cMo 45.0
intMo 15.0
pMo 37.3
Blood Monocytes (%)
cMo
intMo
pMo
C
CD62L
MFI (x10^3)
D
cMo
CD319-BV711
CD177-AF647
CD319+ 6.88
DN 66.4
CD177+ 25.7
CD319+ 9.15
DN 66.2
CD177+ 23.5
cMo (%)
DN
CD177+
CD319+
E
Lung live CD45+Lin-Ly6C- F4/80+CD64+CD11b+ cells
MHC-II-PerCP-Cy5.5
CD206-AF647
IM 95.9
CD64+ Mo 3.91
IM 86.7
CD64+ Mo 12.4
CD64+ Mo
IM
Cells (%)
F
CD64+ Mo
IM
Cell number (x10^3) / lung
Cell number (x10^4) / lung
G
IM
CD11b
CD11c
F4/80
MHC-II
CD206
MFI (x10^3)
H
IM
CD11c-BV786
CD206- 35.5
CD206+ 61.2
CD206- 46.1
CD206+ 50.1
CD206-
CD206+
IM (%)
I
IM
CD206-
CD206+
Cell number (x10^4) / lung
J
Colon live CD45+Lin-F4/80+CD64+ cells
Ly6C-AF700
MHC-II-PerCP-Cy5.5
Ly6C+ 0.93
Ly6C+ MHC-II+ 5.61
MHC-II+ 92.9
Ly6C+ 2.75
Ly6C+ MHC-II+ 1.64
MHC-II+ 95.4
Ly6C+
Ly6C+ MHC-II+
MHC-II+
Cells (%)
K
CM
Ly6C+
Ly6C+ MHC-II+
MHC-II+
Cell number (x10^3) / colon
Cell number (x10^4) / colon
Cell number (x10^5) / colon
L
MHC-II+ CM
CD11b
CD163
MFI (x10^3)
M
MHC-II+ CM
CD163-APC
CD11b-BUV395
CD163+ MM 32.4
CD163- C LPM 65.9
CD163+ MM 30.7
CD163- C LPM 67.3
CD163- C LMP
CD163+ MM
MHC-II+ CMs (%)
N
CD163- C LPM
CD163+ MM
Cell number (x10^4) / colon
O
Kidney live CD45+Lin-CD11b+ cells
F4/80-BV650
CD64-BV421
KRM 70.6
F4/80-CD64- 28.1
KRM 49.2
F4/80-CD64- 49.4
F4/80-CD64- cells
KRM
Cells (%)
P
KRM
Cell number (x10^5) / kidney
Q
KRM
Ly6C
F4/80
MFI (x10^2)
MFI (x10^3)

Figure S4. Impact of MafB deficiency on blood monocytes and lung, colon and kidney RTM subsets, related to Figure 4.

(A) Bar graphs of blood Mo shown as absolute number per mL of blood (left) and percentage of live CD45$^+$ cells (right) from *Mafb$^{fl/fl}$* and *Lyz2^{Cre}Mafb$^{fl/fl}$* mice (n = 5–10). All subsequent panels compare *Mafb$^{fl/fl}$* and *Lyz2^{Cre}Mafb$^{fl/fl}$* mice.
(B) Representative contour plots of Ly6C and CD11b expression within blood live CD45$^+$Lin$^-$Ly6G$^-$CD115$^+$CD11b$^+$ cells (left) and bar graphs of the percentage of cMo, intermediate Mo (intMo), and pMo, as gated on the contour plots (right) (n = 5–8).
(C) Histograms (top) and bar graphs (bottom) of CD62L expression in cMo, as in B.
(D) Representative contour plots of CD319 and CD177 expression within cMo (left) and bar graphs of the percentage of double negative (DN), CD177$^+$, and CD319$^+$ cMo, as gated on the contour plots (right) (n = 5–8).
(E) Representative contour plots of MHC-II and CD206 expression within lung live CD45$^+$Lin$^-$Ly6C$^-$F4/80$^+$CD64$^+$CD11b$^+$ cells (left) and bar graphs of the percentage of CD64$^+$ Mo and IM, as gated on the contour plots (right) (n = 6–8).
(F) Bar graphs of absolute numbers of CD64$^+$ Mo and IM, as in E.
(G) Histograms (top) and bar graphs (bottom) of CD11b, CD11c, F4/80, MHC-II, and CD206 expression in IM, as in E.
(H) Representative contour plots of CD11c and CD206 expression within IM (left) and bar graphs of the percentage of CD206$^-$ and CD206$^+$ IM, as gated on the contour plots (right) (n = 6–8).
(I) Bar graphs of absolute numbers of CD206$^-$ and CD206$^+$ IM, as in H.
(J) Representative contour plots of Ly6C and MHC-II expression within colon live CD45$^+$Lin$^-$F4/80$^+$CD64$^+$ cells (left) and bar graphs of the percentage of Ly6C$^+$, Ly6C$^+$MHC-II$^+$, and MHC-II$^+$ CM, as gated on the contour plots (right) (n = 6–8).
(K) Bar graphs of absolute numbers of Ly6C$^+$, Ly6C$^+$MHC-II$^+$, and MHC-II$^+$ CM, as in J.
(L) Histograms (top) and bar graphs (bottom) of CD11b and CD163 expression in MHC-II$^+$ CM, as in J.
(M) Representative contour plots of CD163 and CD11b expression within MHC-II$^+$ CM (left) and bar graphs of the percentage of CD163$^-$ C LPM and CD163$^+$ MM, as gated on the contour plots (right) (n = 6–8).
(N) Bar graphs of absolute numbers of CD163$^-$ C LPM and CD163$^+$ MM, as in M.
(O) Representative contour plots of F4/80 and CD64 expression within kidney live CD45$^+$Lin$^-$CD11b$^+$ cells (left) and bar graphs of the percentage of F4/80$^-$CD64$^-$ cells and KRM, as gated on the contour plots (right) (n = 4).
(P) Bar graphs of absolute numbers of KRM, as in O.
(Q) Histograms (top) and bar graphs (bottom) of F4/80 and Ly6C expression in KRM, as in O.

Data are mean ± SEM and are pooled from two independent experiments. *P* values were calculated using a two-tailed Student's *t* test. *, $P < 0.05$; **, $P < 0.01$; ***, $P < 0.001$; ****, $P < 0.0001$. MFI, mean fluorescence intensity; ns, not significant.

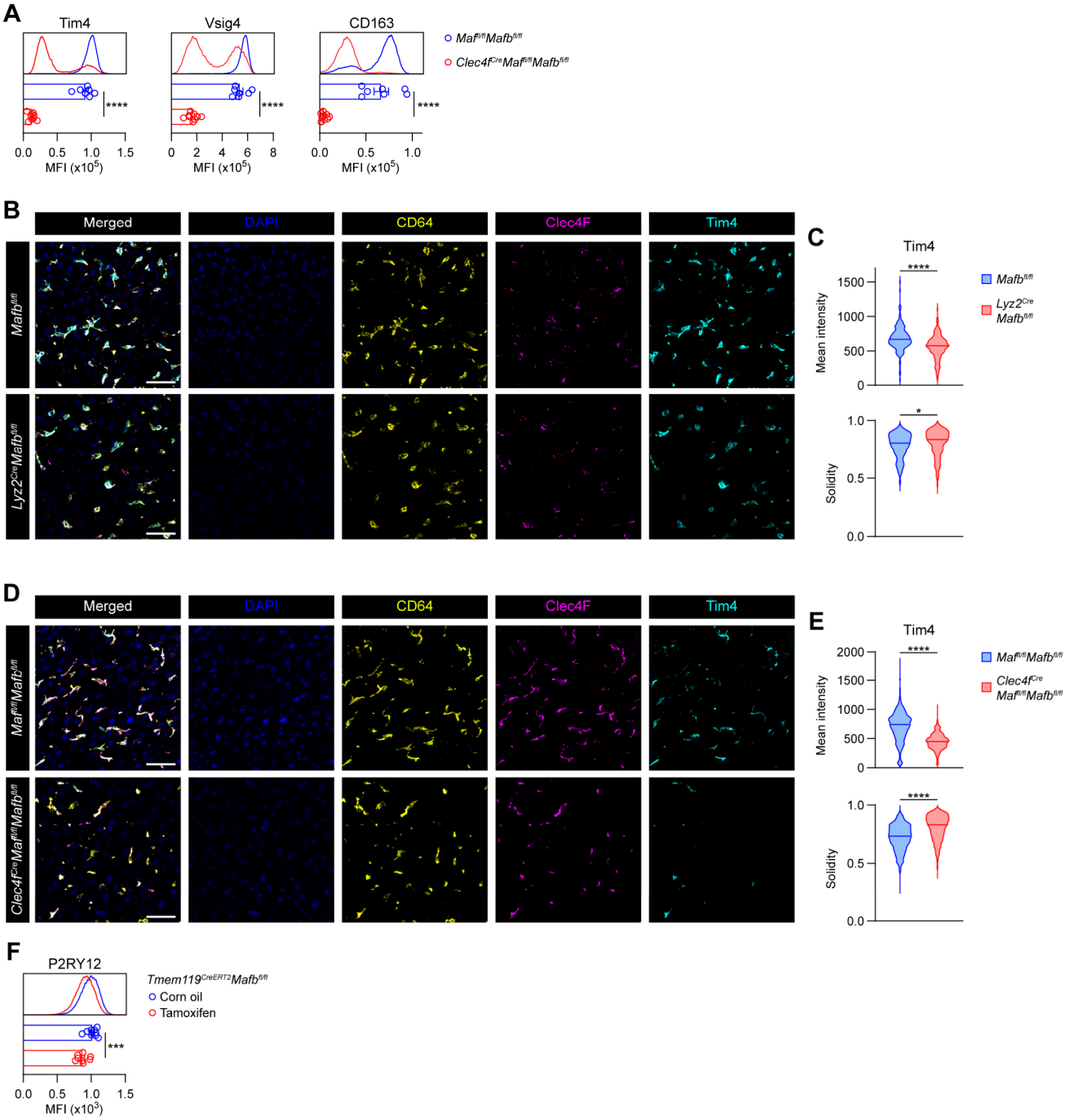

Figure S5. Impact of RTM-specific MafB deficiency on Kupffer cell and microglia phenotypes, related to Figure 4.

(A) Histograms (top) and bar graphs (bottom) of Tim4, Vsig4, and CD163 expression in KCs from *Maf*$^{fl/fl}$*Mafb*$^{fl/fl}$ and *Clec4f*^{Cre}*Maf*$^{fl/fl}$*Mafb*$^{fl/fl}$ mice (n = 7–9).
(B) Representative confocal images of KCs from *Mafb*$^{fl/fl}$ and *Lyz2*^{Cre}*Mafb*$^{fl/fl}$ mice (n = 3). Scale bar, 50 µm.
(C) Violin plots of Tim4 expression (top) and solidity (bottom) in CD64^{+} KCs from *Mafb*$^{fl/fl}$ and *Lyz2*^{Cre}*Mafb*$^{fl/fl}$ mice, as in B.
(D) Representative confocal images of KCs from *Maf*$^{fl/fl}$*Mafb*$^{fl/fl}$ and *Clec4f*^{Cre}*Maf*$^{fl/fl}$*Mafb*$^{fl/fl}$ mice (n = 3). Scale bar, 50 µm.

(E) Violin plots of Tim4 expression (top) and solidity (bottom) in CD64^{+} KCs from *Maf*$^{fl/fl}$*Mafb*$^{fl/fl}$ and *Clec4f*^{Cre}*Maf*$^{fl/fl}$*Mafb*$^{fl/fl}$ mice, as in D.
(F) Histograms (top) and bar graphs (bottom) of P2RY12 expression in MG from *Tmem119*^{CreERT2}*Mafb*$^{fl/fl}$ mice orally gavaged with 5 mg tamoxifen or corn oil (control) for 5 days and analyzed 2 months after the last dose (n = 9–10).

Data are mean ± SEM and are pooled from two independent experiments (A and F). *P* values were calculated using a two-tailed Student's t test (A, C[Tim4 expression] and E[Tim4 expression], F) or a two-tailed Mann–Whitney test (C[Solidity] and E[Solidity]). *, $P < 0.05$; ***, $P < 0.001$; ****, $P < 0.0001$.

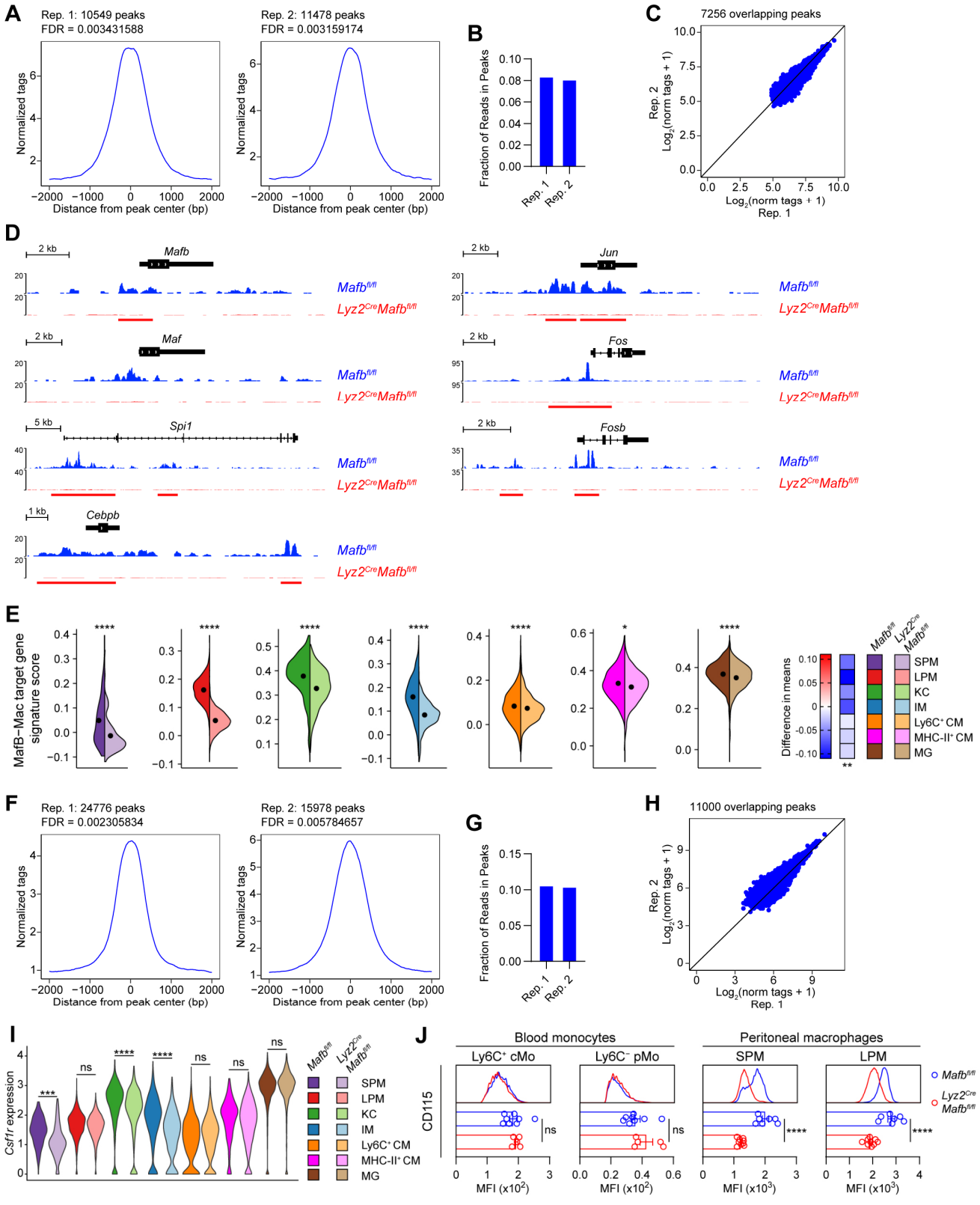

Figure S6. MafB binds to *cis*-regulatory elements to promote transcription of key mac differentiation and identity genes, related to Figure 6.

(A–C) Quality control of MafB CUT&RUN peak calling in BMDMs. (A) Histograms of normalized tag counts at MafB peaks for two replicates, with corresponding numbers of called peaks and false discovery rates (FDRs) indicated. (B) Bar graphs of the fraction of reads in peaks (FRiP) for each replicate. (C) Scatterplot of normalized tag counts at overlapping MafB peaks in both replicates.
(D) CUT&RUN tracks depicting MafB binding around representative transcriptional regulators of mac differentiation in BMDMs from *Mafb*$^{fl/fl}$ and *Lyz2*^{Cre}*Mafb*$^{fl/fl}$ mice, visualized with the Integrative Genomics Viewer (IGV). Horizontal red bars, MafB binding sites in BMDMs.
(E) Violin plots of mac-specific MafB target gene signature scores in RTMs from *Mafb*$^{fl/fl}$ and *Lyz2*^{Cre}*Mafb*$^{fl/fl}$ mice, as in Figure 3 (height, score; width, abundance).
(F–H) Quality control of MafB CUT&RUN peak calling in LPMs. (F) Histograms of normalized tag counts at MafB peaks for two replicates, with corresponding numbers of called peaks and FDRs indicated. (G) Bar graphs of FRiP for each replicate. (H) Scatterplot of normalized tag counts at overlapping MafB peaks in both replicates.
(I) Violin plots of *Csf1r* expression within RTM populations from *Mafb*$^{fl/fl}$ and *Lyz2*^{Cre}*Mafb*$^{fl/fl}$ mice, as in Figure 3 (height, expression; width, abundance of cells).
(J) Histograms (top) and bar graphs (bottom) of CD115 expression in blood Mo (left) and peritoneal macs (right) from *Mafb*$^{fl/fl}$ and *Lyz2*^{Cre}*Mafb*$^{fl/fl}$ mice (n = 5–9).

Data are mean ± SEM and are pooled from two independent experiments (J). *P* values were calculated using a Wilcoxon rank-sum test (E and I) or a two-tailed Student's t test (J). $^{*}P < 0.05$; $^{***}P < 0.001$; $^{****}P < 0.0001$.

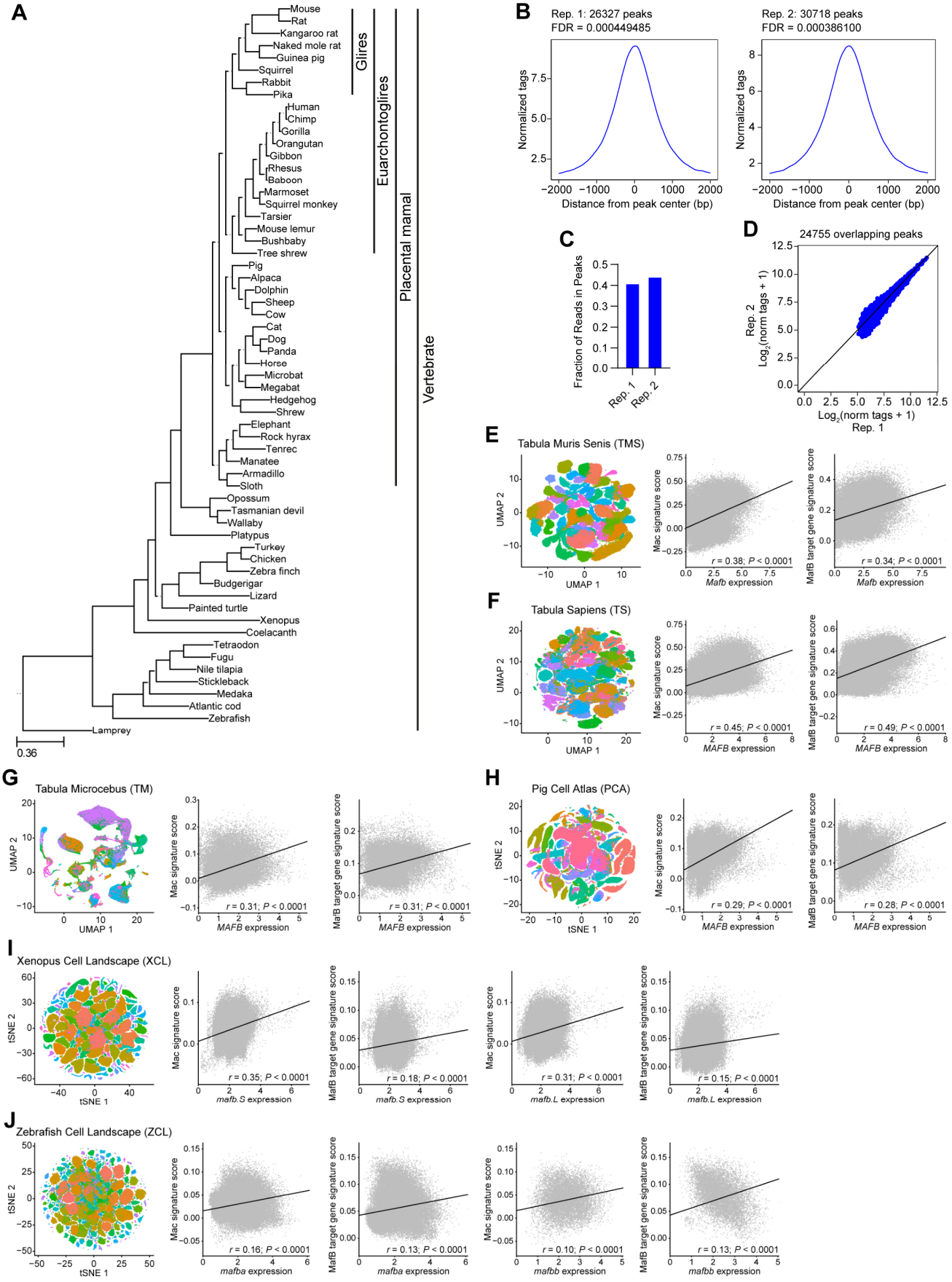
A
Mouse
Rat
Kangaroo rat
Naked mole rat
Guinea pig
Squirrel
Rabbit
Pika
Human
Chimp
Gorilla
Orangutan
Gibbon
Rhesus
Baboon
Marmoset
Squirrel monkey
Tarsier
Mouse lemur
Bushbaby
Tree shrew
Pig
Alpaca
Dolphin
Sheep
Cow
Cat
Dog
Panda
Horse
Microbat
Megabat
Hedgehog
Shrew
Elephant
Rock hyrax
Tenrec
Manatee
Armadillo
Sloth
Opossum
Tasmanian devil
Wallaby
Platypus
Turkey
Chicken
Zebra finch
Budgerigar
Lizard
Painted turtle
Xenopus
Coelacanth
Tetraodon
Fugu
Nile tilapia
Stickleback
Medaka
Atlantic cod
Zebrafish
Lamprey
0.36
Glires
Euarchontoglires
Placental mamal
Vertebrate
B
Rep. 1: 26327 peaks
FDR = 0.000449485
Rep. 2: 30718 peaks
FDR = 0.000386100
Normalized tags
Distance from peak center (bp)
C
Fraction of Reads in Peaks
Rep. 1
Rep. 2
D
24755 overlapping peaks
Rep. 2
Log2(norm tags + 1)
Rep. 1
E
Tabula Muris Senis (TMS)
UMAP 1
UMAP 2
Mac signature score
MafB target gene signature score
Mafb expression
r = 0.38; P < 0.0001
r = 0.34; P < 0.0001
F
Tabula Sapiens (TS)
r = 0.45; P < 0.0001
r = 0.49; P < 0.0001
MAFB expression
G
Tabula Microcebus (TM)
r = 0.31; P < 0.0001
r = 0.31; P < 0.0001
H
Pig Cell Atlas (PCA)
tSNE 1
tSNE 2
r = 0.29; P < 0.0001
r = 0.28; P < 0.0001
I
Xenopus Cell Landscape (XCL)
mafb.S expression
mafb.L expression
r = 0.35; P < 0.0001
r = 0.18; P < 0.0001
r = 0.31; P < 0.0001
r = 0.15; P < 0.0001
J
Zebrafish Cell Landscape (ZCL)
mafba expression
mafbb expression
r = 0.16; P < 0.0001
r = 0.13; P < 0.0001
r = 0.10; P < 0.0001
r = 0.13; P < 0.0001

Figure S7. MafB binding site conservation across species, related to figure 7.

(A) Phylogenetic tree derived from the multiple sequence alignment of 60 vertebrate genomes with mouse as the reference genome.
(B–D) Quality control of MafB CUT&RUN peak calling in human monocyte-derived macrophages (MDMs). (B) Histograms of normalized tag counts at MafB peaks for two replicates, with corresponding numbers of called peaks and FDRs indicated. (C) Bar graphs of FRiP for each replicate. (D) Scatterplot of normalized tag counts at overlapping MafB peaks in both replicates.
(E–J) Correlations between *Mafb* expression and either mac or conserved MafB target gene signature scores across species, as in Figure 7J, using the Tabula Muris Senis (E), Tabula Sapiens (F), Tabula Microcebus (G), Pig Cell Atlas (H), Xenopus Cell Landscape (I), and Zebrafish Cell Landscape (J) datasets.

P values were calculated using a Pearson correlation test.